

Investigation on the Anisotropic Mechanical Behaviour of the Callovo- Oxfordian Clay Rock

Final Report

within the framework of
ANDRA/GRS cooperation
programme



GRS

**Investigation on the
Anisotropic Mechanical
Behaviour of the Callovo-
Oxfordian Clay Rock**

within the framework of
ANDRA/GRS cooperation
programme

Final Report

Chun-Liang Zhang (GRS)
Gilles Armand (ANDRA)
Nathalie Conil (ANDRA)

January 2015

Acknowledgement:

This report was prepared under
contract No. 059844 with the
French Agence Nationale Pour la
Gestion de Déchets Radioactifs
(ANDRA).

The work was conducted by the
Gesellschaft für Anlagen- und
Reaktorsicherheit (GRS) gGmbH.

The author is responsible for the
content of this report.

Keywords

Callovo-Oxfordian Clay Rock, Experiment, Compression, Extension, Failure Strength, Mechanical Anisotropy, Stress-Strain Behaviour

Table of contents

1	Introduction.....	1
2	Characterization of samples	3
2.1	Coring and sample preparation.....	3
2.2	Mineral composition.....	6
2.3	Physical properties	8
3	Laboratory experiments	13
3.1	Test programme	13
3.2	Test methods.....	14
3.3	Test results	17
3.3.1	Hydrostatic pre-compaction	18
3.3.2	Triaxial compression at constant strain rate	24
3.3.3	Triaxial compression at constant stress rate	28
3.3.4	Triaxial extension by lateral compression at constant axial stress.....	30
3.3.5	Triaxial extension by lateral compression and axial tension	30
3.3.6	Triaxial creep under multistep stresses.....	32
3.4	Analysis of the test results	35
3.4.1	Elastic properties	35
3.4.2	Failure strength and mode	46
4	Conclusions.....	53
	List of tables	57
	List of figures	59

Appendix

A	Appendix: Drilled cores and sample preparation.....	65
B	Appendix: Mineral composition of drilled cores	67
C	Appendix: Characteristics of tested samples.....	69

D	Appendix: Test plan	73
E	Appendix: Test data	75
E.1	TCD – triaxial compression tests with strain control	75
E.2	TCS – triaxial compression tests with stress control	88
E.3	TES – triaxial extension tests at constant axial stress	93
E.4	TEM – triaxial extension tests at constant mean stress.....	98
E.5	TCC – triaxial creep tests at multistep stress states	103

1 Introduction

An underground repository for disposal of radioactive waste is planned to be constructed in the sedimentary Callovo-Oxfordian argillaceous formation (COX) in France /AND 05/. The clay rock exhibits inherent anisotropy with bedding structure, which leads to directional dependences of the rock properties (e.g. mineralogical, physical, mechanical, hydraulic, thermal, etc.) with respect to the bedding planes. For the design of the repository and the assessment of its safety during the operation and post-closure phases it is necessary to characterise and predict the anisotropic properties and processes in the host rock, particularly in the excavation damaged zone (EDZ) near the openings.

Within the framework of the bilateral cooperation agreement between the French National Radioactive Waste Management Agency (ANDRA) and the German Federal Ministry of Economics and Technology (BMWi), concerning the research activities in the Meuse/Haute-Marne Underground Research Laboratory (MHM-URL), a joint research programme was initiated by ANDRA and GRS in 2013 to investigate mechanical anisotropy of the COX clay rock for the purpose of precise characterization, better understanding and reliable prediction of the development of EDZ around the repository. This programme was funded by ANDRA under contract number 059844 and performed by GRS during the time period of November 2013 to December 2014. GRS gratefully acknowledges the financial support from and the fruitful cooperation with ANDRA.

The research work focused on laboratory investigations on COX core samples extracted from boreholes drilled in different orientations at the -490m main level of the MHM-URL. Various kinds of experiments were performed under different stress conditions, including triaxial compression and extension, and time effects. The stress-strain behaviour, the elastic properties, the damage and failure strength were determined and analysed with regard to the structural anisotropy of the clay rock. The anisotropic behaviour of the COX clay rock is briefly compared with other clay rocks such as the Opalinus clay at Mont Terri and the Tournemire shale based on the data from literature. Some important results from previous studies by GRS are also involved in the analysis concerning effects of confining stress and load duration. The experiments and results are presented in this report.

2 Characterization of samples

2.1 Coring and sample preparation

Six coring boreholes were drilled in different directions from a horizontal gallery NER at the -490m main level of the MHM-URL. The position of the gallery is marked within a red circle in Fig. 2.1. The boreholes intercepted the quasi-horizontal bedding planes at approximately five angles of $\alpha \approx 0^\circ$, 30° , 45° , 60° and 90° (see Fig. 2.2):

1. OHZ6565 and OHZ6564 parallel to the horizontal bedding with an angle of $\alpha \approx 0^\circ$;
 2. OHZ6563 inclined to the horizontal bedding with an angle of $\alpha \approx 30^\circ$;
 3. OHZ6562 inclined to the horizontal bedding with an angle of $\alpha \approx 45^\circ$;
 4. OHZ6561 inclined to the horizontal bedding with an angle of $\alpha \approx 60^\circ$;
 5. OHZ6560 perpendicular to the horizontal bedding with an angle of $\alpha \approx 90^\circ$.

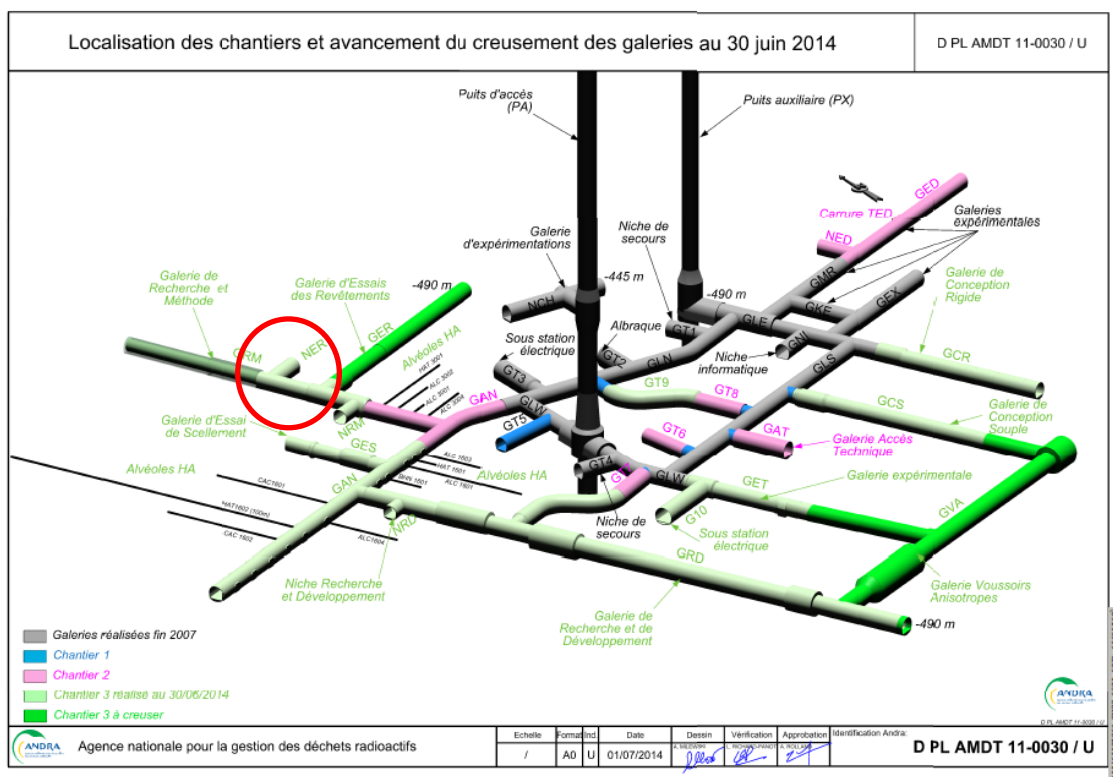


Fig. 2.1 Position of the coring drift NER at the -490m main level of the MHM-URL

Forages géologiques OHZ6560 à OHZ6565 en NER
et les échantillons pour la GRS mbH

D PL ACSE14-0026 / B

Forages	Longueur (en m)	Inclinaison (en °)
OHZ6560	11,15m	89,60°
OHZ6561	8,74m	60,34°
OHZ6562	9,92m	44,54°
OHZ6563	8,40m	29,61°
OHZ6564	12,74m	0,10°
OHZ6565	5,95m	-0,36°

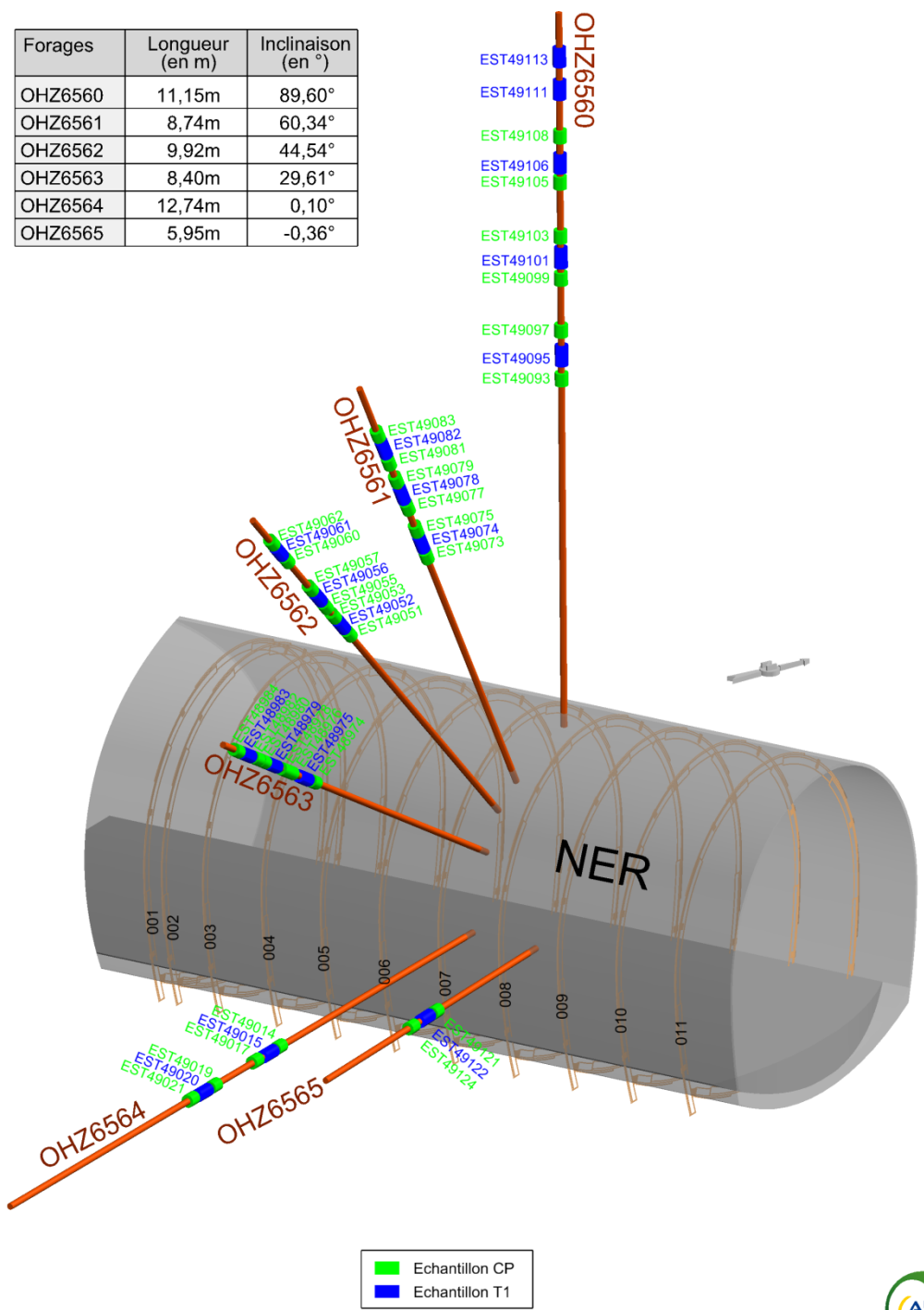


Fig. 2.2 Arrangement of the boreholes and sampling positions

The boreholes were pneumatically drilled to depths of 6 to 13 meters. Five of them lay in a vertical plane across the gallery, except for the horizontal borehole OHZ6565. Totally, 47 cores of 78.5 mm diameter and 200 – 300 mm lengths were extracted from the boreholes in the depths of 5 to 10 meters beyond the damaged zone near the drift wall. The positions of the cores are marked in Fig. 2.2. At least 9 cores were taken for each direction. The cores were immediately confined in T-cells or in aluminium foils after coring in order to prevent desaturation and damage. Some photos of the drilled cores are presented in Appendix A for an unpacked core from the T-cell and another one from the foil. A few cores were damaged after unpacking and they were not used for testing.

The confined cores were delivered by ANDRA to the GRS laboratory and stored in a climate-controlled room at 22 °C until testing. From the cores, cylindrical samples were carefully prepared by cutting and smoothing the surfaces in a lathe (a photo in App. A). Two sample sizes were defined as diameter/length = 50mm/100mm and 70mm/140mm for different tests. For each direction a typical sample is shown in Fig. 2.3. The bedding structure can be visually recognized on the sample surface. The natural intrinsic bedding structure leads to directional dependences of the rock properties. Because of high sensitivities of the clay rock to unloading and environment changes, microcracks were unavoidably induced during coring and sampling. The propagation and interconnection of the microcracks yielded a few visible fractures in some samples along the bedding planes (photos in App. A).

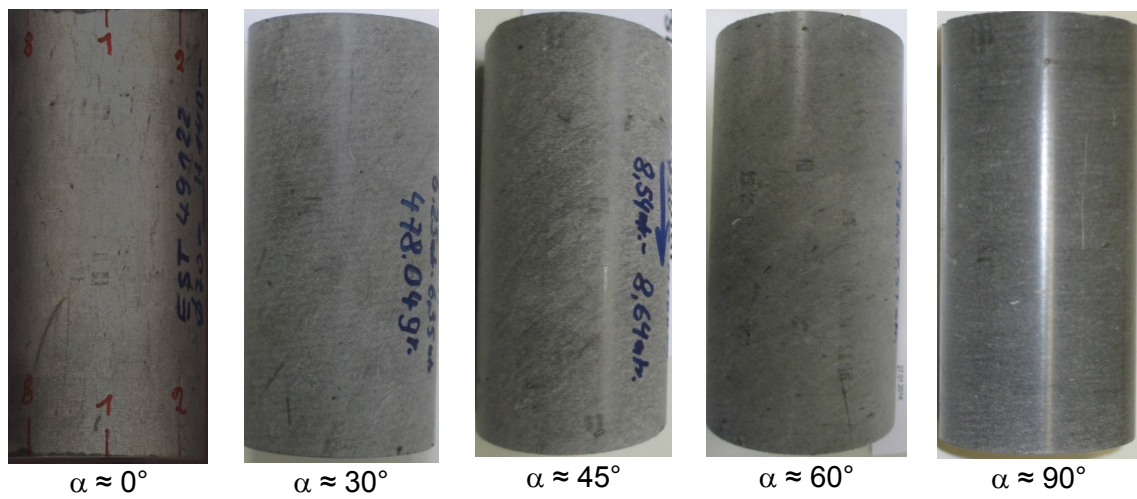


Fig. 2.3 Pictures of typical samples with bedding planes inclined to the sample axis at angles of $\alpha \approx 0^\circ$, 30° , 45° , 60° and 90°

2.2 Mineral composition

Main mineralogical components of the samples, including clay, carbonate and quartz, were estimated by ANDRA. The results are summarised in Appendix B and in Fig. 2.4. The mineralogical components vary from one position to another, indicating the inherent heterogeneous nature of the rock. On average, the investigated rock region contains 35 % clay minerals, 33 % carbonates, 31 % quartz and small amounts of others. Additionally, there are also some organic components in the rock as observed in some cores (photos in App. A). The organic components affect negatively the rock mass strength.

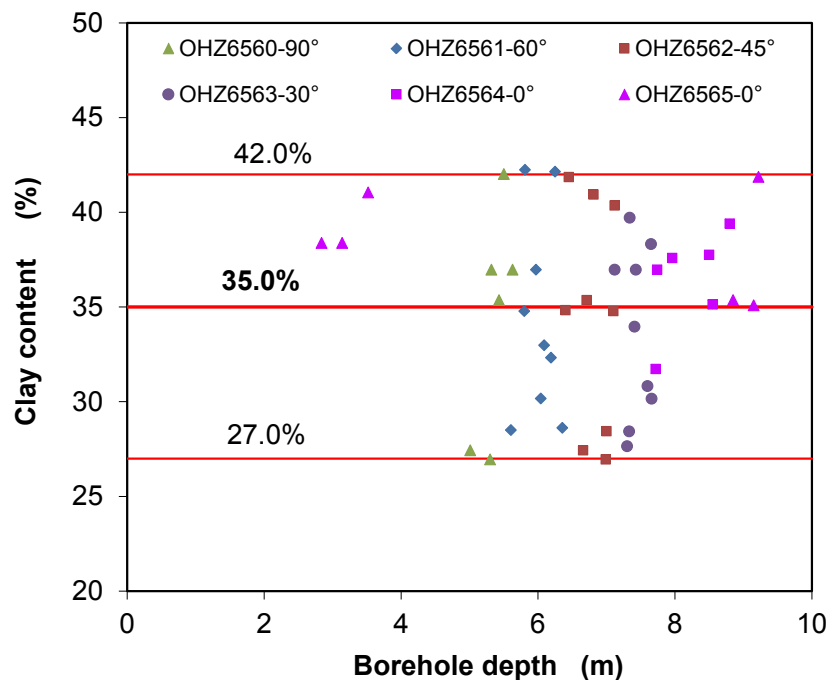


Fig. 2.4 Distributions of the main mineralogical components (clay, carbonate, quartz etc.) in the sampling region

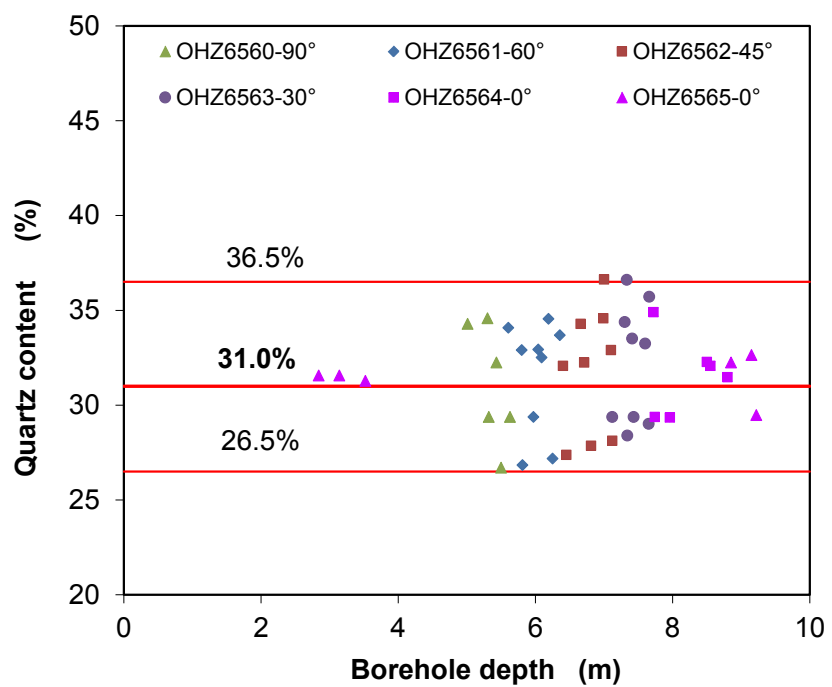
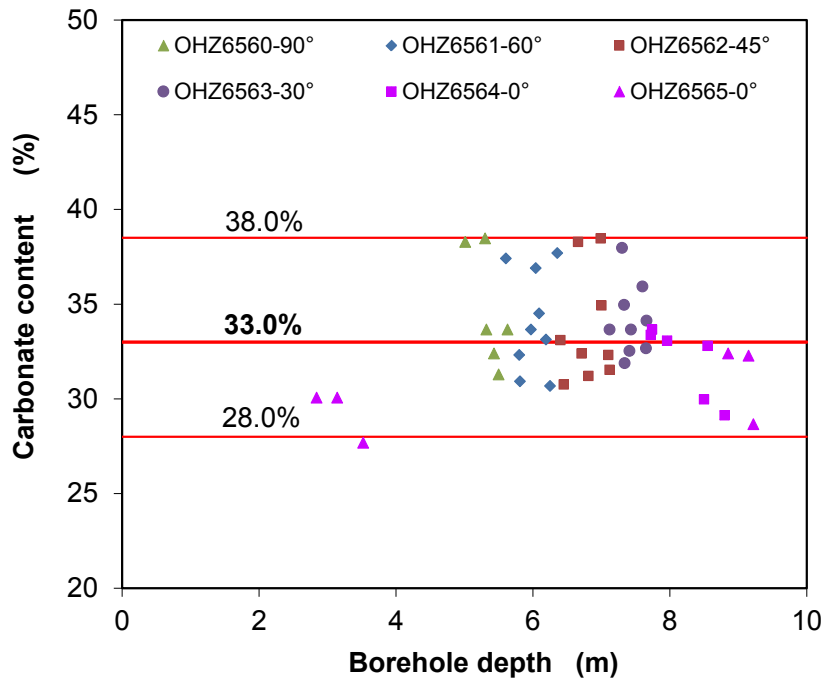


Fig. 2.4 Distributions of the main mineralogical components (clay, carbonate, quartz etc.) in the sampling region

2.3 Physical properties

The physical properties of the samples were determined according to testing methods suggested by ISRM (International Society for Rock Mechanics) /ISR 81/, including grain density, dry density, bulk density, porosity, water content, and degree of water saturation. The properties are defined as follows.

$$\text{Grain density: } \rho_s = \frac{M_s}{V_s} \quad (2.1)$$

M_s = mass of solids, V_s = volume of solids.

$$\text{Bulk density: } \rho_b = \frac{M}{V} = \frac{M_s + M_w}{V} \quad (2.2)$$

M = mass of bulk sample, V = volume of bulk sample,

M_s = mass of solids, M_w = mass of water.

$$\text{Dry density: } \rho_d = \frac{M_s}{V} \quad (2.3)$$

$$\text{Porosity: } \varphi = \frac{V_v}{V} = \left(1 - \frac{\rho_d}{\rho_s}\right) \quad (2.4)$$

V_v = volume of voids.

$$\text{Water content: } w = \frac{M_w}{M_s} \quad (2.5)$$

Degree of water saturation:

$$S_w = \frac{V_w}{V_v} = \frac{\rho_d \cdot w}{\rho_w \cdot \varphi} \quad (2.6)$$

ρ_w = density of pore water.

Before starting each test, the bulk density of the samples with natural water content was determined by measuring their volume and weight. The water content was measured on pieces remaining from sample preparation. They were dried in an oven at a temperature of 105 °C for 2 days. On basis of the measured bulk density and water content, the dry density was calculated. The grain density was measured on powder produced during sample preparation by use of pycnometer with helium gas. The porosity was calculated on basis of the measured grain and dry densities. The basic characteristics determined on the samples are summarized in Appendix C and in Fig. 2.5. As a result of the different mineralogical components and the different intensities of the disturbance by sampling, the physical properties are somewhat varying from one sample to another, and of course, do not exactly represent the original properties of the natural rock mass. The average properties determined on the samples are: grain densi-

ty $\rho_s = 2.70 \text{ g/cm}^3$, dry density $\rho_d = 2.25 \text{ g/cm}^3$, bulk density $\rho_b = 2.42 \text{ g/cm}^3$, porosity $\phi = 16.5 \%$, water content $w = 7.1 \%$ and water saturation degree $S_w = 96 \%$.

Generally, the inhomogeneous distributions of the mineralogical components and physical properties as well as the bedding planes make the clay rock heterogeneous and anisotropic in some degrees.

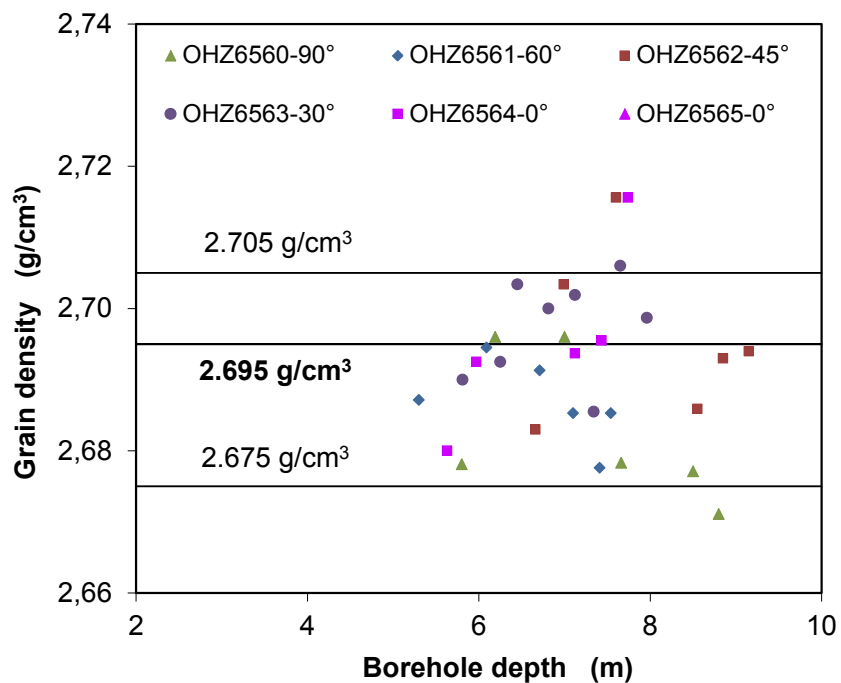


Fig. 2.5 Distributions of the physical properties in the sampling region

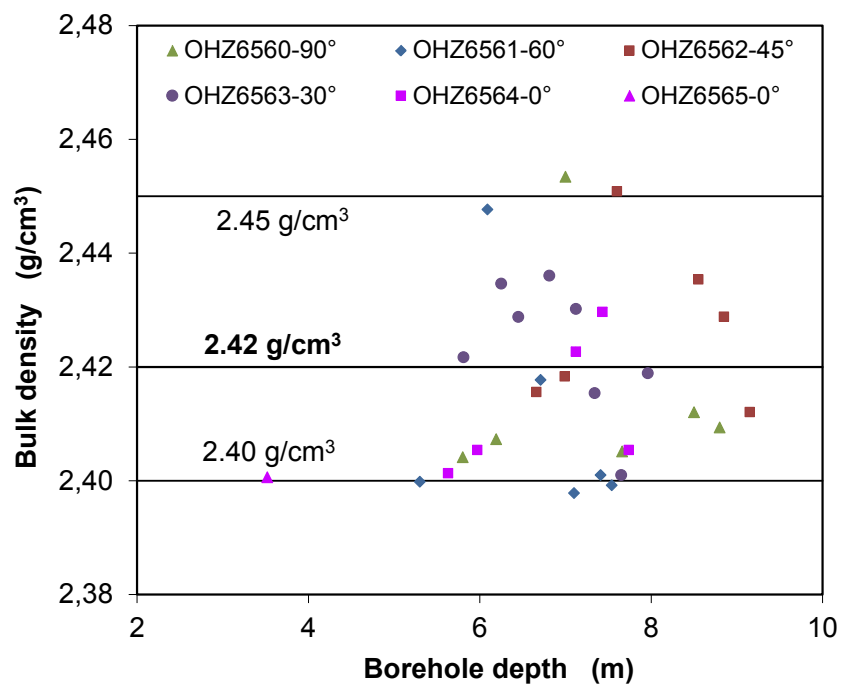
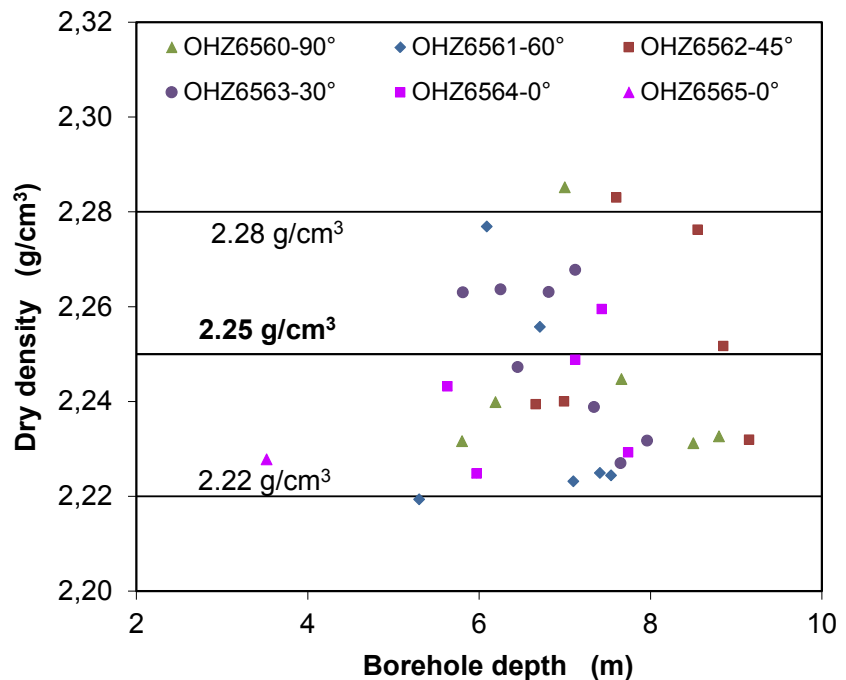


Fig. 2.5 Distributions of the physical properties in the sampling region

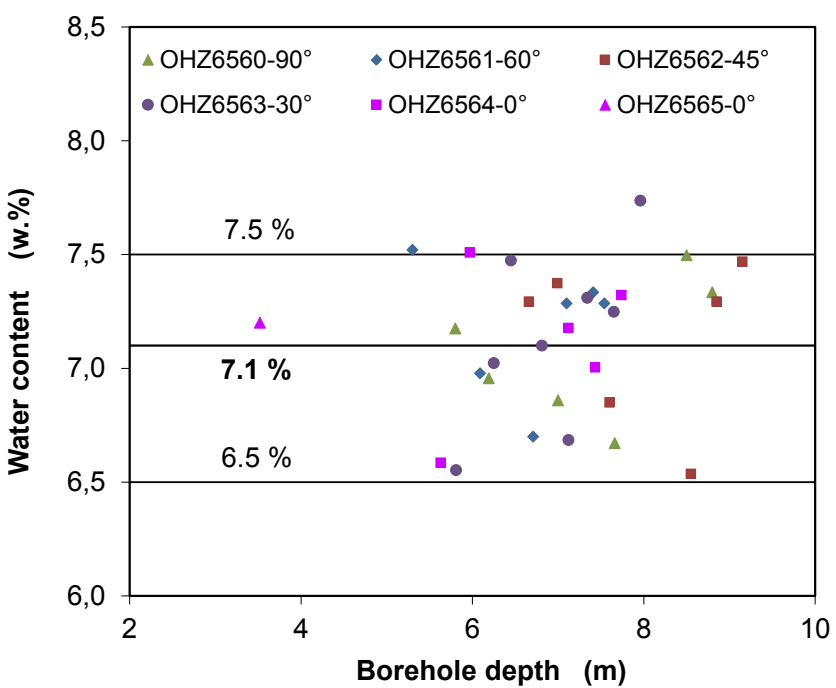
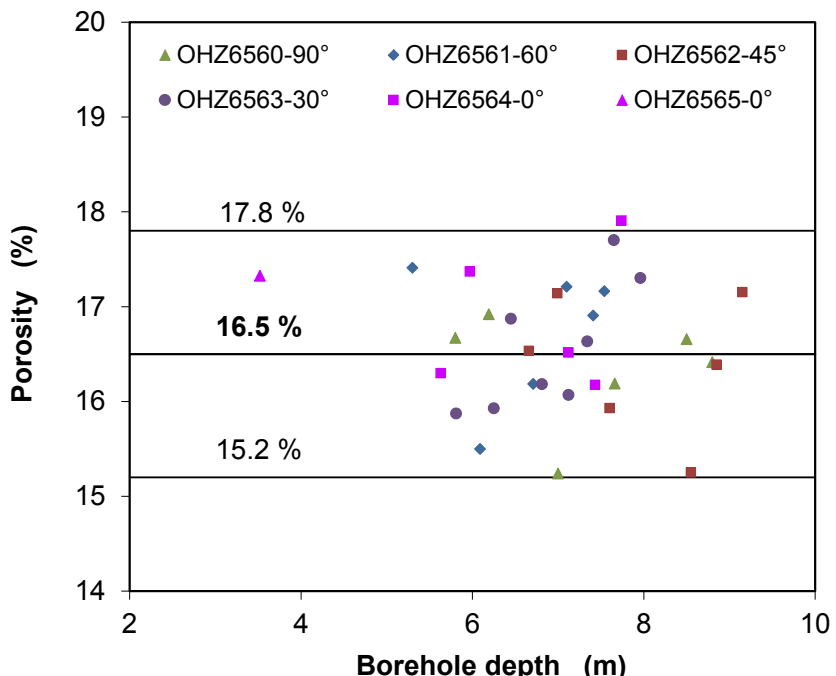


Fig. 2.5 Distributions of the physical properties in the sampling region

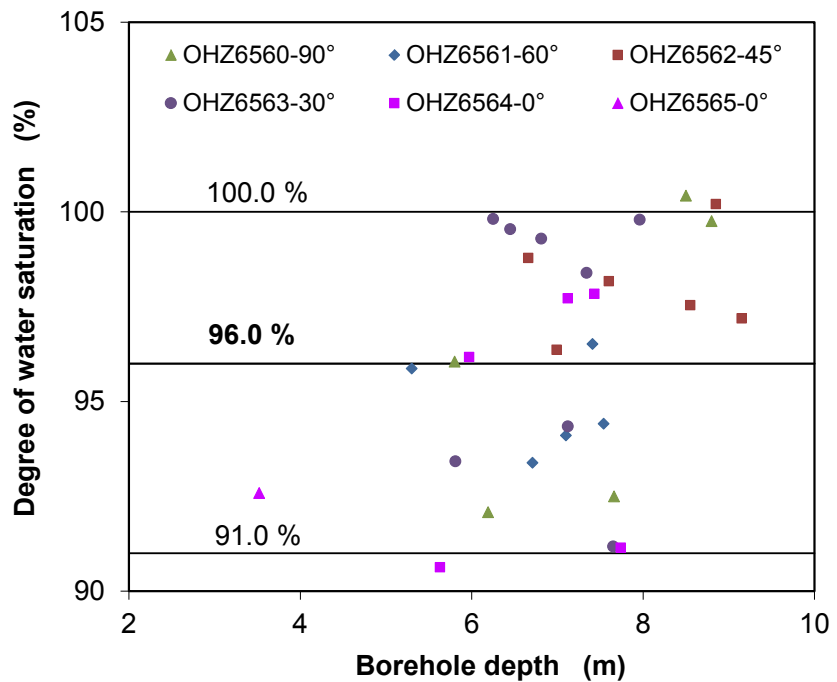


Fig. 2.5 Distributions of the physical properties in the sampling region

3 Laboratory experiments

3.1 Test programme

The mechanical anisotropy of the COX clay rock was investigated on the core samples under different triaxial load conditions. Five essential loading paths were applied, as illustrated in Fig. 3.1:

TCD – triaxial compression by axial deformation ε_a at constant radial stress σ_r ;

TCS – triaxial compression by axial loading σ_a at constant radial stress σ_r ;

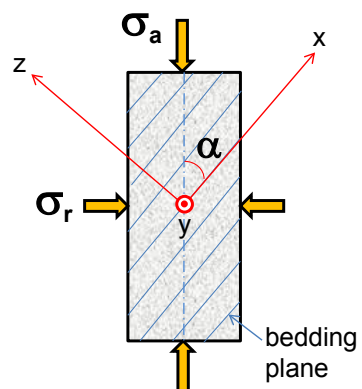
TES – triaxial extension by increasing radial stress σ_r at a constant axial stress σ_a ;

TEM – triaxial extension by keeping mean stress $\sigma_m = (\sigma_a + 2\sigma_r)/3$ constant with simultaneously increasing radial stress σ_r and decreasing axial stress σ_a ;

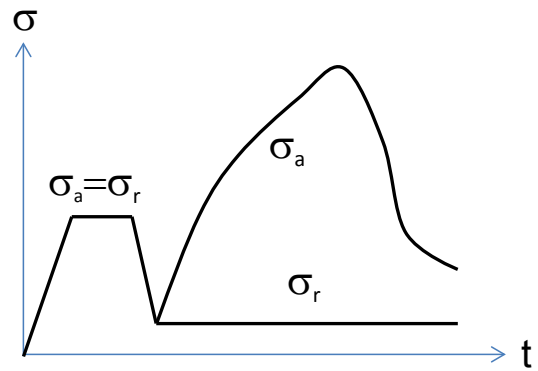
TCC – triaxial creep under multistep constant stress states, $\sigma_a = \text{const.}$ and $\sigma_r = \text{const.}$

A structural coordinate system is defined so that an axis z is normal to bedding planes and two orthogonal axes x and y are parallel to bedding. Loading orientation is defined by the angle α between the axial stress and the bedding planes. All the test types mentioned above were planned and carried out on the samples in each coring direction: $\alpha = 0^\circ, 30^\circ, 45^\circ, 60^\circ$ and 90° . The detailed test plan is given in Appendix D. Totally, 40 tests were successfully performed: 7 x TCD, 7 x TCS, 10 x TES, 10 x TEM, and 6 x TCC. A few other tests could not be conducted because the samples had been damaged during preparation.

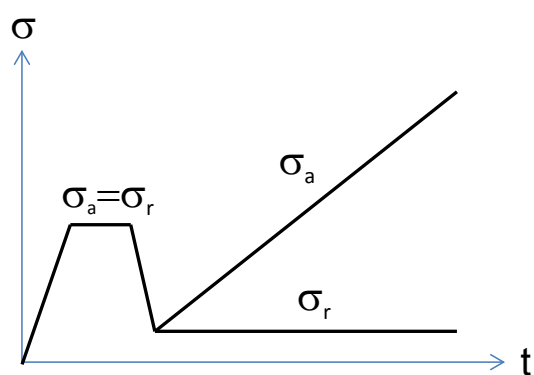
In order to minimize the effects of microcracks in the disturbed samples and to gather representative data for the intact clay rock, all samples were pre-compacted by hydrostatic loading up to 16 MPa, corresponding to the *in situ* maximum horizontal stress /AND 05/. The subsequent deviatoric loading was applied along each designed path at an identical confining stress: TCD and TCS at $\sigma_r = 5$ MPa, TES at $\sigma_a = 5$ MPa, TEM at $\sigma_m = 13.7$ MPa, TCC at $\sigma_r = 5$ MPa and $\sigma_a \geq 15$ MPa.



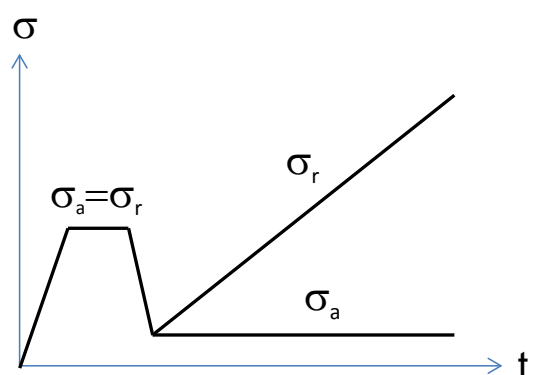
Coordinate system and load orientation



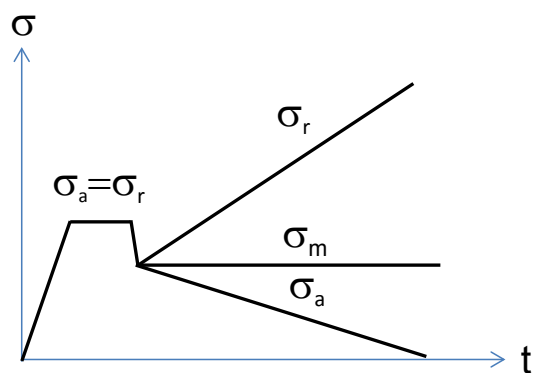
TCD: triaxial compression with strain control



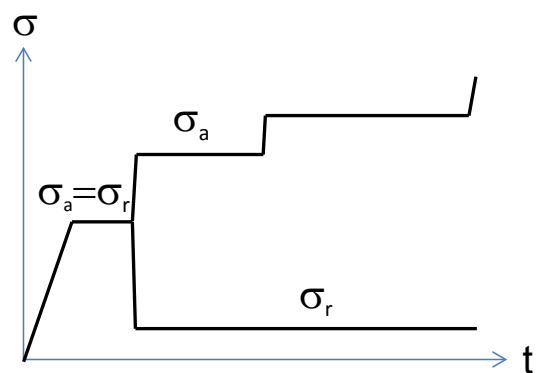
TCS: triaxial compression with stress control



TES: triaxial extension at constant axial stress



TEM: triaxial extension at constant mean stress



TCC: triaxial creep at multistep loads

Fig. 3.1 Schematic of designed loading paths

3.2 Test methods

The **TCD** triaxial compression tests focused on local strains oriented parallel and perpendicular to the bedding planes during deviatoric loading-unloading cycles. Tested

were samples ($d/l = 70\text{mm}/140\text{mm}$) with bedding orientations of $\alpha = 0^\circ$, 30° , 45° and 90° inclined to the axis. At a radial stress of $\sigma_r = 5 \text{ MPa}$, axial loading-unloading cycles were carried out within short ranges by axial deformation at rate of $\dot{\varepsilon}_a = \pm 1 \cdot 10^{-5} / \text{s}$. The loading-unloading cycles serve to determine influences of load magnitude and orientation on the elastic properties of the material. A Karman type triaxial testing apparatus was used, which allows instrumentation of two strain gauges for the measurement of the local strains. As shown in Fig. 3.2, both strain gauges were glued on the surface of each sample at its middle and oriented parallel and perpendicular to bedding planes respectively, namely $\varepsilon_{//}$ and ε_{\perp} . Additionally, a linear variable differential transducer (LVDT) was installed outside of the cell for axial strain ε_a over the entire sample with angle α to the bedding. The stiffness of the testing system was taken into account in evaluation of the ε_a -data. Based on the measured data $\varepsilon_{//}$, ε_{\perp} and ε_a , the radial strain ε_r and volumetric strain ε_v was approximately obtained by

$$\varepsilon_r = \frac{(\Delta\varepsilon_{r//} + \Delta\varepsilon_{r\perp})}{2} = \frac{(\Delta\varepsilon_{//}\sin\alpha + \Delta\varepsilon_{\perp}\cos\alpha)}{2} \quad (3.1)$$

$$\varepsilon_v = \varepsilon_a + 2\varepsilon_r \quad (3.2)$$

where $\varepsilon_{r//}$ and $\varepsilon_{r\perp}$ are the components of the measured strains $\varepsilon_{//}$ and ε_{\perp} in radial direction.

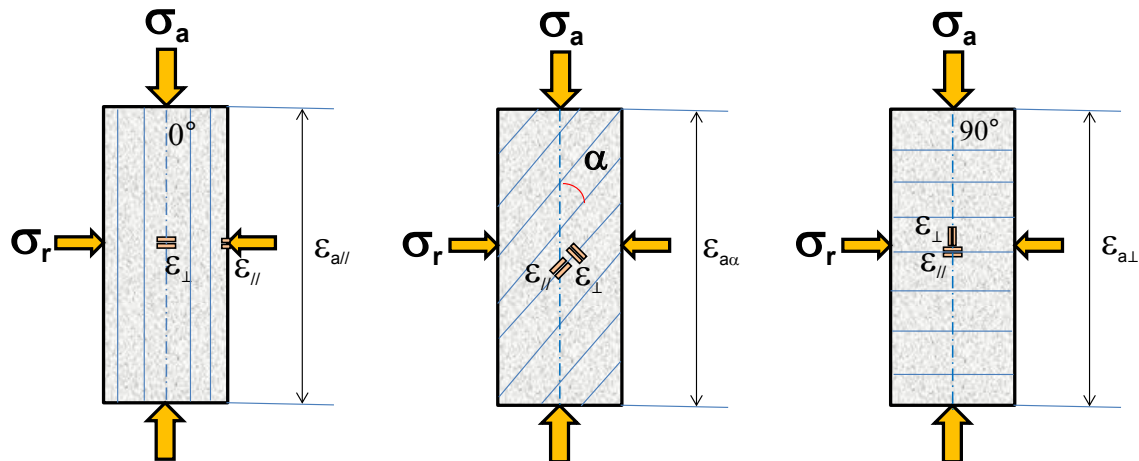


Fig. 3.2 Orientations of local strain measurements with respect to bedding planes

The **TCS**, **TES** and **TEM** tests aimed at estimating the strength anisotropy of the clay rock under triaxial compression and extension. For these tests, another triaxial testing apparatus was applied, which allows different loading paths such as compression, extension and torsion. Fig. 3.3 shows the assembly of a sample with instrumentation in

the triaxial cell. Tested were samples ($d/l = 50\text{mm}/100\text{mm}$) with bedding orientations of $\alpha = 0^\circ, 30^\circ, 45^\circ, 60^\circ$ and 90° inclined to the axis. For the TES and TEM extension tests, guard rings were installed between the load pistons and the sample end planes in order to prevent local damage of the rubber jacket due to possible separation between piston and sample during the axial elongation. Constant stress rates were controlled during each loading path: axial compression loading at $\dot{\sigma}_a = 0.007 \text{ MPa/s}$ and at $\sigma_r = 5 \text{ MPa}$ in TCS tests; radial compression loading at $\dot{\sigma}_r = 0.007 \text{ MPa/s}$ and at $\sigma_a = 5 \text{ MPa}$ in TES tests; radial compression and axial tension loading at $\dot{\sigma}_r = -\dot{\sigma}_a/2$ and at $\sigma_m = 13.7 \text{ MPa}$ in TEM tests. In each test, the axial strain ε_a was recorded using a LVDT transducer mounted inside the cell between the upper and lower loading piston, while radial strain ε_r was monitored by means of a circumferential extensometer chain mounted around the sample at its middle. The volumetric strain was calculated according to equation (3.2). During the TCS and TES tests, a unloading-reloading cycle was carried out at a stress difference of $\Delta\sigma = |\sigma_a - \sigma_r| = 10 \text{ MPa}$ to determine elastic parameters.

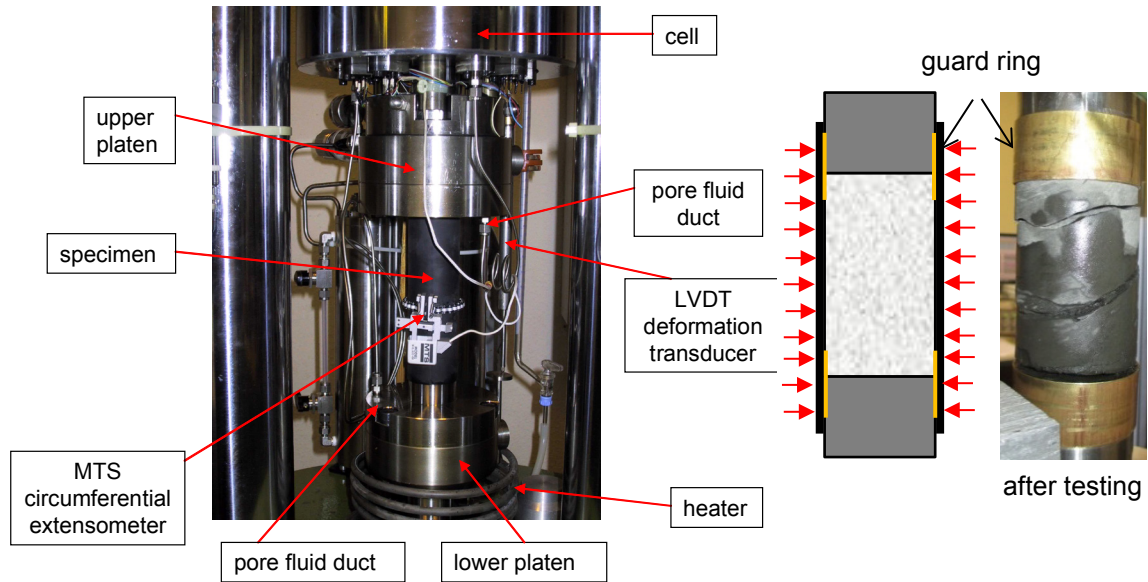


Fig. 3.3 Test set up for triaxial compression and extension testing

The **TCC** triaxial creep tests were designed to examine time effects on deformation and strength of the clay rock in different load orientations of $\alpha = 0^\circ, 30^\circ, 45^\circ, 60^\circ$ and 90° . A triaxial creep rig was used, which allows testing two samples of $d/l = 70\text{mm}/140\text{mm}$ simultaneously. Fig. 3.4 shows the creep rig with main components and instrumentations. The samples were placed in two separated triaxial cells and loaded at identical

axial stress adjusted by a syringe pump connected to the oil in the load piston. The lateral confining stress was applied independently to each sample using two individual syringe pumps. High axial stresses of $\sigma_a \geq 20$ MPa were stepwise applied up to failure at constant radial stress of $\sigma_r = 5$ MPa. In the tests, only axial strain was measured using individual LVDT deformation transducers.

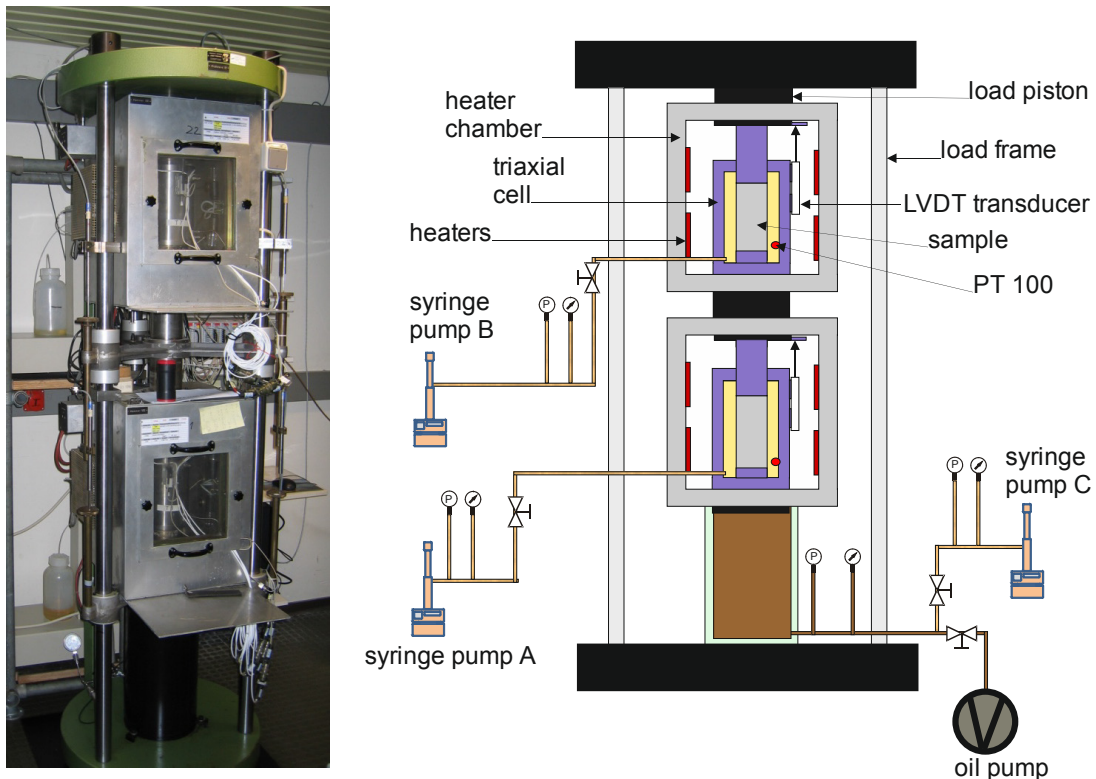


Fig. 3.4 Coupled rig for triaxial creep testing on two samples one upon another

It is to be pointed out that the test conditions are not hydraulically “undrained” because the samples were not fully water-saturated, even though they were sealed between rubber jackets and load pistons. Additionally, pore pressure was not monitored because of the difficulties of its accurate measurement in such highly consolidated claystones. So the total stress recorded during testing is applied in the following evaluation and analysis of the tests.

3.3 Test results

Test data obtained from the various tests are given in Appendix D in terms of the physical properties, stress-strain curves, elastic parameters, and strengths of the samples under different load conditions:

- App. D.1 for TCD - triaxial compression tests with strain control;
- App. D.2 for TCS - triaxial compression tests with stress control;
- App. D.3 for TES - triaxial extension tests by lateral compression at constant axial stress;
- App. D.4 for TEM - triaxial extension tests by lateral compression and axial tension at constant mean stress;
- App. D.5 for TCC - triaxial creep tests at multistep stresses.

Major findings are presented and discussed below.

3.3.1 Hydrostatic pre-compaction

All data of the hydrostatic pre-compaction are given in Tab. D.1 to D.4. They show that the applied maximum hydrostatic stress of 16 MPa almost completely closed up the microcracks in the disturbed samples. The total porosities measured decrease from the initial values of $\phi_0 = 16.5\% - 17.1\%$ to $\phi = 15.7\% - 16.6\%$. The differences of $\Delta\phi = 0.5\% - 1.0\%$ are attributed to the microcracks. In correspondence to the closure of the microcracks, the degrees of water saturation in the samples are rising from the initial values of $S_{wo} = 93\% - 97\%$ to $S_w = 97\% - 100\%$. Obviously, recompaction improves the quality of the samples significantly making them comparable to the intact claystone. However, the cohesion of the closed microcracks might not be fully recovered because they might be more or less desaturated due to the opening and the apertures could not be exactly rematched again under the applied load.

Moreover, the structural anisotropy of the clay rock can be characterised from the measured strains in the principal orientations perpendicular and parallel to the bedding planes. As typical examples, Fig. 3.5 shows the strains in three orientations of perpendicular, parallel and inclined to bedding (ε_\perp , ε_\parallel , $\varepsilon_{\alpha\alpha}$) during the hydrostatic loading and unloading for the axial load angles of $\alpha = 0^\circ$, 30° , 45° , and 90° .

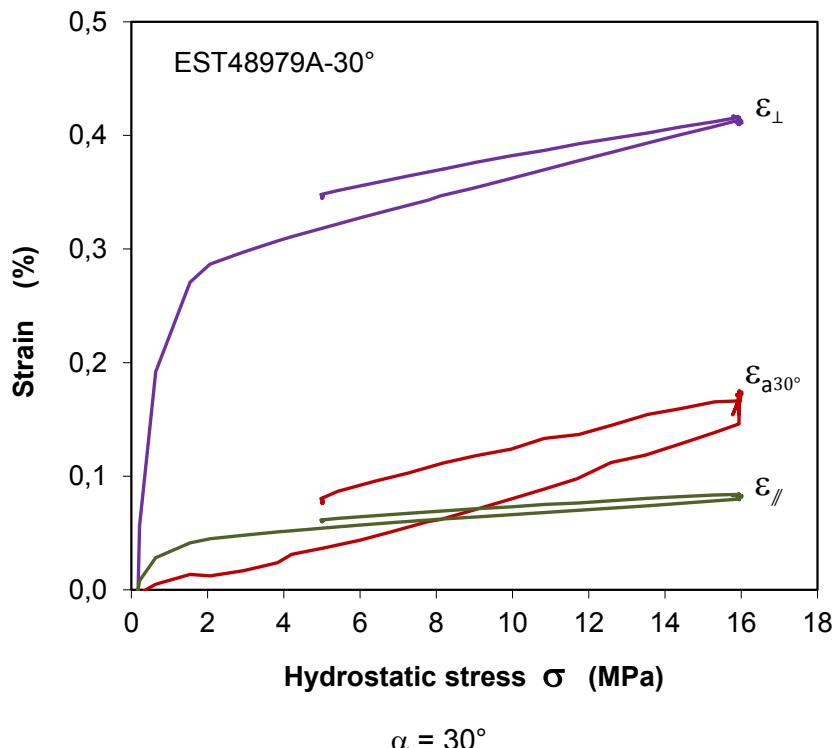
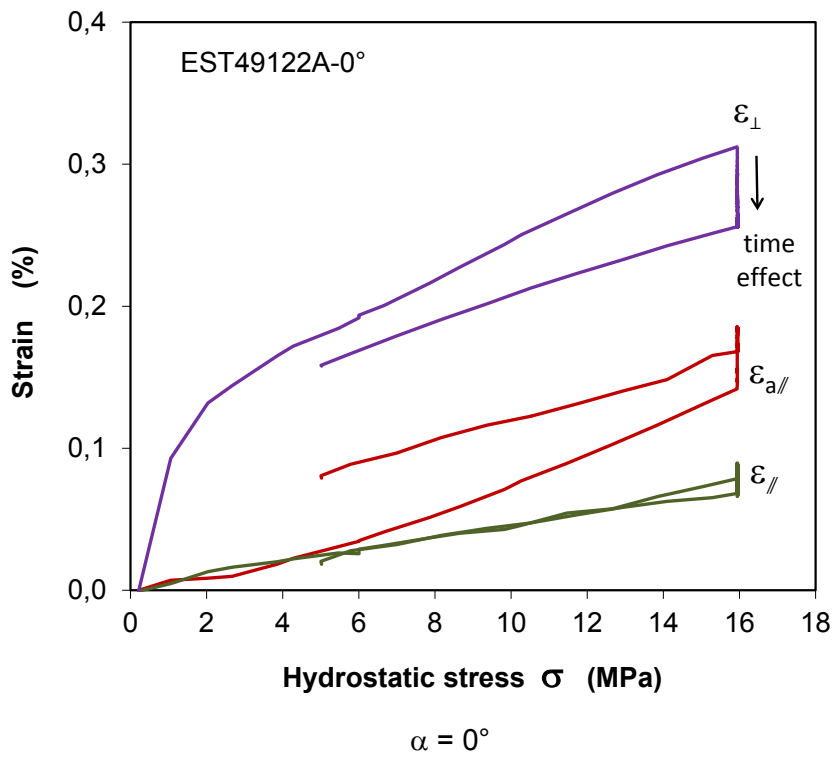


Fig. 3.5 Strains measured in orientations normal, parallel and inclined to bedding planes (ε_{\perp} , ε_{\parallel} , $\varepsilon_{a\alpha}$) during hydrostatic loading-unloading cycle

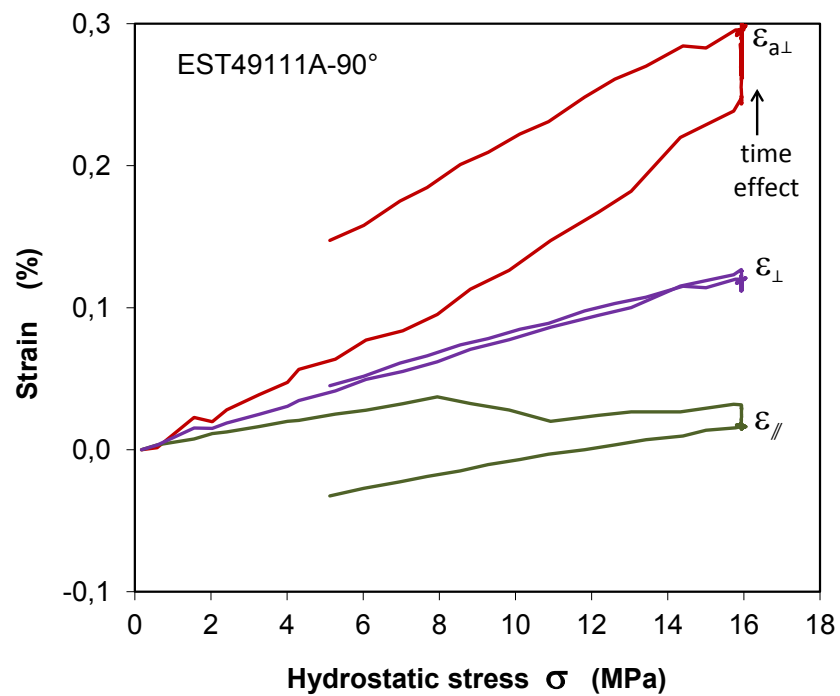
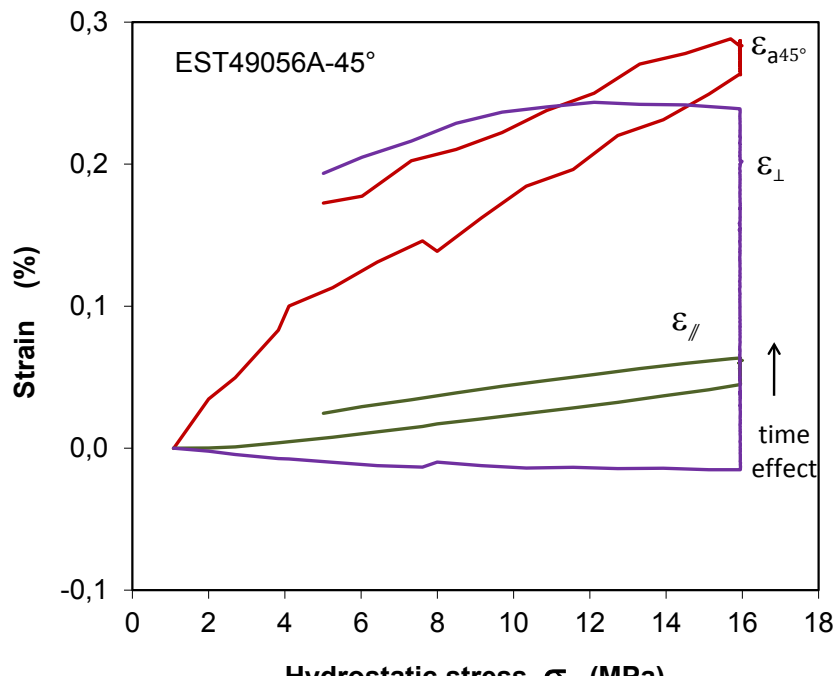


Fig. 3.5 Strains measured in orientations normal, parallel and inclined to bedding planes (ε_{\perp} , ε_{\parallel} , $\varepsilon_{\alpha\alpha}$) during hydrostatic loading-unloading cycle

The following main phenomena can be identified from the stress-strain curves:

- Hydrostatic loading leads to non-linear compressive strains in all directions. However, the strain normal to bedding ε_{\perp} is significantly larger than parallel to bedding ε_{\parallel} . The normal direction is the major opening direction of the microcracks.
- The global axial strains $\varepsilon_{a\parallel}$ and $\varepsilon_{a\perp}$ recorded on the samples with $\alpha = 0^\circ$ and $\alpha = 90^\circ$, respectively, are larger than those local values of ε_{\parallel} and ε_{\perp} measured on the sample surfaces. This could be attributed to some heterogeneity of the testing material on the one hand and to some errors of the testing system on the other hand such as imperfect contact between sample and piston.
- Taking into account the systematic difference, the strains in the bedding planes shall be isotropic (unfortunately it could not be measured due to instrumental limitations of the strain gauges used). That means that the mechanical behaviour in bedding planes is isotropic and the major anisotropic direction is normal to bedding. So the sedimentary clay rock can be considered a transversely isotropic material /SAR 07/, /YAN 13/, like the Opalinus clay /NAU 07/, /POP 07/, /BOC 10/ and the Tournemire shale /NIA 96/, /VAL 04/.
- Time effects can be identified during the compaction under the maximum constant load. However, due to the very small voids of the remaining microcracks they are considered to be insignificant.
- Note that the anisotropic deformation behaviour observed during the loading path is actually of significance for the disturbed samples rather than for the natural intact rock.
- Unloading leads to linear reversible strains in all directions. The stress-strain curves along the unloading path are represented again in Fig. 3.6 to highlight the structural anisotropy of the intact clay rock. The linear elastic strain normal to bedding is larger than parallel to bedding, $|\varepsilon_{\perp}| > |\varepsilon_{\parallel}|$. Taking into account the systematic difference between the local and global strains in axial direction, the elastic strains in orientations $0^\circ < \alpha < 90^\circ$ should lie between the values of normal and parallel to bedding, $|\varepsilon_{\parallel}| < |\varepsilon_{\alpha}| < |\varepsilon_{\perp}|$. The elastic deformability in the major and minor principal direction can be adopted for characterization of the structural anisotropy of the clay rock,

$$R_c = \frac{\Delta\varepsilon_{\perp}/\Delta\sigma}{\Delta\varepsilon_{\parallel}/\Delta\sigma} = \frac{\Delta\varepsilon_{\perp}}{\Delta\varepsilon_{\parallel}} \quad (3.3)$$

The R_c -values are calculated on the basis of the locally recorded strains during unloading. The mean value is obtained to $R_c = 2.2 \pm 0.48$, i.e., the elastic deformability in direction normal to bedding is about twice that in parallel direction.

Based on the volumetric strain from the unloading path, elastic bulk modulus of the clay rock can be obtained

$$K = \frac{\Delta\sigma}{\Delta\varepsilon_v} \quad (3.4)$$

The bulk modulus obtained is equal to $K = 5.6 \pm 1.5$ GPa in TCD tests, $K = 4.6 \pm 0.3$ GPa in TCS, $K = 4.6 \pm 0.5$ GPa in TES, and $K = 6.4 \pm 0.4$ GPa in TEM. The differences are relatively small. On average, $K = 5.5 \pm 0.6$ GPa is determined for the clay rock. As mentioned in /NIA 97/, the bulk modulus is not a representative material constant for anisotropic media. It can only be used when the anisotropy of the material is negligible.

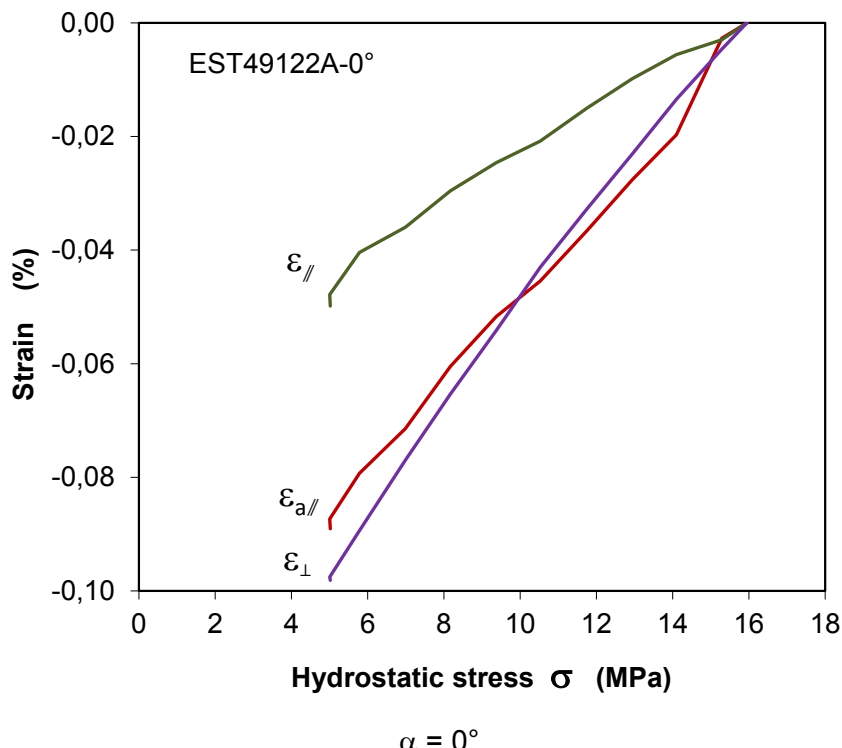


Fig. 3.6 Elastic strains measured in orientations normal, parallel and inclined to bedding planes (ε_{\perp} , ε_{\parallel} , $\varepsilon_{a\alpha}$) during hydrostatic unloading

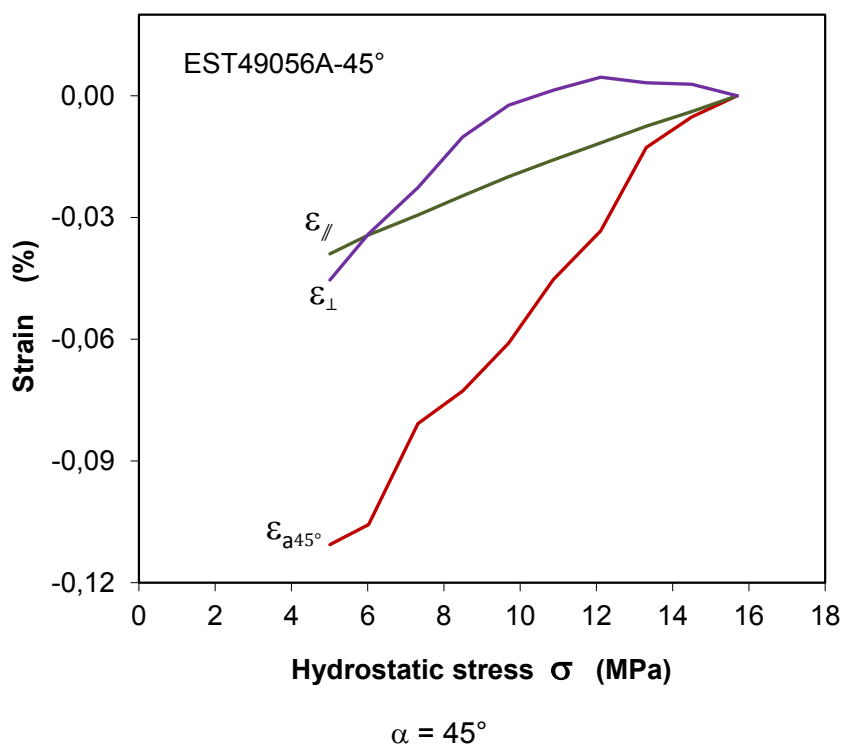
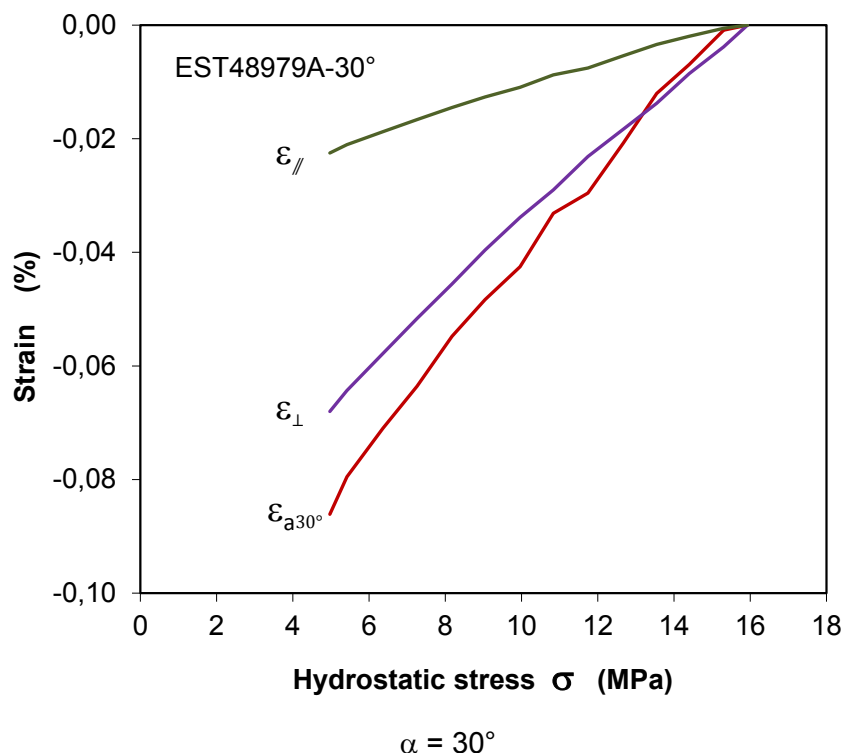


Fig. 3.6 Elastic strains measured in orientations normal, parallel and inclined to bedding planes (ε_{\perp} , ε_{\parallel} , $\varepsilon_{\alpha\alpha}$) during hydrostatic unloading

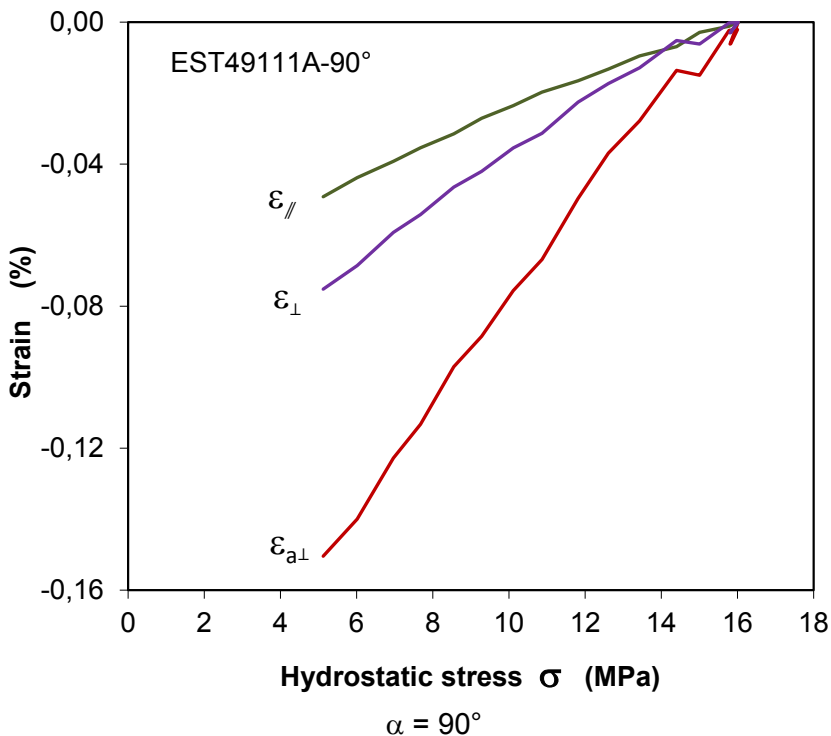


Fig. 3.6 Elastic strains measured in orientations normal, parallel and inclined to bedding planes (ε_{\perp} , ε_{\parallel} , $\varepsilon_{a\perp}$) during hydrostatic unloading

3.3.2 Triaxial compression at constant strain rate

The TCD triaxial compression tests were carried out with multiple loading-unloading cycles at axial strain rate of $\dot{\varepsilon}_a = \pm 1 \cdot 10^{-5} / s$ and at a radial stress of $\sigma_r = 5$ MPa. Each loading-unloading cycle was performed within a short range of $\Delta\sigma_a = 4$ MPa. Fig. 3.7 illustrates the typical stress-strain curves in orientations normal, parallel and inclined to bedding planes (ε_{\perp} , ε_{\parallel} , $\varepsilon_{a\alpha}$) for the axial load directions of $\alpha = 0^\circ$, 30° , 45° , and 90° with respect to the bedding.

All the curves show certain non-linearity of the stress-strain relationships, hysteresis in the unloading-reloading cycles and irreversibility of the strains after unloading. During axial loading in direction parallel to bedding ($\alpha = 0^\circ$), the transversely recorded strains show extension in both orientations normal and parallel to bedding. The magnitude of the normal extension ε_{\perp} is larger than the parallel extension, $|\varepsilon_{\perp}| > |\varepsilon_{\parallel}|$. This indicates that opening of bedding planes dominates. However, the opening of the bedding planes decreases with increasing the axial load angle to bedding. As $\alpha > 45^\circ$, the bed-

ding planes turn to close up, i.e., $\varepsilon_{\perp} > 0$. The maximum closure of the bedding planes is reached when the major principle load is normal to the bedding ($\alpha = 90^\circ$).

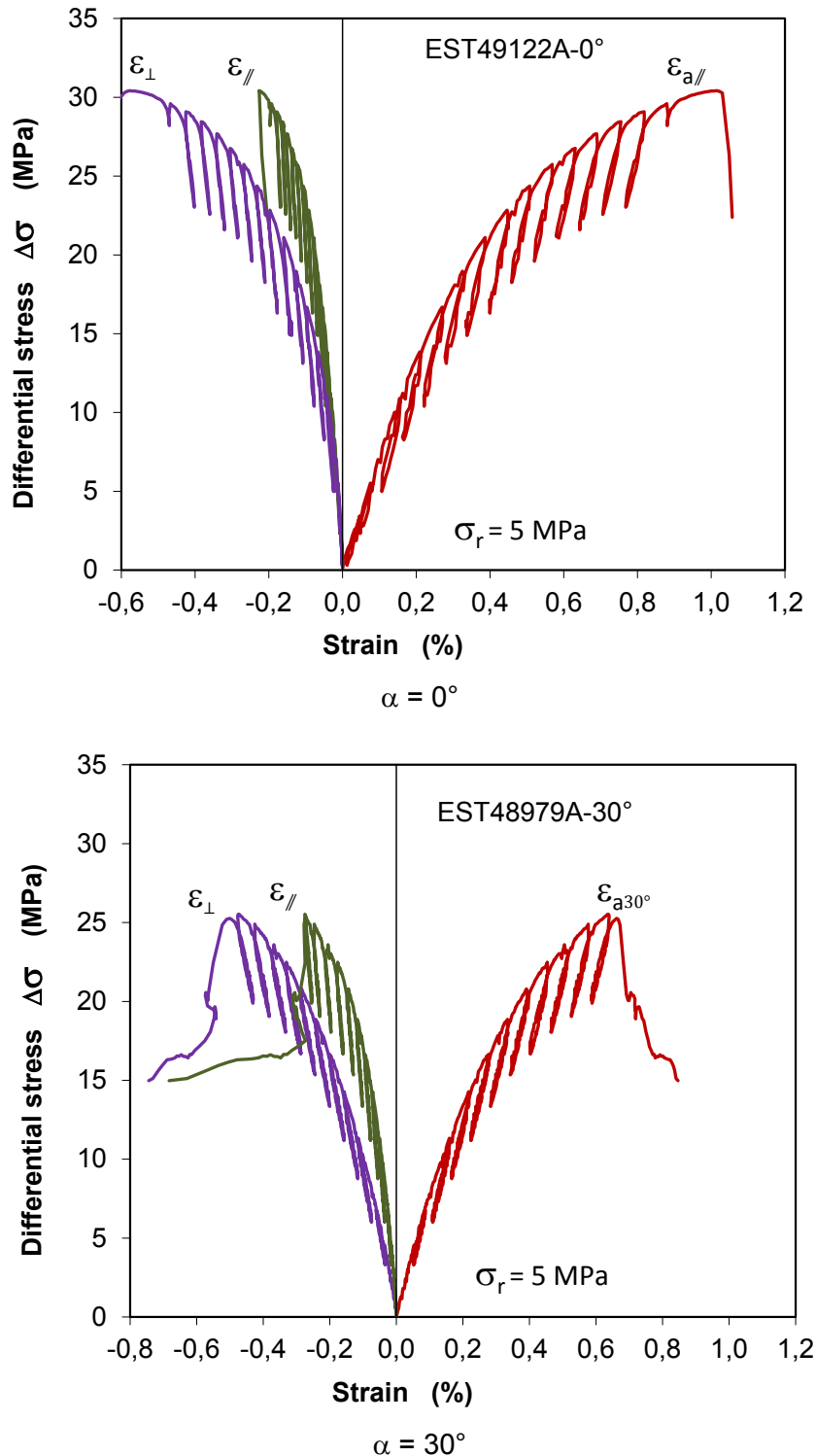


Fig. 3.7 Stress-strain curves obtained in directions normal, parallel and inclined to bedding planes ($\Delta\sigma-\varepsilon_{\perp}$, $\Delta\sigma-\varepsilon_{\parallel}$, $\Delta\sigma-\varepsilon_{a\alpha}$) during strain-controlled axial compression oriented at angles of $\alpha = 0^\circ$, 30° , 45° and 90° to bedding and at lateral stress of 5 MPa

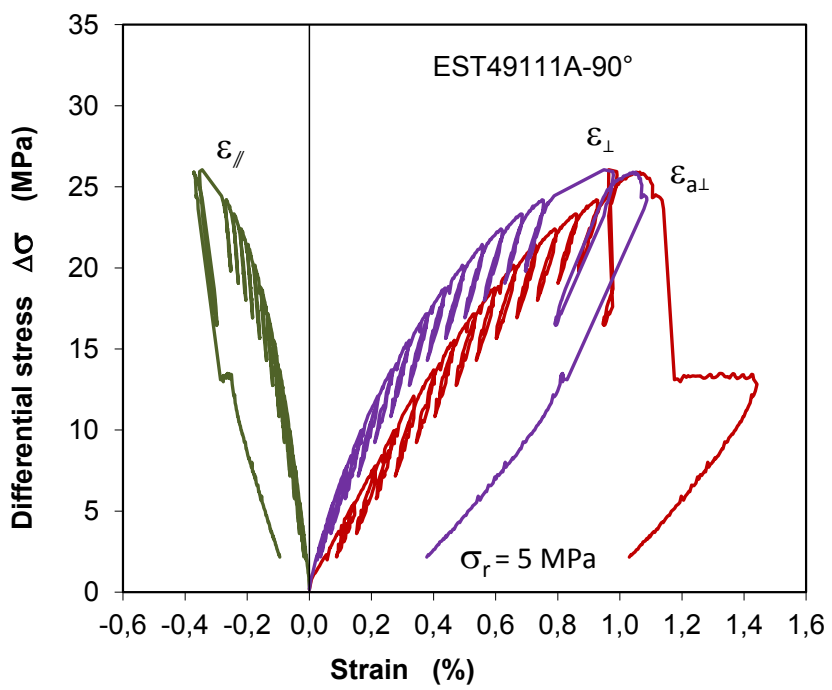
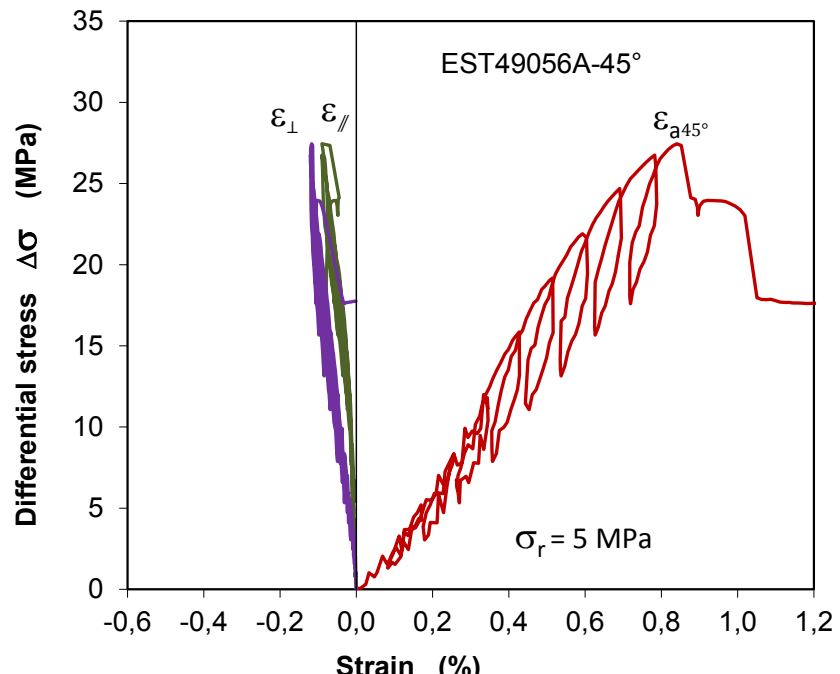


Fig. 3.7 Stress-strain curves obtained in directions normal, parallel and inclined to bedding planes ($\Delta\sigma-\varepsilon_\perp$, $\Delta\sigma-\varepsilon_\parallel$, $\Delta\sigma-\varepsilon_{aa}$) during strain-controlled axial compression oriented at angles of $\alpha = 0^\circ$, 30° , 45° and 90° to bedding and at lateral stress of 5 MPa

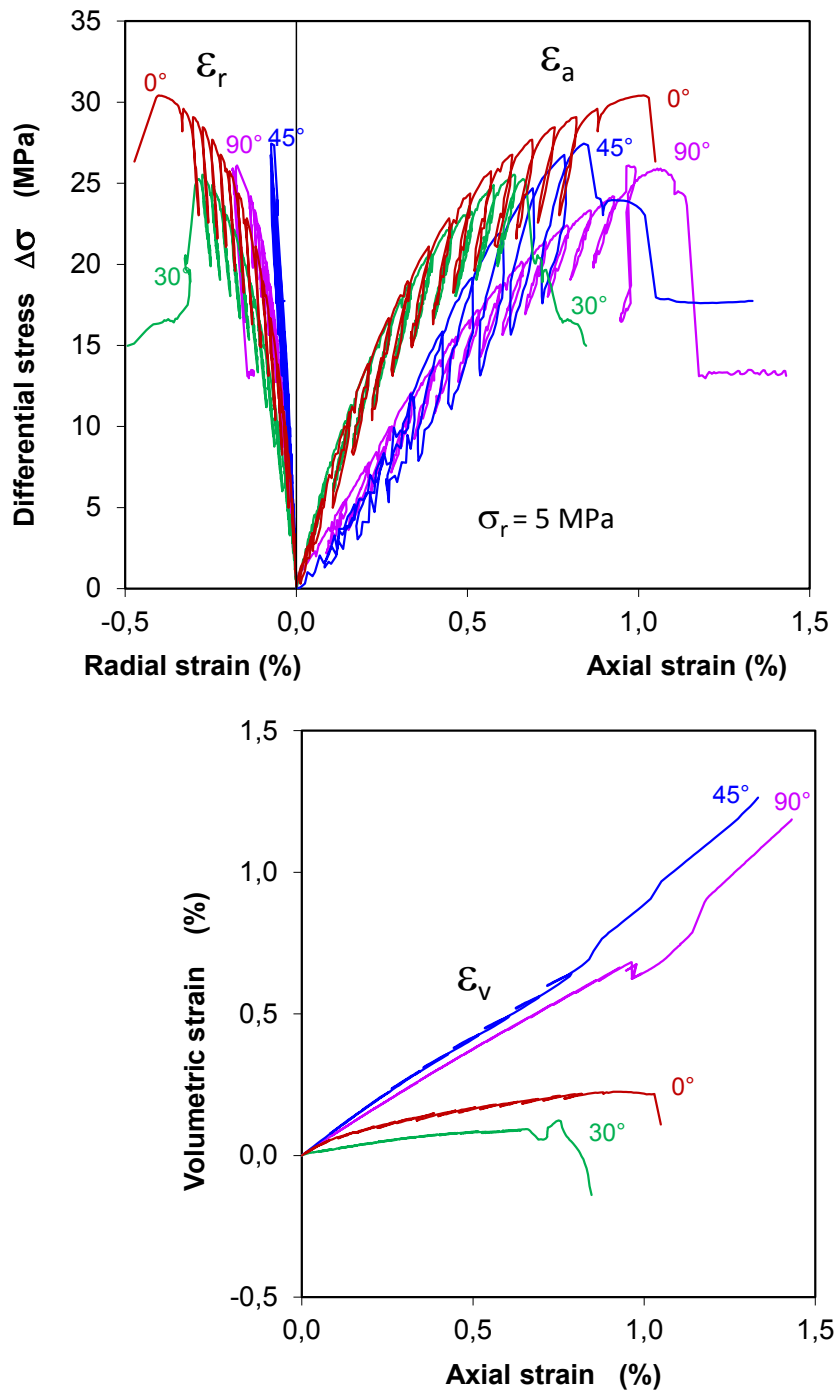


Fig. 3.8 Development of axial / radial / volumetric strains during strain-controlled axial compression oriented at angles of $\alpha = 0^\circ, 30^\circ, 45^\circ$ and 90° inclined to bedding and at lateral stress of 5 MPa

Based on the data of ε_{\perp} , ε_{\parallel} and ε_a , and according to equations (3.1) and (3.2), radial strain ε_r and volumetric strain ε_v can be obtained for each sample. Fig. 3.8 shows the differential stress – axial/radial/volumetric strain curves ($\Delta\sigma - \varepsilon_a$, $\Delta\sigma - \varepsilon_r$, $\varepsilon_v - \varepsilon_a$) for the

load orientations of $\alpha = 0^\circ$, 30° , 45° and 90° . The non-linearity of the stress-strain envelopes and the deformation anisotropy of the claystone are reflected again. Generally, the increase in differential stress ($\Delta\sigma = \sigma_a - \sigma_r$) results in axial compression, radial extension, and volume compaction until the brittle failure at the peak stress. The failure is accompanied by volume dilatancy in the samples at $\alpha = 0^\circ$ and 30° , while no dilatancy could be measured on the other samples at $\alpha = 45^\circ$ and 90° before the peak strength. Commonly, dilatancy or damage takes place due to the generation and accumulation of microcracks in such clay rocks under high deviatoric stresses close to the peak strength /NAU 07/, /POP 07/ and /ZHA 10/13/14/. The peak strengths and elastic parameters determined during the loading-unloading cycles will be presented and analysed later in section 3.4 together with other results from the TCS, TES, TEM and TCC tests.

3.3.3 Triaxial compression at constant stress rate

In addition to the strain-controlled triaxial compression tests (TCD) described above, another series of triaxial compression tests (TCS) was carried out with stress control by increasing axial load at a rate of $\dot{\sigma}_a = 0.007 \text{ MPa/s}$ and at radial stress of $\sigma_r = 5 \text{ MPa}$. Fig. 3.9 illustrates the stress-strain curves obtained on the samples in five load orientations of $\alpha = 0^\circ$, 30° , 45° , 60° and 90° . It is evident that the stress-strain curves are quite similar to the stress-strain envelopes of the multiple loading-unloading cycles in the strain-controlled TCD tests (cf. Fig. 3.8), i.e. non-linear stress-strain relations, irreversibility of the strains after unloading, no dilatancy before peak failure, and influence of the loading orientation on the strength. The elastic parameters were determined during an unloading-reloading cycle at $\Delta\sigma = 10 \text{ MPa}$. The characteristics of the stress-strain behaviour, including the elastic parameters, peak strengths and failure strains, will be presented and discussed later in section 3.4.

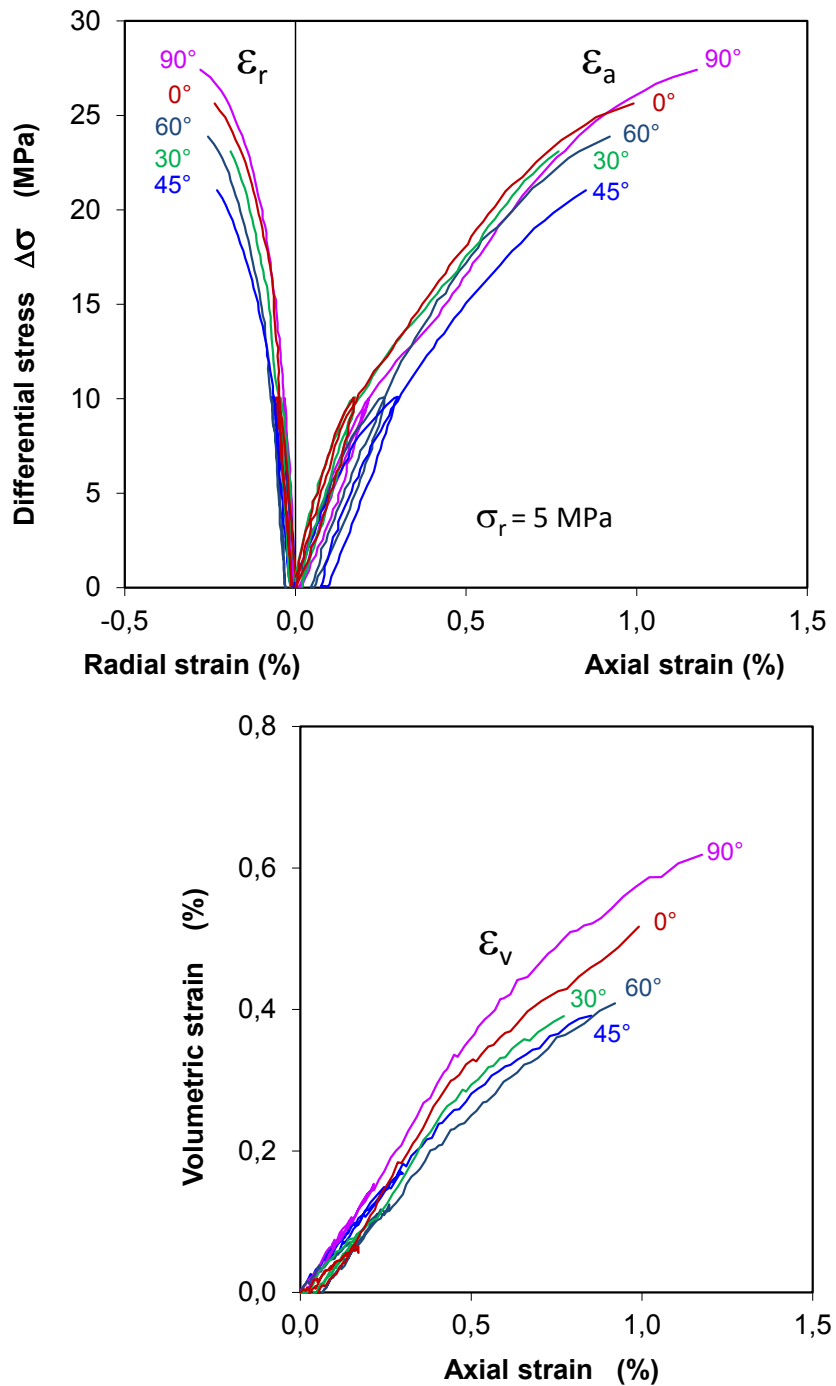


Fig. 3.9 Stress-strain curves obtained during stress-controlled axial compression oriented at angles of $\alpha = 0^\circ, 30^\circ, 45^\circ, 60^\circ$ and 90° inclined to bedding and at lateral stress $\sigma_r = 5 \text{ MPa}$

3.3.4 Triaxial extension by lateral compression at constant axial stress

The TES – triaxial extension tests were performed by increasing radial stress σ_r at a rate of $\dot{\sigma}_r = 0.007 \text{ MPa/s}$ and under constant axial stress of $\sigma_a = 5 \text{ MPa}$. The stress difference is defined here by $\Delta\sigma = \sigma_r - \sigma_a$. Fig. 3.10 illustrates the typical stress-strain curves obtained on the samples in five load orientations of $\alpha = 0^\circ, 30^\circ, 45^\circ, 60^\circ$ and 90° . As expected, axial elongation ($\varepsilon_a < 0$) occurs in the minor principle stress direction σ_a during the lateral compression ($\varepsilon_r > 0$). The strains are related non-linearly to the deviatoric stress. The volume is decreasing continuously with increasing the deviatoric loading until failure. The elastic stiffness was obtained during an unloading-reloading cycle at $\Delta\sigma = 10 \text{ MPa}$, which is referred here to $C = \Delta\sigma / \Delta\varepsilon_r$ (see App. D.3). The peak strengths and failure strains will be presented and analysed in section 3.4 with regard to loading directions.

3.3.5 Triaxial extension by lateral compression and axial tension

Another set of triaxial extension tests (TEM) was conducted at a constant mean stress $\sigma_m = 13.7 \text{ MPa}$, which was controlled by simultaneously increasing radial stress σ_r and decreasing axial stress σ_a with a load rate ratio of $\dot{\sigma}_r / \dot{\sigma}_a = -1/2$. Typical results are presented in Fig. 3.11. The samples deformed in radial compression and axial tension with a ratio of $\varepsilon_r / \varepsilon_a \approx 1/2$, almost in coincidence with the load ratio. The resultant volumetric compression is relatively small. Most samples showed no dilatancy before the peak failure, except for the sample at the load angle of $\alpha = 60^\circ$. Generally, the peak strengths reached during the TEM loading at constant mean stress are lower than those obtained during the TES loading at constant axial stress. Detailed discussions will be given later in section 3.4.

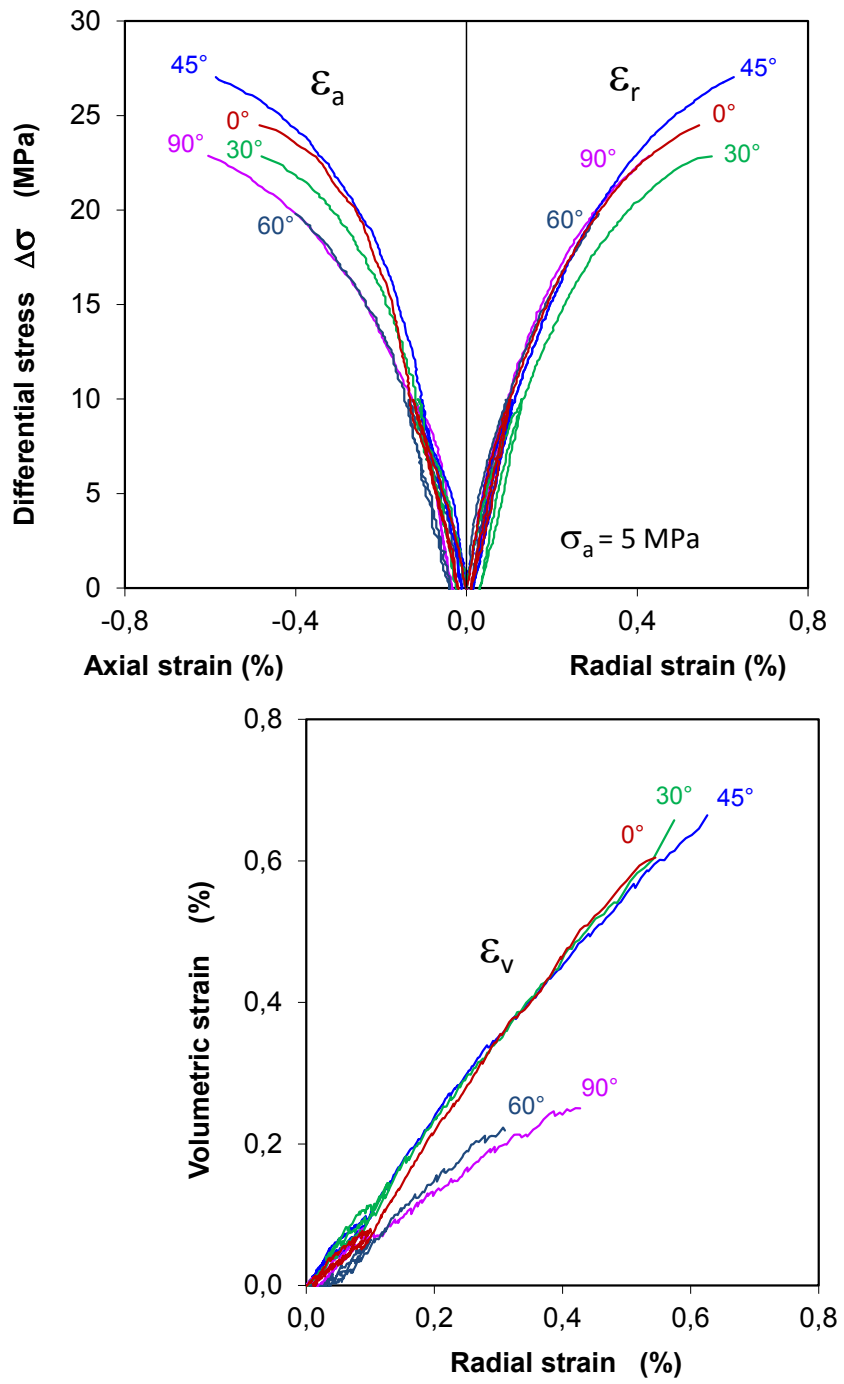


Fig. 3.10 Stress-strain curves obtained during lateral compression at constant axial stress $\sigma_a = 5 \text{ MPa}$ for the axial load angles of $\alpha = 0^\circ, 30^\circ, 45^\circ, 60^\circ$ and 90° inclined to bedding

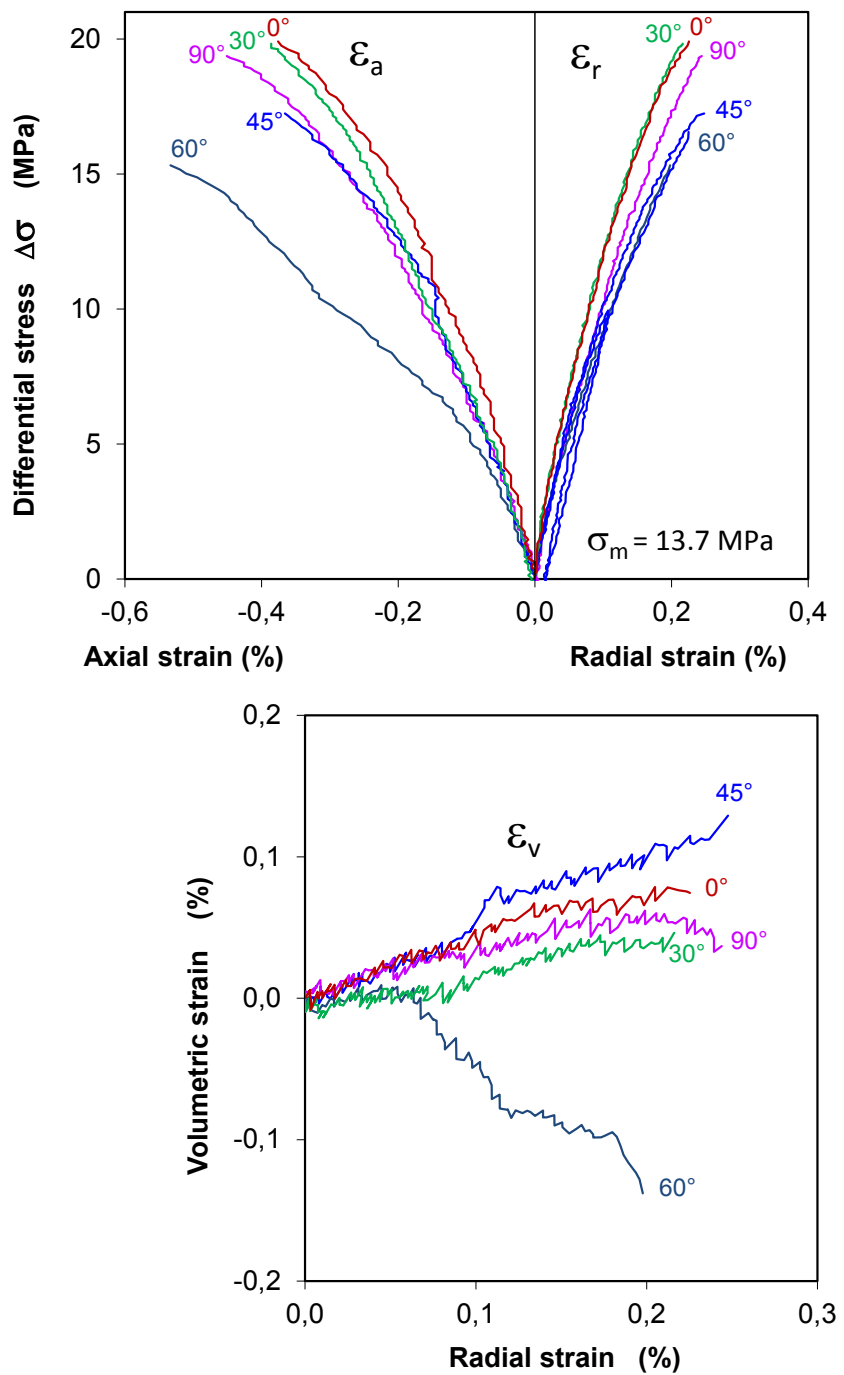
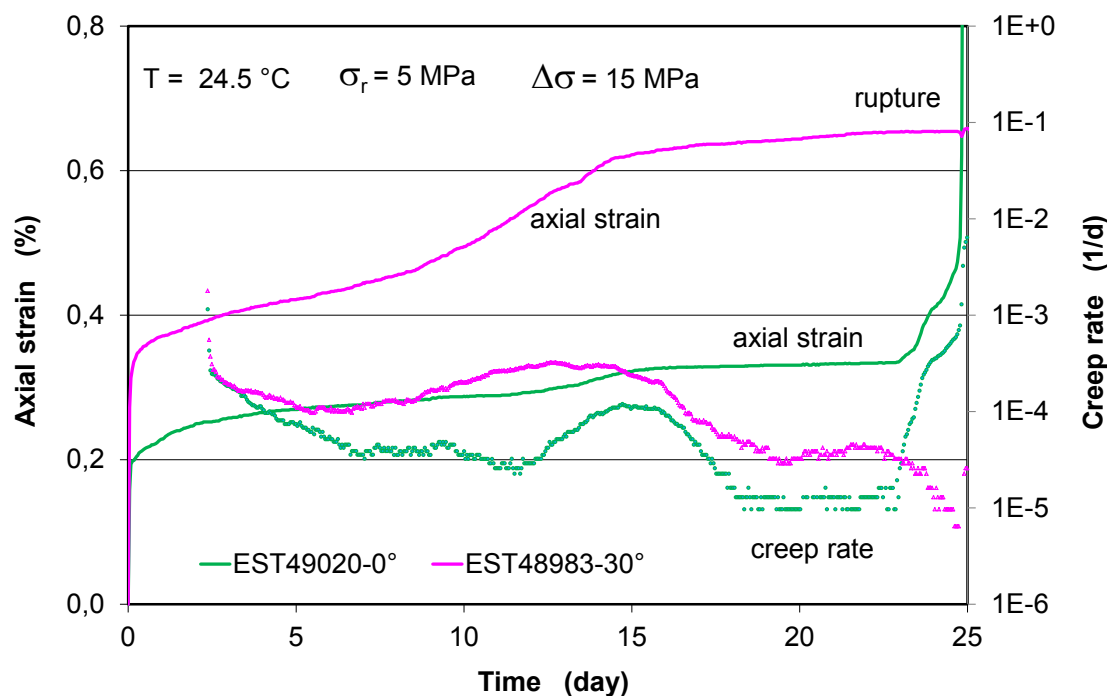


Fig. 3.11 Stress-strain curves obtained during lateral compression and axial extension at constant mean stress $\sigma_m = 13.7 \text{ MPa}$ for the axial load angles of $\alpha = 0^\circ, 30^\circ, 45^\circ, 60^\circ$ and 90° inclined to bedding

3.3.6 Triaxial creep under multistep stresses

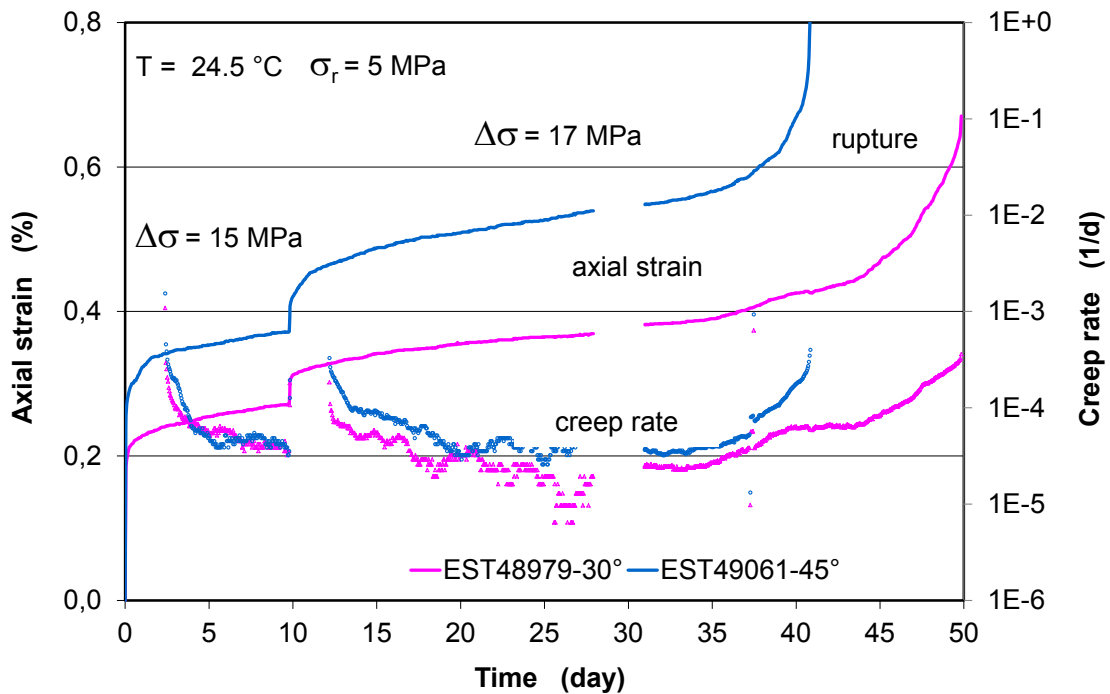
Time-dependent deformation and strength of the clay rock was investigated with triaxial creep tests (TCC) on the samples under multistep stresses for five load orientations of

$\alpha = 0^\circ, 30^\circ, 45^\circ, 60^\circ$ and 90° . The samples were firstly reconsolidated under a hydrostatic load of 16 MPa for 2 to 4 weeks. Following that, the stresses were adjusted to $\sigma_r = 5$ MPa and $\sigma_a = 20$ MPa within 30 minutes, and then $\sigma_a = 22$ MPa. The data obtained during the whole test procedure are summarized in App. E.5. Fig. 3.12 shows the measured evolution of axial strain and strain rate of the samples in three groups under the deviatoric loads. The radial and volumetric strains were not measured during the tests. The rapid loading resulted in a sudden increase in axial strain, which continued with time at $\sigma_r = 5$ MPa and $\sigma_a = 20$ MPa. Over 3 weeks, creep rupture took place at sample EST49020 subjected to the axial load parallel to the bedding planes. Unfortunately, this led also to the termination of the other test EST48983 in $\alpha = 30^\circ$ in the same group 1. In the other two groups, the second load phase was conducted at increased axial stress of $\sigma_a = 22$ MPa and at $\sigma_r = 5$ MPa. The resulting axial strains increased with time over more than a month and then accelerated rapidly to failure for all samples. The creep rates and failure stresses seem to be less dependent on the load orientations. Comparing with the short-term tests, the creep failure stresses are significantly lower.

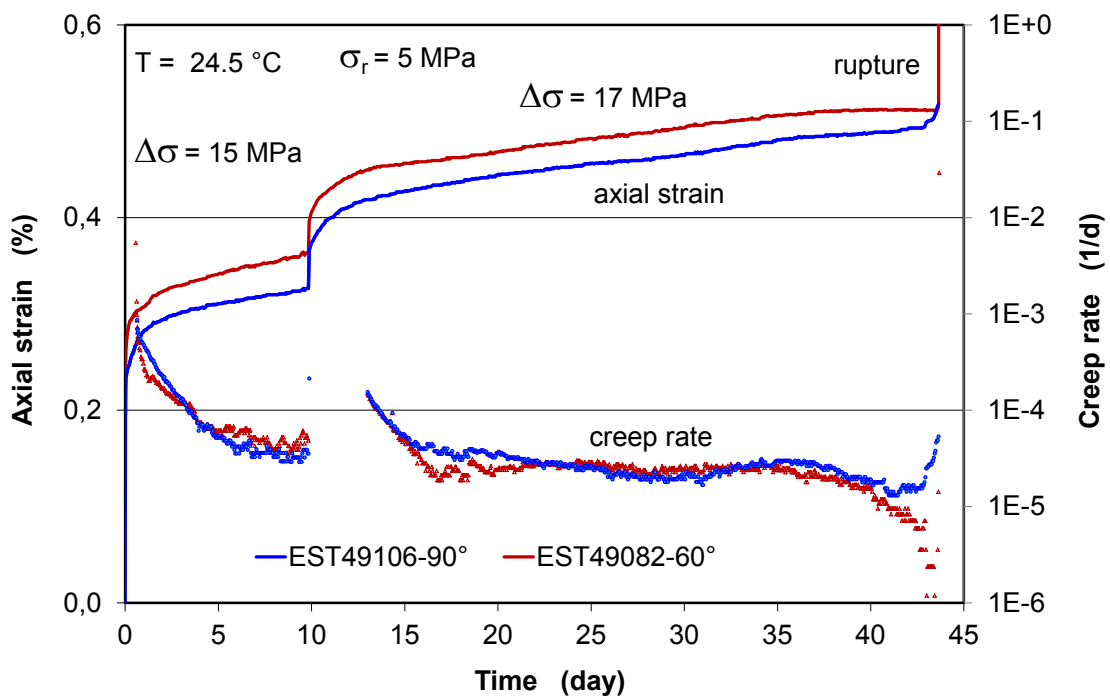


Group 1 with two samples at axial load angle of $\alpha = 0^\circ$ and 30°

Fig. 3.12 Evolution of axial strain and strain rate during the triaxial creep tests under multistep stresses of $\sigma_r = 5$ MPa and $\sigma_a = 20 / 22$ MPa and at axial load angles of $\alpha = 0^\circ, 30^\circ, 45^\circ, 60^\circ$ and 90° inclined to bedding



Group 2 with two samples at axial load angle of $\alpha = 30^\circ$ and 45°



Group 3 with two samples at axial load angle of $\alpha = 60^\circ$ and 90°

Fig. 3.12 Evolution of axial strain and strain rate during the triaxial creep tests under multistep stresses of $\sigma_r = 5 \text{ MPa}$ and $\sigma_a = 20 / 22 \text{ MPa}$ and at axial load angles of $\alpha = 0^\circ, 30^\circ, 45^\circ, 60^\circ$ and 90° inclined to bedding

3.4 Analysis of the test results

Based on the test results, the anisotropy of the mechanical behaviour of the COX clay rock will be analysed and discussed in terms of elastic deformability and failure strength as function of deviatoric stress, loading path and orientation with respect to the bedding planes.

3.4.1 Elastic properties

For the transversely isotropic clay rock, which is symmetric with respect to axis z in the coordinate system (x, y, z) defined in Fig. 3.13 (see also Fig. 3.1), the elastic stress-strain relationship is given by Hook's law:

$$\begin{bmatrix} \varepsilon_x \\ \varepsilon_y \\ \varepsilon_z \\ \gamma_{xy} \\ \gamma_{yz} \\ \gamma_{zx} \end{bmatrix} = \begin{bmatrix} \frac{1}{E_1} & -\frac{\nu_1}{E_1} & -\frac{\nu_2}{E_2} & 0 & 0 & 0 \\ -\frac{\nu_1}{E_1} & \frac{1}{E_1} & -\frac{\nu_2}{E_2} & 0 & 0 & 0 \\ -\frac{\nu_2}{E_2} & -\frac{\nu_2}{E_2} & \frac{1}{E_2} & 0 & 0 & 0 \\ 0 & 0 & 0 & \frac{2(1+\nu_1)}{E_1} & 0 & 0 \\ 0 & 0 & 0 & 0 & \frac{1}{G_2} & 0 \\ 0 & 0 & 0 & 0 & 0 & \frac{1}{G_2} \end{bmatrix} \begin{bmatrix} \sigma_x \\ \sigma_y \\ \sigma_z \\ \tau_{xy} \\ \tau_{yz} \\ \tau_{zx} \end{bmatrix} \quad (3.5)$$

In this equation, σ_i and ε_i ($i = x, y, z$) are the normal stress and strain in the i direction respectively; τ_{ij} and γ_{ij} ($i, j = x, y, z$ and $i \neq j$) denote the shear stress and strain in the plane (i, j) . The elastic compliance matrix is related to five independent parameters: E_1 and E_2 are Young's moduli parallel and normal to the bedding planes respectively; ν_1 and ν_2 are the lateral expansion coefficients (Poisson's ratio) parallel to the bedding under compressive loading in direction parallel and normal to the bedding respectively; G_2 is the shear modulus for planes containing the normal to the bedding. According to WIT 84/, the elastic parameters for a transversely isotropic medium are defined in Fig. 3.13.

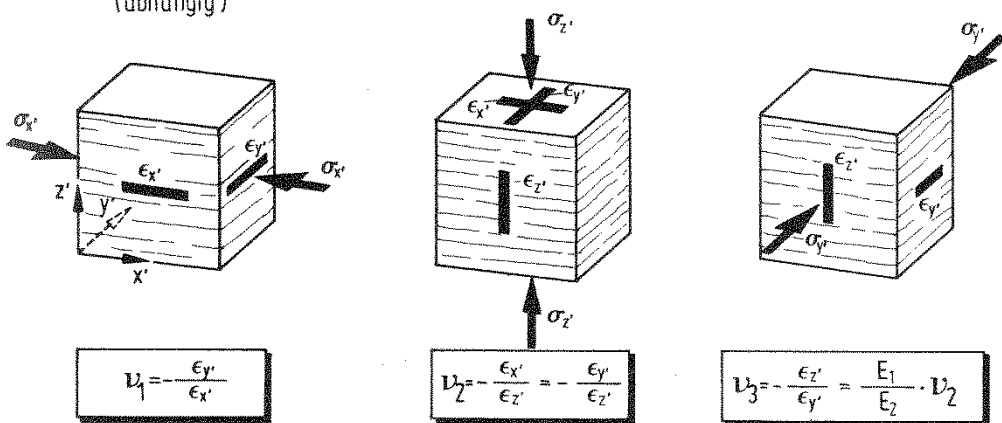
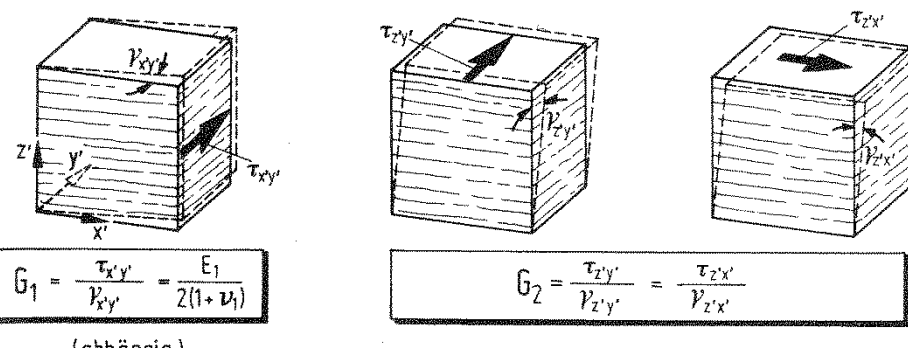
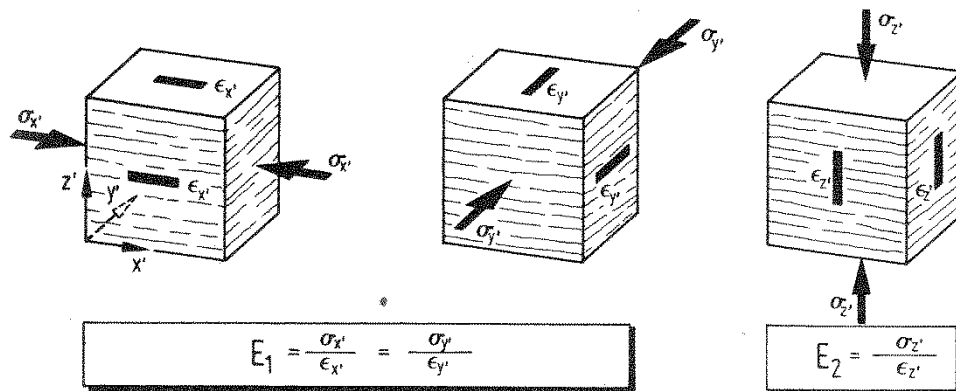
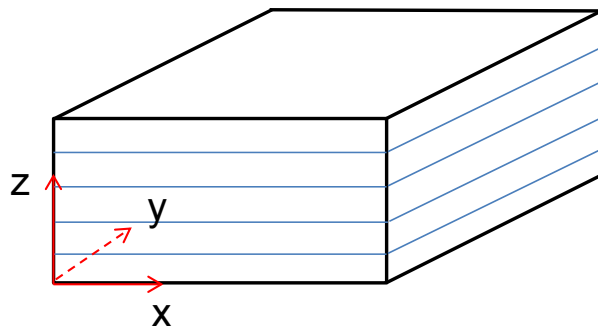


Fig. 3.13 Definition of the elastic parameters for a transversely isotropic rock with bedding planes (after /WIT 84/)

Elastic properties of a rock are generally dependent upon applied load. In order to investigate the variations of the elastic parameters of the clay rock with stress, multiple loading-unloading cycles were conducted in the TCD – triaxial compression tests (section 3.3.2). From the stress-strain curves obtained along the loading and unloading path, one can determine the elastic Young's modulus E and Poisson's ratio ν by

$$E = \frac{\Delta\sigma_a}{\Delta\varepsilon_a} \quad (3.6)$$

$$\nu = -\frac{\Delta\varepsilon_r}{\Delta\varepsilon_a} \quad (3.7)$$

According to the approach applied in /NIA 97/, the Young's moduli E_1 and E_2 are determined from the tests performed in $\alpha = 0^\circ$ and $\alpha = 90^\circ$ respectively. Similarly, Poisson's ratio ν_1 is determined from the tests in $\alpha = 0^\circ$ ($\nu_1 = -\Delta\varepsilon_{r\parallel}/\Delta\varepsilon_{a\parallel}$), while ν_2 can be obtained from the tests in $\alpha = 0^\circ$ ($\nu_2 = -\Delta\varepsilon_{r\perp}/\Delta\varepsilon_{a\perp}$) and/or from the tests in $\alpha = 90^\circ$ ($\nu_2 = -\Delta\varepsilon_{r\parallel}/\Delta\varepsilon_{a\parallel}$). Finally, the shear modulus G_2 can be derived from any tests performed in an out-of-axis orientation:

$$\frac{1}{E_\alpha} = \frac{\sin^4\alpha}{E_2} + \left[\frac{1}{G_2} - 2\frac{\nu_2}{E_2} \right] \cdot \sin^2\alpha \cdot \cos^2\alpha + \frac{\cos^4\alpha}{E_2} \quad (3.8)$$

where E_α is the axial Young's modulus determined from a test performed in the α direction ($0^\circ < \alpha < 90^\circ$), and thus G_2 is deduced from this equation. There are also some simple formulas available for approximately estimating G_2 /WIT 84/, for instance, the Saint-Venant's formula used in /NIA 97/:

$$\frac{1}{G_2} = \frac{1}{E_1} + \frac{1}{E_2} + 2\frac{\nu_2}{E_2} \quad (3.9)$$

The measured elastic parameters are plotted in Fig. 3.14 for Young's moduli E_1 and E_2 and in Fig. 3.15 for Poisson's ratios ν_1 and ν_2 as a function of applied deviatoric stress. It is obvious that the parameters are not constant but vary with the stress.

Both Young's modulus E_1 parallel and E_2 normal to bedding are increasing with deviatoric stress in the beginning before $\Delta\sigma < 10-12$ MPa, due to the hardening effect with volume compaction. With further increase in the stress until the peak σ_F , the Young's moduli do not change much. The values determined from unloading path are slightly higher than those from loading path. Additionally, the data also vary from a sample to

another due to the differences in the characteristics. The mean curves of E_1 and E_2 vs. $\Delta\sigma$ are derived by averaging the data. The maximum values are reached at $\Delta\sigma \approx 25$ MPa before failure, on average $E_1 = 10$ GPa and $E_2 = 6.3$ GPa. The relatively high Young's modulus E_1 parallel to bedding is due to the higher density of the claystone along the bedding.

The Poisson's ratio ν_2 normal to bedding obtained on samples EST49122A/B in $\alpha = 0^\circ$ increases with stress, while ν_1 parallel to bedding does not change much. The significant increase in ν_2 may be related to the progressive increase in the opening of bedding planes with stress. Because of the different features between samples, the ν_2 -values obtained in $\alpha = 0^\circ$ are differing from one to another. For instance, the ν_2 -values of sample EST49122A are larger than those of sample EST49122B, even though both positioned closely. The averaged maximum values are reached at $\Delta\sigma = 25$ MPa to $\nu_2 = 0.45$ for EST49122A and $\nu_2 = 0.34$ for B. Additionally, the ν_2 -values obtained in load direction parallel to bedding ($\alpha = 0^\circ$) and normal to bedding ($\alpha = 90^\circ$) are not consistent. The $\nu_2\Delta\sigma$ curves in $\alpha = 0^\circ$ on samples EST49122A/B-0° are higher than those in $\alpha = 90^\circ$ on the others EST49111A/B-90°.

Taking the mean curves of E_1 / E_2 and ν_1 / ν_2 represented in Fig. 3.16, one can derive the shear modulus G_2 according to equation (3.8), provided that the axial Young's modulus E_α is determined from a test performed in the α direction. In contrast, the simplified equation (3.9) does not require the data of E_α . Based on the TCD tests in $\alpha = 30^\circ$ and $\alpha = 45^\circ$, the axial Young's moduli E_{30° and E_{45° are obtained and plotted in Fig. 3.17 as a function of deviatoric stress. Both show the same behaviour like E_1 and E_2 . The shear modulus G_2 calculated according to equations (3.8) and (3.9) are plotted in Fig. 3.18 for $\alpha = 30^\circ$ and $\alpha = 45^\circ$ together with averaged Young's moduli E_1 , E_2 and E_α . The relatively high initial value of E_{30° leads to a large G_2 value according to (Eq. 3.8), while the G_2 based on E_{45° shows the similar dependence on the deviatoric stress like the Young's moduli. Compared with the G_2 -values according to (Eq. 3.8), the simplified Saint-Venant's formula (Eq. 3.9) underestimates G_2 for the clay rock. However, the Saint-Venant's formula was validated for the Tournemire shale in /NIA 97/. Again, because of the different features of the samples, the G_2 -values based on E_{30° at sample EST48979A and E_{45° at EST49056A are different. These G_2 -values are averaged and summarized in Tab. 3.1 together with the other parameters as a function of deviatoric stress.

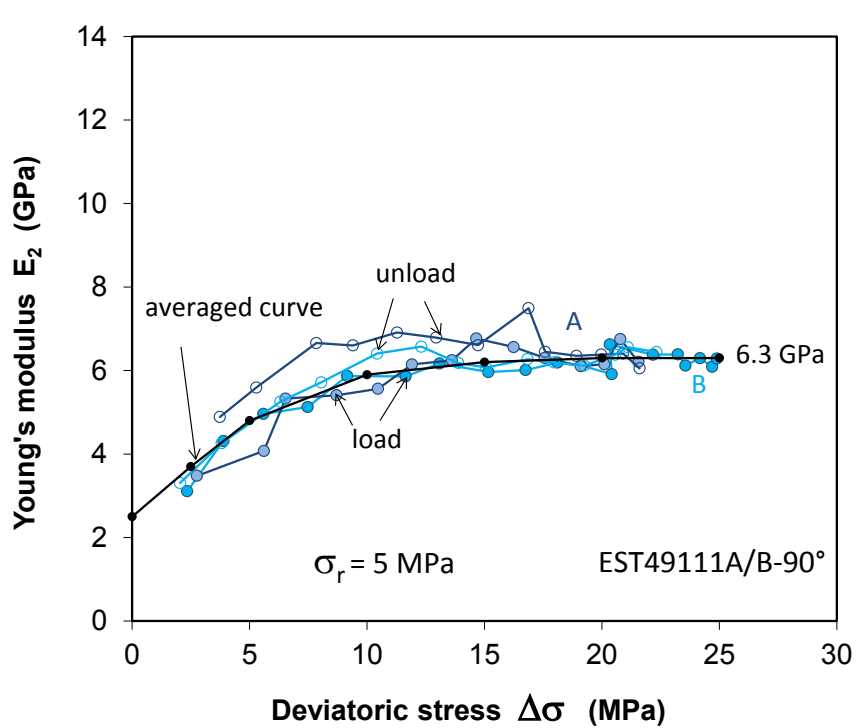
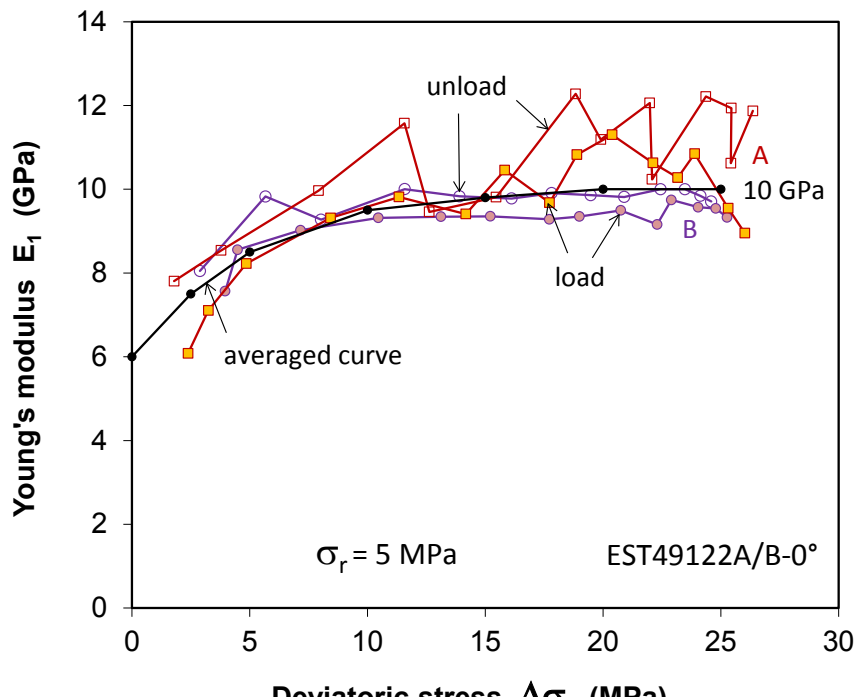


Fig. 3.14 Variation of Young's moduli E_1 and E_2 with deviatoric stress before failure

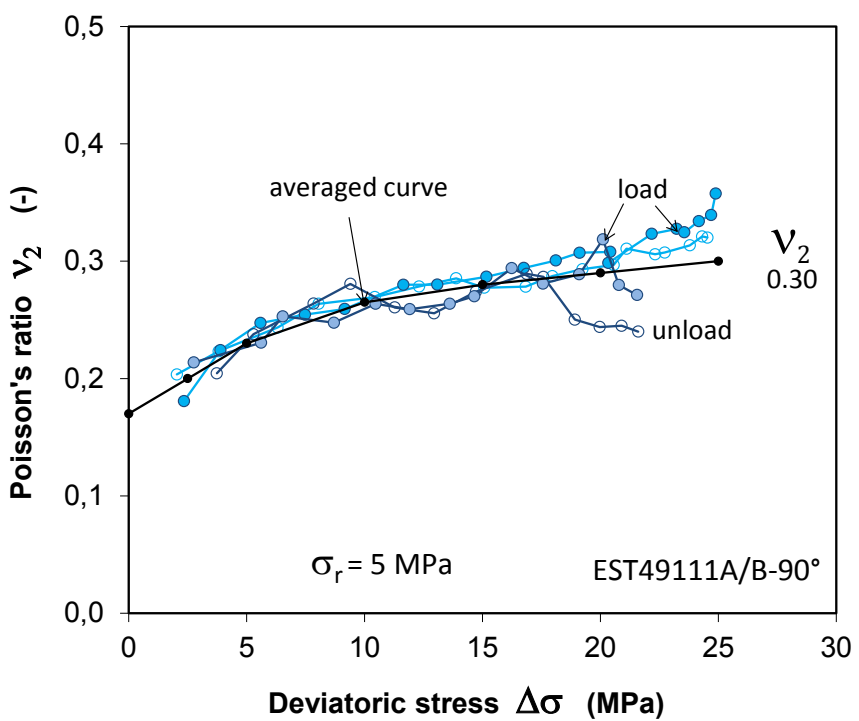
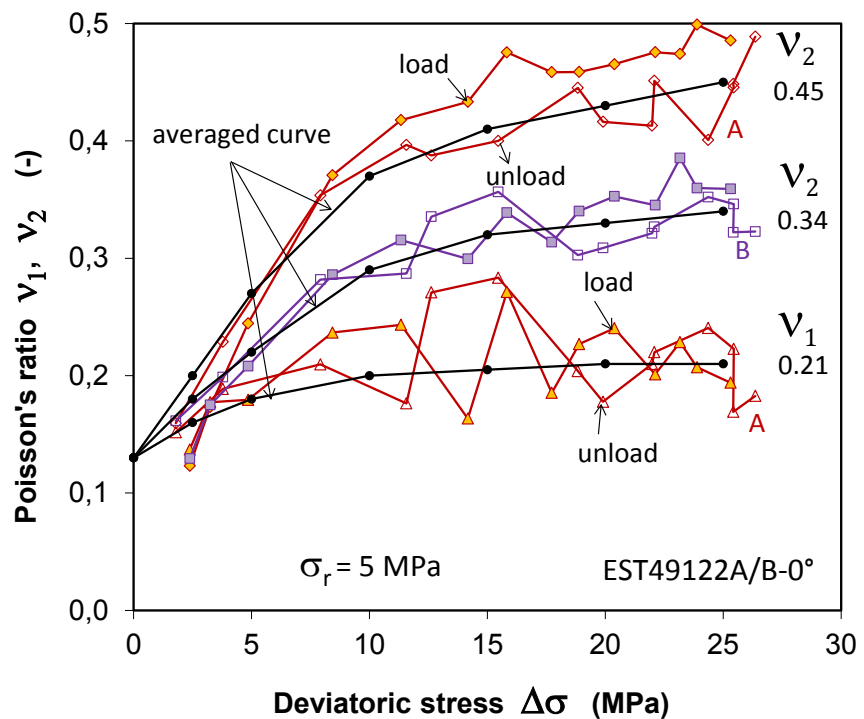


Fig. 3.15 Variation of Poisson's ratios v_1 and v_2 with deviatoric stress before failure

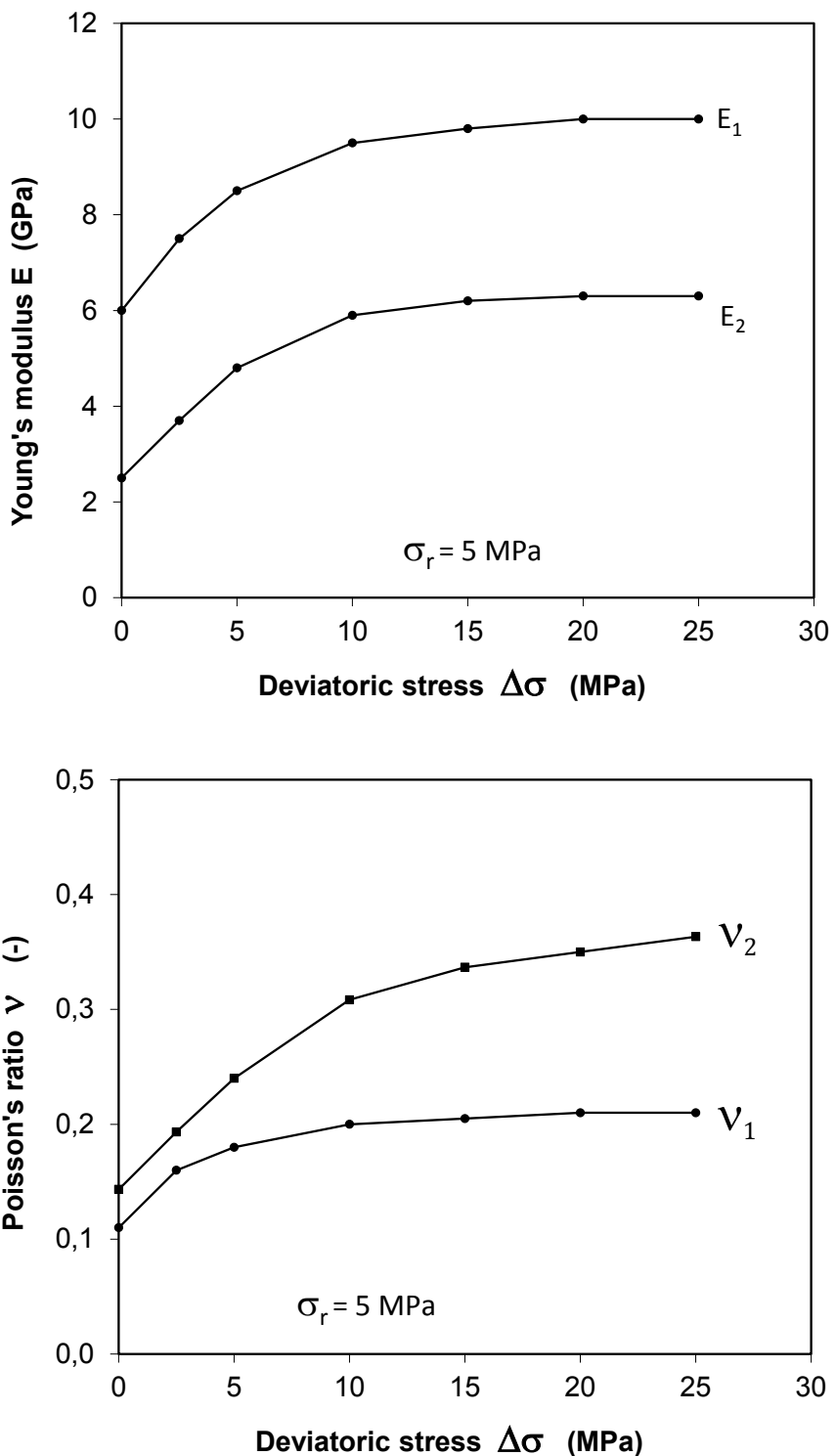


Fig. 3.16 Average Young's moduli E_1 and E_2 and Poisson's ratios ν_1 and ν_2 as a function of deviatoric stress

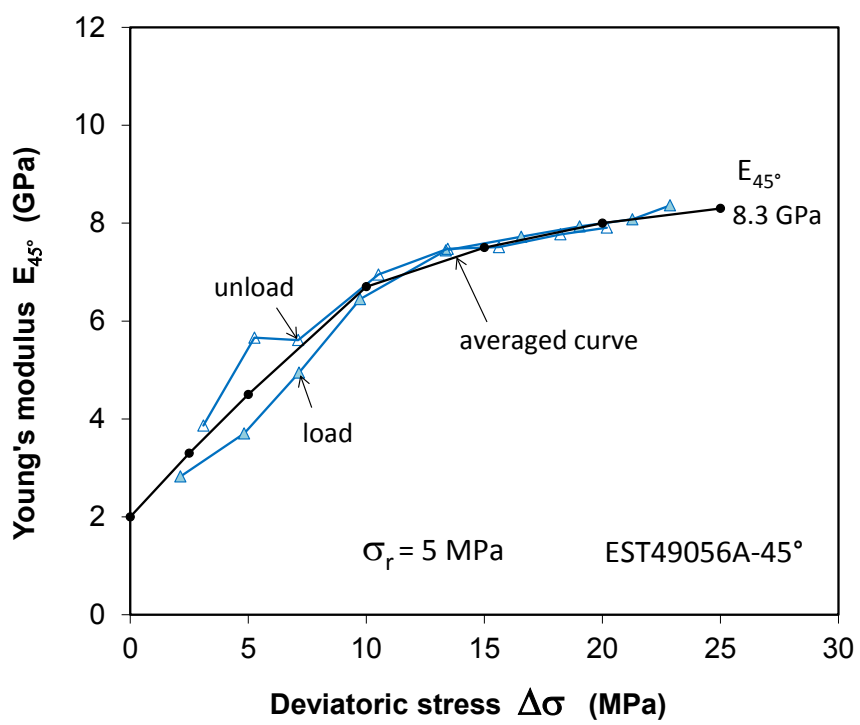
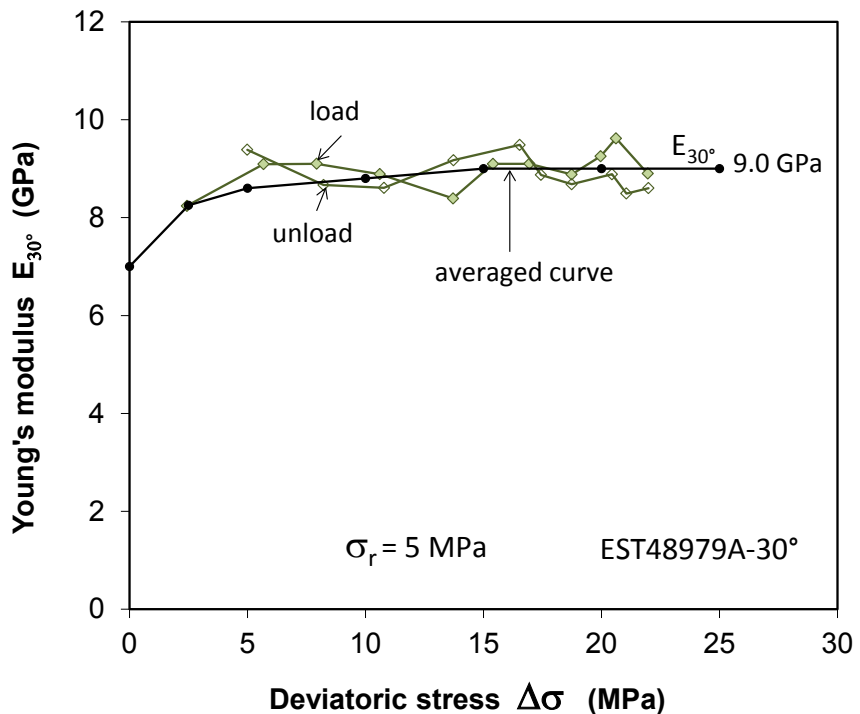


Fig. 3.17 Variation of Young's modulus E_α with deviatoric loading in $\alpha = 30^\circ$ and 45°

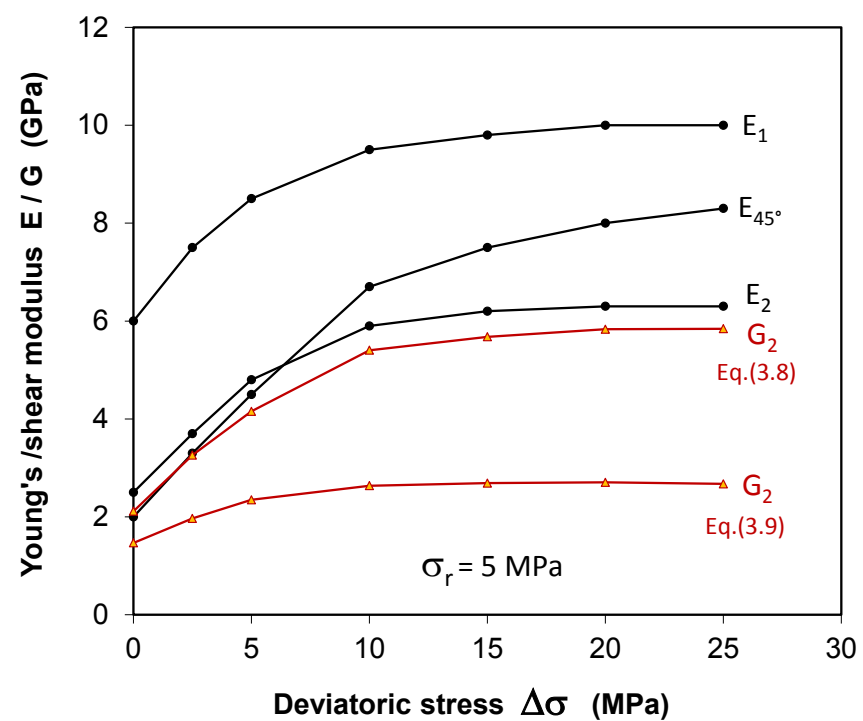
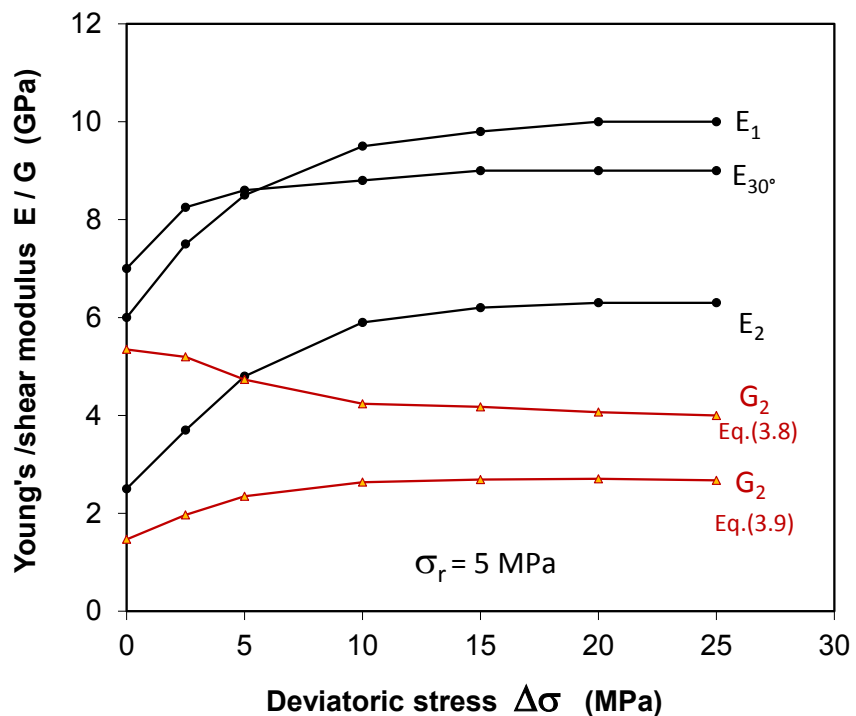


Fig. 3.18 Shear modulus G_2 based on the axial Young's modulus E_{30° and E_{45°

The degree of the elastic anisotropy may be characterised by the following two parameters

$$R_E = \frac{E_1}{E_2} \quad (3.10)$$

$$R_v = \frac{\nu_2}{\nu_1} \quad (3.11)$$

Based on the averaged values of E_1 / E_2 and ν_2 / ν_1 depicted in Fig. 3.16, the parameters of the elastic anisotropy are determined and illustrated in Fig. 3.19 as a function of deviatoric stress. Both parameters show different variations with the stress. Whereas R_E decreases due to the relatively fast increase in Young's modulus E_2 normal to bedding, in contrast R_v increases due to the relatively fast increase in Poisson's ratio ν_2 normal to bedding. Both parameters tend towards constant values close to each other, $R_E = 1.6$ and $R_v = 1.7$ for the range of $\Delta\sigma = 10$ to 25 MPa. It indicates that the elastic anisotropy of the claystone tends to be stabilized in the relatively high stress region above 10 MPa.

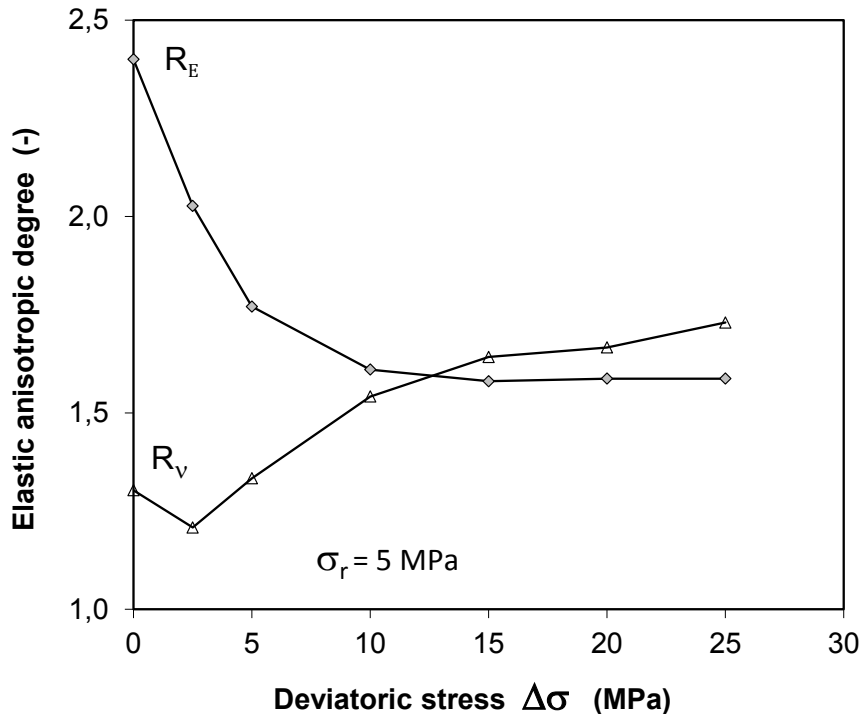


Fig. 3.19 Variation of the elastic anisotropy parameters as a function of deviatoric stress

The average values of the five independent elastic parameters obtained according to (Eq. 3.8) and the elastic anisotropic degrees are summarized in Tab. 3.1 for the COX clay rock at different deviatoric stresses. The relatively constant values of the parameters in the range of $\Delta\sigma = 10$ to 25 MPa are representative for the intact rock mass. The data can be used for comparison of the elastic anisotropy of the COX clay rock with others such as the Opalinus clay and Tournemire shale. Based on the data from literature, the elastic parameters of the Opalinus clay rock at Mont Terri /BOC 10/ and the Tournemire shale /NIA 97/ are represented in Tab. 3.1. The parameters of the Opalinus clay were given as constant while they were determined for the Tournemire shale at different stress conditions. For the comparison purpose, the parameters of the Tournemire shale are taken for the radial confining stress of 5 MPa. From Tab. 3.1 one can identify that the elastic stiffness of the COX clay rock is higher than that of the Opalinus clay but lower than the Tournemire shale. The elastic anisotropy of the COX clay rock is less significant compared with the other two clay rocks.

Tab. 3.1 Average values of the five independent elastic parameters and the anisotropic parameters of the COX clay rock at different deviatoric stresses

$\Delta\sigma$ (MPa)	E ₁ (GPa)	E ₂ (GPa)	G ₂ (GPa)	v ₁	v ₂	R _E =E ₁ /E ₂	R _v =v ₂ /v ₁
0	6.0	2.5	3.73	0.11	0.14	2.4	1.3
2.5	7.5	3.7	4.23	0.16	0.19	2.0	1.2
5	8.5	4.8	4.44	0.18	0.24	1.8	1.3
10	9.5	5.9	4.82	0.20	0.31	1.6	1.5
15	9.8	6.2	4.93	0.21	0.34	1.6	1.6
20	10.0	6.3	4.95	0.21	0.35	1.6	1.7
25	10.0	6.3	4.95	0.21	0.36	1.6	1.7

Elastic parameters of the Opalinus clay at Mont-Terri /BOC 10/

assumed	E ₁ (GPa)	E ₂ (GPa)	G ₂ (GPa)	v ₁	v ₂	R _E =E ₁ /E ₂	R _v =v ₂ /v ₁
constant	10.0	4.0	3.5	0.25	0.35	2.5	1.4

Elastic parameters of the Tournemire shale at confining stress = 5 MPa /NIA 97/

assumed	E ₁ (GPa)	E ₂ (GPa)	G ₂ (GPa)	v ₁	v ₂	R _E =E ₁ /E ₂	R _v =v ₂ /v ₁
constant	30.0	10.0	5.0	0.15	0.30	3.0	2.0

3.4.2 Failure strength and mode

Like most of transversely isotropic rocks, the failure strength and mode of the COX clay rock are closely related to the bedding structure, the orientation of the major principal stress, and the loading type such as triaxial compression and extension. Fig. 3.20 summarizes the peak strengths ($\sigma_F = |\sigma_a - \sigma_r|$) and the axial failure strains (ε_{a-f}) reached during the TCD and TCS triaxial compression and the TES and TEM triaxial extension as a function of the orientation of the major principal stress σ_1 inclined to the bedding planes. The orientation of the major principal stress is defined here as the angle θ of σ_1 to bedding: $\sigma_1 = \sigma_a$ and $\theta = \alpha$ for the TCD and TCS tests; $\sigma_1 = \sigma_r$ and $\theta = (90^\circ - \alpha)$ for the TES and TEM tests. The following points can be generally concluded:

- In a given orientation of θ , the peak strengths developed during TCD and TCS compression are higher than those reached during TES and TEM extension; in more detail, the TCD strain-controlled compressive strength is higher than the TCS stress-controlled strength, while the TEM extensive strength reached by simultaneously lateral compression and axial extension is lower than the TES extensive strength by lateral compression at constant axial stress.
- For each loading type (TCD, TCS, TES, TEM), the maximum strength values are reached at $\theta = 0^\circ$ and $\theta = 90^\circ$, and both are comparable; the minimum strength occurs at $\theta \approx 45^\circ$ by TCD and TCS compression and at $\theta \approx 30^\circ$ by TES and TEM extension respectively.
- The axial failure strains show a similar behaviour as the strength. The compressive failure strains occurred during TCD and TCS loading are comparable and higher than the tensile failure strains reached during TES and TEM loading. The maximum TCD and TCS compressive failure strains are reached at $\theta = 90^\circ$ and $\theta = 0^\circ$ and the minimum occurs at $\theta = 30-45^\circ$, while the TES and TEM extension failure strains are relatively constant for the different load orientations.

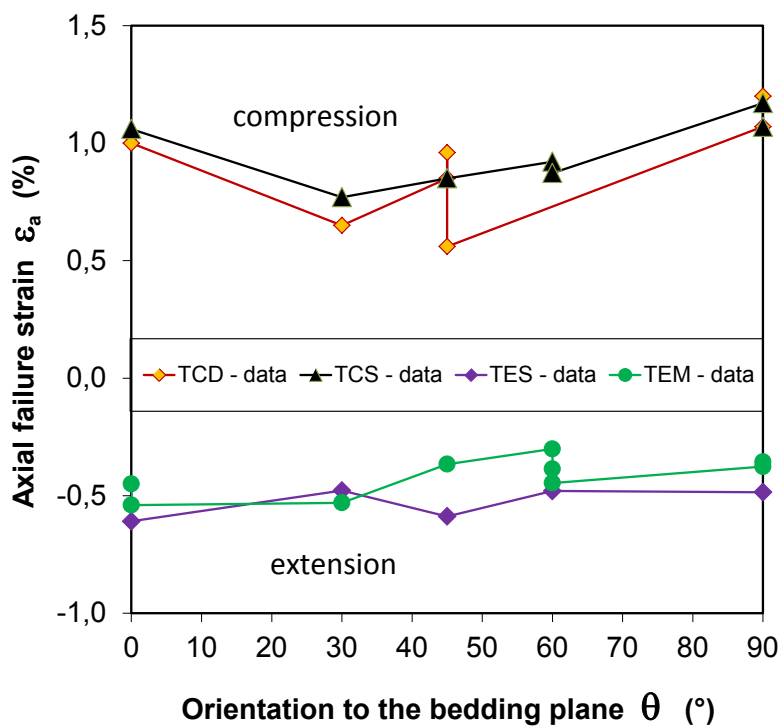
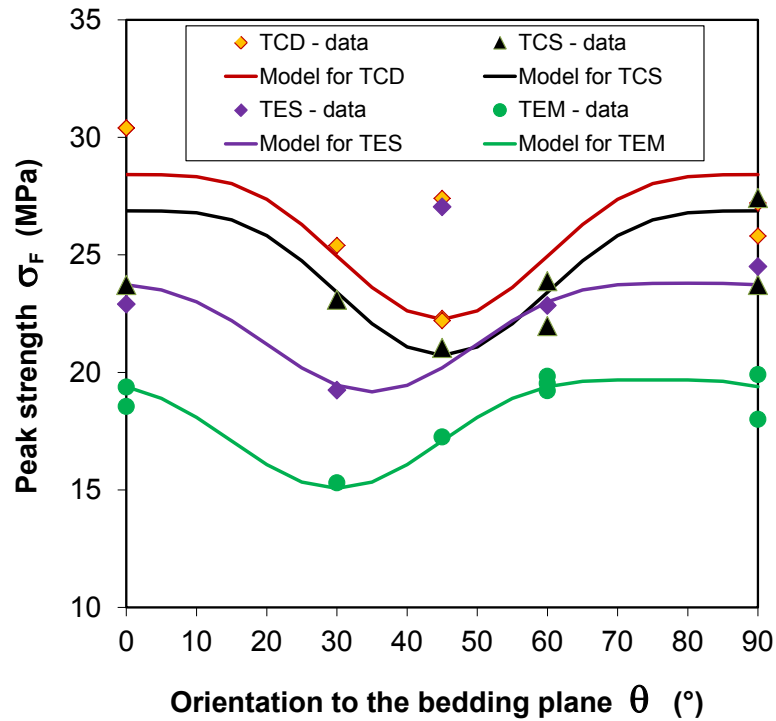


Fig. 3.20 Peak failure strength and axial failure strain developed along different loading paths as function of the orientation of the major principal stress with respect to bedding planes

After testing, failure modes of the failed samples were visually inspected. Fig. 3.21 shows pictures of some failed samples during TCD triaxial compression, TES and TEM triaxial extension. The failure modes observed after the TCD triaxial compression are quite similarly to those observed on the Tournemire shale in /NIA 97/ and the other rocks with a strong planar anisotropy /GAT 02/, /VAL 04/, /NAU 07/, /POP 07/, /GHO 14/. For $\alpha = 0^\circ$, the failure is dominated by extension of the bedding planes and thus the fractures are mainly oriented parallel and subparallel to the bedding planes, i.e. the fracture angle β is close to the bedding angle α ($\beta \approx \alpha$). For $30^\circ < \alpha < 45^\circ$, the failure is mainly controlled by sliding along the bedding planes and thus the fracture orientation is also close to the bedding angle ($\beta \approx \alpha$). For $60^\circ < \alpha < 90^\circ$, the failure is caused by shearing the claystone matrix and the fractures are crossing the bedding planes in angle of $\alpha - \beta \approx 30^\circ$. In the TES and TEM triaxial extension tests, most of the induced fractures are relatively parallel or subparallel to the major principal stress in radial direction. For $\alpha = 0^\circ$ the main fractures are normally crossing the bedding planes; for $30^\circ < \alpha < 60^\circ$ some fractures are also developing along the bedding planes; and for $\alpha = 90^\circ$ tensile splitting takes place between the bedding planes. Obviously, failure of the clay rock occurs not only along the bedding planes but also in the matrix, which depends on the orientation of the major principal stress to the bedding planes.

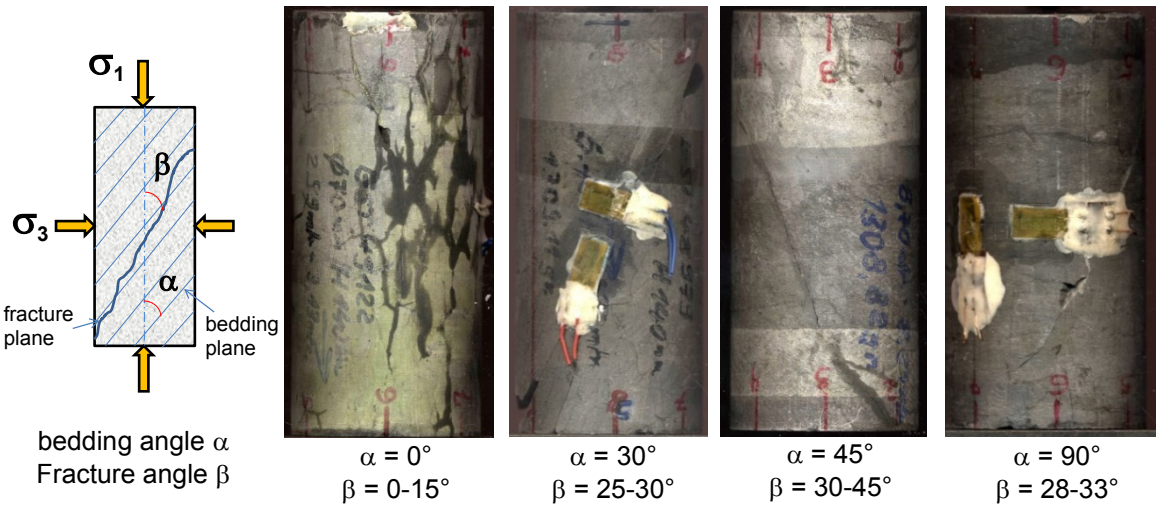
Jaeger (1960) introduced an instructive analysis of anisotropic rock containing a set of parallel weakness planes and proposed a criterion for failure along the weakness planes based on the Coulomb's criterion /JAE 60/, /BRA 06/. Considering the failure modes observed in most of the anisotropic rocks, the Jaeger criterion was improved by McLamore and Gray /MCL 67/ by introducing continuously variable cohesion and friction angle. Yuan et al /YUA 13/ successfully applied this improved model with variable cohesion but constant friction angle for the analysis of borehole stability in a shale:

$$\sigma_F = (\sigma_1 - \sigma_3)_F = \frac{2(c_o + \sigma_3 \tan \varphi)}{\sqrt{\tan^2 \varphi + 1} - \tan \varphi} \quad (3.12a)$$

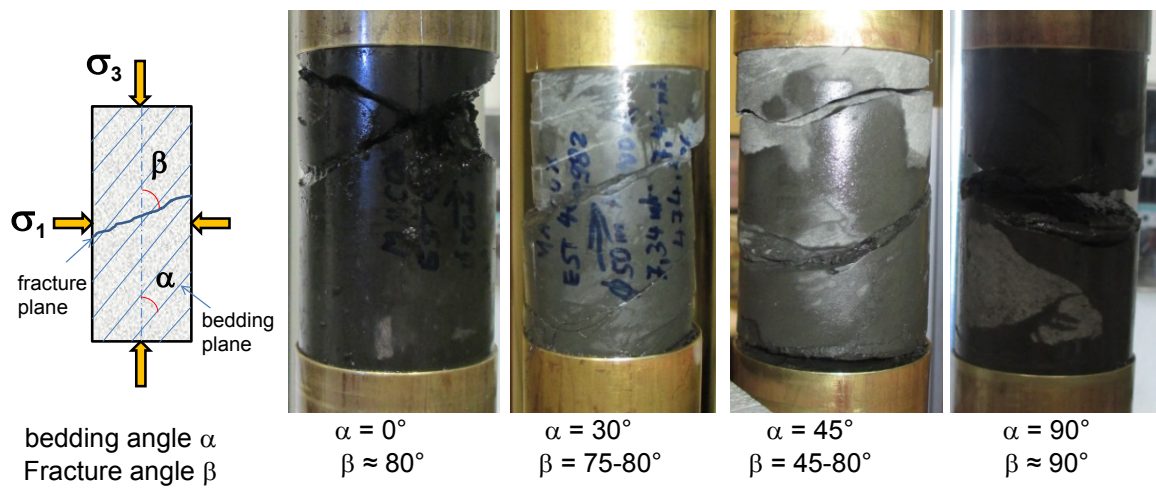
$$c_o = A - B[\cos 2(\theta - \theta_{co})]^n, \quad 0^\circ < \theta < \theta_{co} \quad (3.12b)$$

$$c_o = C - D[\cos 2(\theta - \theta_{co})]^m, \quad \theta_{co} < \theta < 90^\circ \quad (3.12c)$$

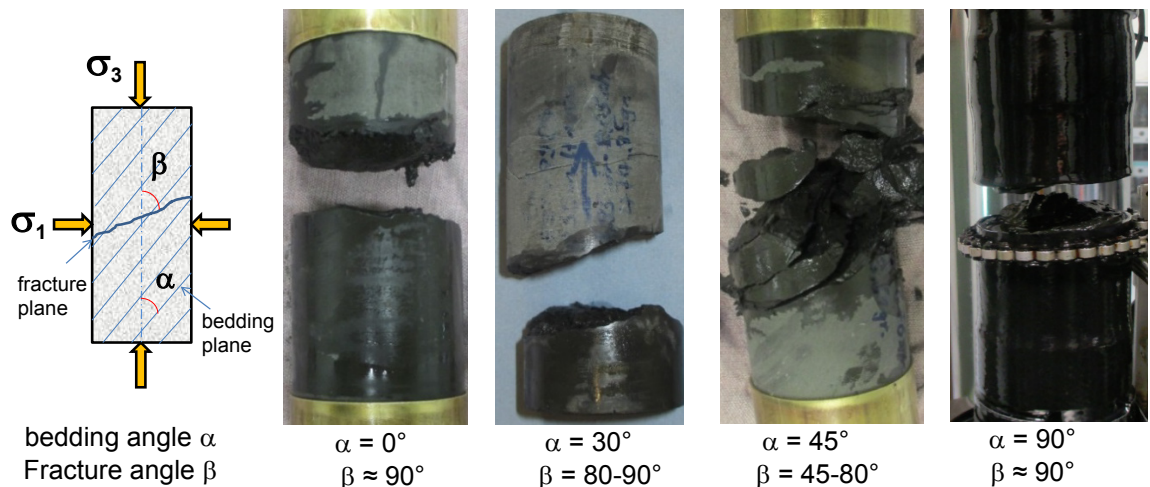
where σ_1 and σ_3 are the major and minor principal stress respectively, φ is the inner friction angle, c_o is the inherent cohesion depending on the angle θ of the major principal stress σ_1 direction to the bedding planes, and θ_{co} is the value of θ at which c_o takes minimum value.



TCD axial compression at $\sigma_3 = \sigma_r = 5$ MPa



TES lateral compression at $\sigma_3 = \sigma_a = 5$ MPa



TEM lateral compression and axial tension at $\sigma_m = (\sigma_3 + 2\sigma_1)/3 = 13.7$ MPa

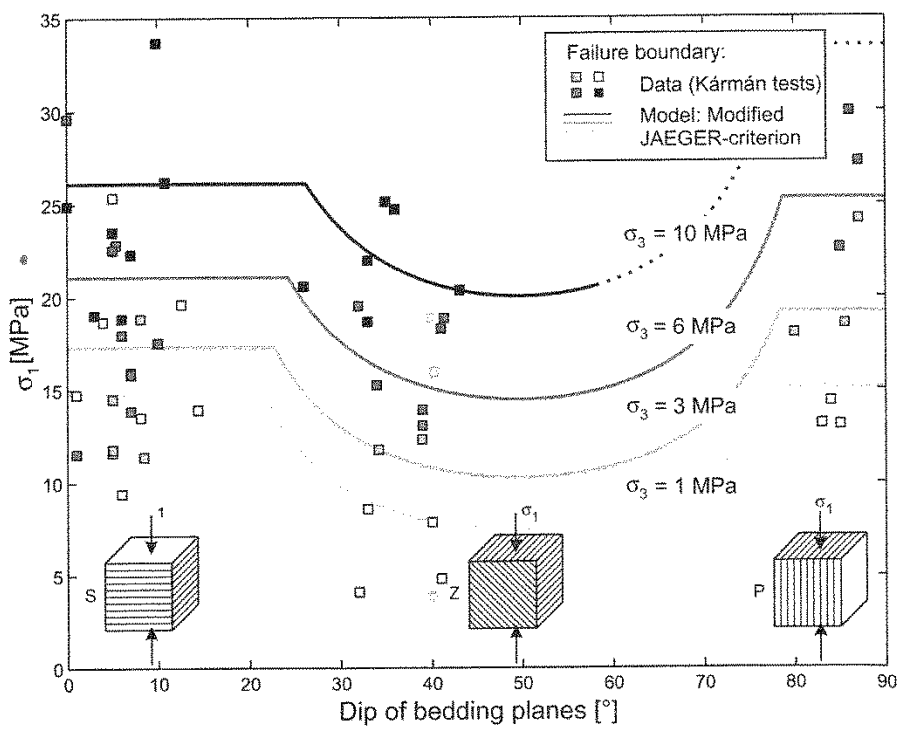
Fig. 3.21 Pictures of failed samples with induced fractures after various kinds of triaxial loading

Because the maximum strengths of the clay rock developed in the load orientations parallel and perpendicular to bedding are comparable, only one equation among (3.12b) and (3.12c) is required for fitting the data over the entire range of $0^\circ \leq \alpha \leq 90^\circ$. Based on the previous tests /ZHA 13/14/, the friction angle of $\varphi = 24^\circ$ determined in $\alpha = 0^\circ$ is adopted here. The other parameters are determined for each kind of test (TCD, TCS, TES and TEM) by fitting the strength data respectively. Whereas $\sigma_3 = 5$ MPa is known for the TCD, TCS and TES tests, it varies in a range of 1 to 3 MPa during the TEM tests at constant mean stress $\sigma_m = 13.7$ MPa. A mean value $\sigma_3 = 2$ MPa is taken for fitting the TEM strength data. All the parameters for each type of test are summarized in Tab. 3.2. Most of the parameters are equal or close for all test types. Fig. 3.20 compares the empirical criterion with the strength data. A reasonable agreement between them for all kinds of the tests can be identified.

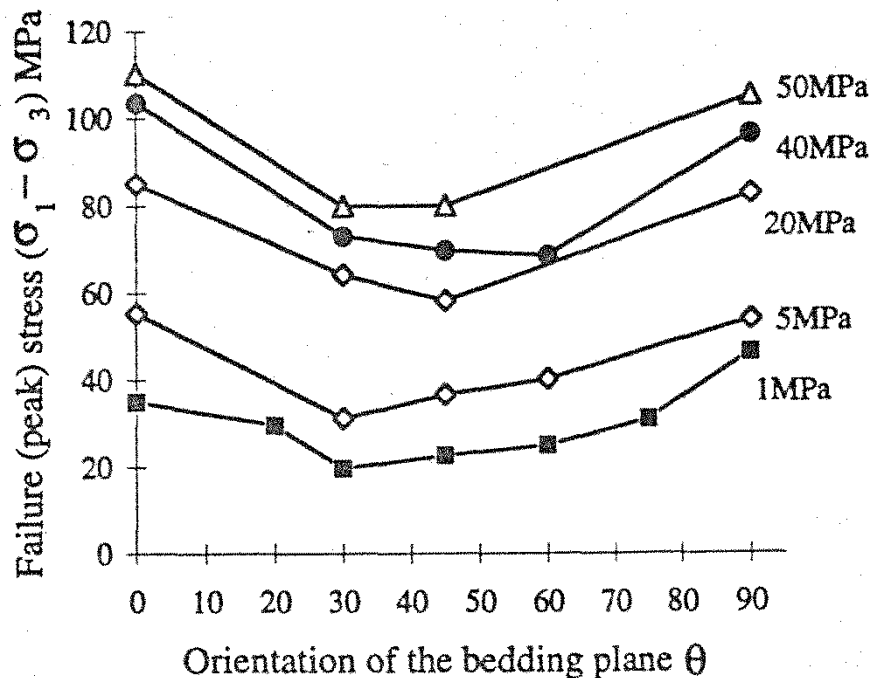
Tab. 3.2 Strength parameters for the various kinds of load conditions

Test type	$\sigma_3 \equiv$	$\sigma_1 \equiv$	$\varphi (\circ)$	$\alpha_{co} (\circ)$	A (MPa)	B (MPa)	n (-)
TCD	$\sigma_r = 5$ MPa	σ_a	24	45	7.0	2.0	4
TCS	$\sigma_r = 5$ MPa	σ_a	24	45	6.5	2.0	4
TES	$\sigma_a = 5$ MPa	σ_r	24	35	5.5	1.5	4
TEM	$\sigma_a \approx 2$ MPa	σ_r	24	30	5.5	1.5	4

The similar dependency of the strength on the load orientation was also observed for the Opalinus clay /NAU 07/ and the Tournemire shale /NIA 97/. The strength data obtained at various confining stresses are represented in Fig. 3.22. Note that the dip of bedding plane for the Opalinus clay is equal to $90^\circ - \theta$. The peak strengths of both clay rocks increase with increasing confining stress. For the same confining stress of $\sigma_3 = 5$ MPa, the compressive strength of the COX clay rock is higher than that of the Opalinus clay but lower than the Tournemire shale.



Opalinus clay /NAU 07/



Tournemire shale /NIA 97/

Fig. 3.22 Peak strengths of the Opalinus clay and Tournemire shale as function of the confining stress and the orientation of the major principal stress with respect to bedding planes

4 Conclusions

The anisotropic mechanical behaviour of the COX clay rock has been investigated with various kinds of triaxial compression and extension tests on the cores drilled in different directions with respect to the bedding planes. In order to enhance their quality and thus the transferability of the test data to the natural clay rock, the samples were hydrostatically pre-compacted before testing. The following conclusions can be drawn from the test results:

- The degree of structural anisotropy of the clay rock is about 2, determined during hydrostatic loading-unloading and characterized by the ratio of the elastic deformability in normal to parallel direction to the bedding.
- The clay rock exhibits the elasto-plastic behaviour during short-term deviatoric compression and extension, characterised by non-linearity of the stress-strain relation, hysteresis in loading-unloading, irreversibility of strains after unloading, and volume compaction until the peak failure stress.
- The deformation is influenced by the bedding planes and depends on the orientation of the major principal stress to the bedding. When the load is parallel and sub-parallel to bedding, the opening of the bedding planes is the dominating damage mechanism; when the load is normal and subnormal to bedding, the bedding planes are going to close up; and in between, sliding along the bedding planes plays an important role.
- The Young's moduli and Poisson's ratios determined in the applied load orientations increase in the beginning of deviatoric loading due to hardening effect and then tend to constant before peak failure. Five independent elastic parameters are obtained for the clay rock.
- The short-term strength is dependent on loading path and direction with respect to the bedding. For a given major load direction, the compressive strength is higher than the extensive one and the lowest strength occurs by triaxial extension at constant mean stress. In each loading path, the maximum strength values are reached in parallel and normal to bedding, while the minimum occurs at the load orientation of $\sim 45^\circ$ during compression and of $\sim 30^\circ$ during extension. The dependence of the strength on the major load orientation can be described by an empirical model for each kind of the tests.
- Significant time effects on the deformation and strength are observed during the long-term creep tests. The long-term deformation rate seems to be less dependent on load orientation, i.e., insignificant anisotropy of the long-term behaviour.

It has to be pointed out that more precise experiments on the clay rock are needed to enhance the certainty of the test results and conclusions, particularly with regard to the effect of confining stress on the mechanical behaviour and anisotropy, the long-term deformation and damage.

References

- /AND 05/ ANDRA DOSSIER (2005): Synthesis – Evaluation of the feasibility of a geological repository in an argillaceous formation
- /BRA 06/ Brady, B.H.G. and Brown, E.T. (2006): Rock Mechanics for Underground Mining, third edition, Springer
- /BOC 10/ Bock, H., Dehandschutter, B., Martin, C.D., Mazurek, M., Haller, A.D., Skoczylas, F., Davy, C. (2010): Self-Sealing of Fractures in Argillaceous Formations in the Context of Geological Disposal of Radioactive Waste – Review and Synthesis, OECD 2010, NEA No. 6184
- /GAT 02/ Gatelier, N., Pellet, F., Loret, B. (2002): Mechanical damage of an anisotropic porous rock in cyclic triaxial tests, Int. J. Rock Mech. Min. Sci. Vol 39 335-354
- /GHO 14/ Gholami, R., Rasouli, V. (2014): Mechanical Elastic Properties of Transversely Isotropic Slate, Rock Mech Rock Eng 47: 1763-1773
- /ISR 81/ ISRM: Rock Characterization Testing & Monitoring – IRSM suggested methods, 1981
- /JAE 60/ Jaeger, J. C. (1960): Shear fracture of anisotropic rocks, Geol. Mag. 97: 65-72
- /MCL 67/ McLamore, R. and Gray, K.E. (1967): The mechanical behaviour of anisotropic sedimentary rocks, J. Energy for Industry, Trans. Am. Soc. Mech. Engers Ser. B, 89: 62-73
- /NAU 07/ Naumann, M., Hunsche, U., Schulze, O. (2007): Experimental investigations on anisotropy in dilatancy, failure and creep of Opalinus Clay, Phys. Chem. Earth Parts 32, 889–895
- /NIA 97/ Niandou, H., Shao, J.F., Henry, J.P., Fourmaintraux, D. (1997): Laboratory Investigation of the Mechanical Behaviour of Tournemire Shale, Int. J. Rock Mech. Min. Sci. Vol 34, No. 1, pp. 3-16

- /POP 07/ Popp, T., Salzer, K. (2007): Anisotropy of seismic and mechanical properties of Opalinus clay during triaxial deformation in a multi-anvil apparatus, Phys. Chem. Earth Parts 32, 879–888
- /SAR 07/ Sarout, J., Molez, L., Gueguen, Y., Hoteit, N. (2007): Shale dynamic properties and anisotropy under triaxial loading: Experimental and theoretical investigations, Phys. Chem. Earth Parts 32, 896-906
- /VAL 04/ Vales, F., Nguyen Minh, D., Gharbi, H., Rejeb, A. (2004): Experimental study of the influence of the degree of saturation on physical and mechanical properties in Tornemire shale (France), Appl. Clay Sci. 26, 197-207
- /VAL 12/ Valente, S., Fidelibus, C., Loew, S., Cravero, M., Iabichino, G., Barpi, F. (2012): Analysis of Fracture Mechanics Tests on Opalinus Clay, Rock Mech Rock Eng 45:767-779
- /WIT 84/ Wittke, W. (1984): Felsmechanik – Grundlagen für wirtschaftliches Bauern im Fels, Springer-Verlag
- /YAN 13/ Yang, D., Chanchole, S., Valli, P., Chen, L. (2013): Study of the Anisotropic properties of argillite under moisture and mechanical loads, Rock Mech Rock Eng (2013), 46: 247-257
- /YOU 13/ Yuan, J.L., Deng, J.G., Tan, Q., Yu, B.H., Jin, X.C. (2013): Borehole stability analysis of horizontal drilling in shale gas reservoirs, Rock Mech Rock Eng (2013), 46: 1157-1164
- /ZHA 10/ Zhang, C.L., Czaikowski, O., Rothfuchs, T. (2010): Thermo-Hydro-Mechanical Behaviour of the Callovo-Oxfordian Clay Rock, Final report of the BURE-HAUP/EC-TIMODAZ project, GRS-266
- /ZHA 13/ Zhang C.L., Czaikowski O., Rothfuchs T., Wieczorek K. (2013): Thermo-Hydro-Mechanical Processes in the Nearfield around a HLW Repository in Argillaceous Formations, Project Report THM-TON, GRS-312
- /ZHA 14/ Zhang C.L. (2014): Deliverables D3.28 and D5.5 of the EC project DOPAS: Status report on characterization and modelling of clay rock and claystone-based seal material

List of tables

Tab. 3.1	Average values of the five independent elastic parameters and the anisotropic parameters of the COX clay rock at different deviatoric stresses	45
Tab. 3.2	Strength parameters for the various kinds of load conditions	50

List of figures

Fig. 2.1	Position of the coring drift NER at the -490m main level of the MHM-URL	3
Fig. 2.2	Arrangement of the boreholes and sampling positions.....	4
Fig. 2.3	Pictures of typical samples with bedding planes inclined to the sample axis at angles of $\alpha \approx 0^\circ, 30^\circ, 45^\circ, 60^\circ$ and 90°	5
Fig. 2.4	Distributions of the main mineralogical components (clay, carbonate, quartz etc.) in the sampling region	6
Fig. 2.5	Distributions of the physical properties in the sampling region	9
Fig. 3.1	Schematic of designed loading paths.....	14
Fig. 3.2	Orientations of local strain measurements with respect to bedding planes.....	15
Fig. 3.3	Test set up for triaxial compression and extension testing	16
Fig. 3.4	Coupled rig for triaxial creep testing on two samples one upon another	17
Fig. 3.5	Strains measured in orientations normal, parallel and inclined to bedding planes ($\varepsilon_{\perp}, \varepsilon_{\parallel}, \varepsilon_{a\alpha}$) during hydrostatic loading-unloading cycle	19
Fig. 3.6	Elastic strains measured in orientations normal, parallel and inclined to bedding planes ($\varepsilon_{\perp}, \varepsilon_{\parallel}, \varepsilon_{a\alpha}$) during hydrostatic unloading.....	22
Fig. 3.7	Stress-strain curves obtained in directions normal, parallel and inclined to bedding planes ($\Delta\sigma-\varepsilon_{\perp}, \Delta\sigma-\varepsilon_{\parallel}, \Delta\sigma-\varepsilon_{a\alpha}$) during strain-controlled axial compression oriented at angles of $\alpha = 0^\circ, 30^\circ, 45^\circ$ and 90° to bedding and at lateral stress of 5 MPa.....	25
Fig. 3.8	Development of axial / radial / volumetric strains during strain-controlled axial compression oriented at angles of $\alpha = 0^\circ, 30^\circ, 45^\circ$ and 90° inclined to bedding and at lateral stress of 5 MPa.....	27

Fig. 3.9	Stress-strain curves obtained during stress-controlled axial compression oriented at angles of $\alpha = 0^\circ, 30^\circ, 45^\circ, 60^\circ$ and 90° inclined to bedding and at lateral stress $\sigma_r = 5$ MPa	29
Fig. 3.10	Stress-strain curves obtained during lateral compression at constant axial stress $\sigma_a = 5$ MPa for the axial load angles of $\alpha = 0^\circ, 30^\circ, 45^\circ, 60^\circ$ and 90° inclined to bedding	31
Fig. 3.11	Stress-strain curves obtained during lateral compression and axial extension at constant mean stress $\sigma_m = 13.7$ MPa for the axial load angles of $\alpha = 0^\circ, 30^\circ, 45^\circ, 60^\circ$ and 90° inclined to bedding	32
Fig. 3.12	Evolution of axial strain and strain rate during the triaxial creep tests under multistep stresses of $\sigma_r = 5$ MPa and $\sigma_a = 20 / 22$ MPa and at axial load angles of $\alpha = 0^\circ, 30^\circ, 45^\circ, 60^\circ$ and 90° inclined to bedding	33
Fig. 3.13	Definition of the elastic parameters for a transversely isotropic rock with bedding planes (after /WIT 84/)	36
Fig. 3.14	Variation of Young's moduli E_1 and E_2 with deviatoric stress before failure.....	39
Fig. 3.15	Variation of Poisson's ratios ν_1 and ν_2 with deviatoric stress before failure.....	40
Fig. 3.16	Average Young's moduli E_1 and E_2 and Poisson's ratios ν_1 and ν_2 as a function of deviatoric stress.....	41
Fig. 3.17	Variation of Young's modulus E_α with deviatoric loading in $\alpha = 30^\circ$ and 45°	42
Fig. 3.18	Shear modulus G_2 based on the axial Young's modulus E_{30° and E_{45°	43
Fig. 3.19	Variation of the elastic anisotropy parameters as a function of deviatoric stress.....	44
Fig. 3.20	Peak failure strength and axial failure strain developed along different loading paths as function of the orientation of the major principal stress with respect to bedding planes	47
Fig. 3.21	Pictures of failed samples with induced fractures after various kinds of triaxial loading.....	49

Fig. 3.22	Peak strengths of the Opalinus clay and Tournemire shale as function of the confining stress and the orientation of the major principal stress with respect to bedding planes	51
Fig. A.1	A core unpacked from T-cell	65
Fig. A.2	A core unpacked from aluminium foil	65
Fig. A.3	A damaged core unpacked from aluminium foil	65
Fig. A.4	Organic component in cores (I).....	66
Fig. A.5	Organic component in cores (II).....	66
Fig. A.6	Sample preparation	66
Fig. E.1	Sample EST49122A in axial load orientation $\alpha = 0^\circ$ with respect to bedding.....	77
Fig. E.2	Stress-strain curves during hydrostatic pre-compaction and deviatoric loading.....	77
Fig. E.3	Elastic parameters as a function of applied deviatoric stress	78
Fig. E.4	Sample EST49122B in axial load orientation $\alpha = 0^\circ$ with respect to bedding.....	78
Fig. E.5	Stress-strain curves during hydrostatic pre-compaction and deviatoric loading.....	79
Fig. E.6	Elastic parameters as a function of applied deviatoric stress	79
Fig. E.7	Sample EST48979A in axial load orientation $\alpha = 30^\circ$ with respect to bedding.....	80
Fig. E.8	Stress-strain curves during hydrostatic pre-compaction and deviatoric loading.....	80
Fig. E.9	Elastic parameters as a function of applied deviatoric stress	81
Fig. E.10	Sample EST49056A in axial load orientation $\alpha = 45^\circ$ with respect to bedding.....	82

Fig. E.11	Stress-strain curves during hydrostatic pre-compaction and deviatoric loading.....	82
Fig. E.12	Elastic parameters as a function of applied deviatoric stress	83
Fig. E.13	Sample EST49056B in axial load orientation $\alpha = 45^\circ$ with respect to bedding.....	83
Fig. E.14	Stress-strain curves during hydrostatic pre-compaction and deviatoric loading.....	84
Fig. E.15	Elastic parameters as a function of applied deviatoric stress	84
Fig. E.16	Sample EST49111A in axial load orientation $\alpha = 90^\circ$ with respect to bedding.....	85
Fig. E.17	Stress-strain curves during hydrostatic pre-compaction and deviatoric loading.....	85
Fig. E.18	Elastic parameters as a function of applied deviatoric stress	86
Fig. E.19	Sample EST49111B in axial load orientation $\alpha = 90^\circ$ with respect to bedding.....	86
Fig. E.20	Stress-strain curves during hydrostatic pre-compaction and deviatoric loading.....	87
Fig. E.21	Elastic parameters as a function of applied deviatoric stress	87
Fig. E.22	Stress-strain curves from TC hydrostatic and deviatoric compression	91
Fig. E.23	Parameters obtained from the TCS hydrostatic pre-compaction	91
Fig. E.24	Parameters obtained from the TCS triaxial deviatoric compression	92
Fig. E.25	Stress-strain curves from TES triaxial extension tests	96
Fig. E.26	Parameters obtained from the TES hydrostatic pre-compaction	97
Fig. E.27	Parameters obtained from the TES triaxial extension	97
Fig. E.28	Stress-strain curves from TEM triaxial extension tests	101
Fig. E.29	Parameters obtained from the TEM hydrostatic pre-compaction.....	102

Fig. E.30 Parameters obtained from the TEM triaxial extension 102

Fig. E.31 Creep curves obtained under constant triaxial stress conditions 105

A**Appendix: Drilled cores and sample preparation**

Fig. A.1 A core unpacked from T-cell



Fig. A.2 A core unpacked from aluminium foil



Fig. A.3 A damaged core unpacked from aluminium foil



Fig. A.4 Organic component in cores (I)

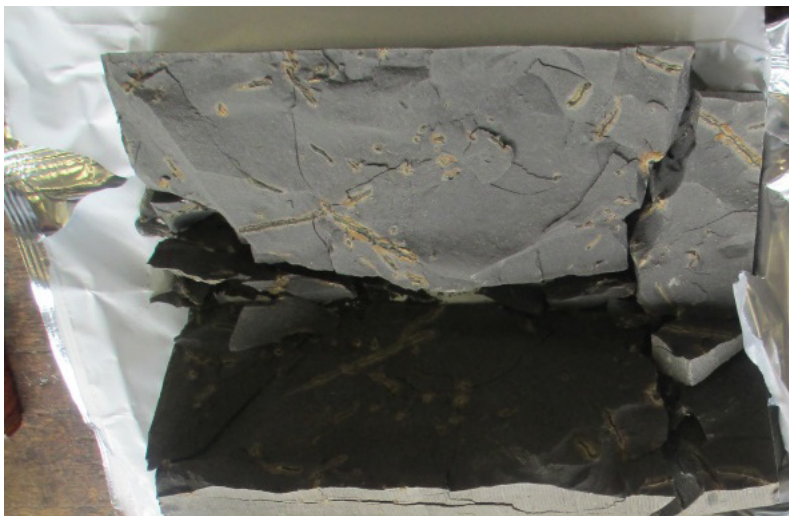


Fig. A.5 Organic component in cores (II)



Fig. A.6 Sample preparation

B Appendix: Mineral composition of drilled cores

Tab. B.1 Estimated mineralogical components of clay, carbonates and quartz

OHZ6560: $\alpha = 90^\circ$				
Core ID	Depth (m)	Clay (%)	Carbonates (%)	Quartz (%)
EST49073	5,01	27,44	38,28	34,28
EST49074	5,3	26,96	38,47	34,58
EST49014	5,32	36,97	33,66	29,38
EST49093	5,43	35,36	32,40	32,25
EST48974	5,5	42,01	31,28	26,70
EST49015	5,63	36,97	33,66	29,38

OHZ6561: $\alpha = 60^\circ$				
Core ID	Depth (m)	Clay (%)	Carbonates (%)	Quartz (%)
EST49075	5,605	28,50	37,41	34,08
EST49095	5,8	34,79	32,31	32,90
EST48975	5,81	42,24	30,92	26,84
EST49017	5,97	36,97	33,66	29,38
EST49051	6,04	30,17	36,90	32,93
EST49077	6,09	32,98	34,51	32,52
EST49097	6,19	32,32	33,13	34,55
EST48976	6,25	42,14	30,68	27,18
EST49052	6,355	28,61	37,69	33,69

OHZ6562: $\alpha = 45^\circ$				
Core ID	Depth (m)	Clay (%)	Carbonates (%)	Quartz (%)
EST49078	6,4	34,83	33,10	32,07
EST48978	6,45	41,86	30,76	27,38
EST49053	6,66	27,44	38,28	34,28
EST49079	6,71	35,36	32,40	32,25
EST48979	6,81	40,94	31,21	27,85
EST49055	6,99	26,96	38,47	34,58
EST49099	7	28,44	34,93	36,63
EST49081	7,1	34,79	32,31	32,90
EST48980	7,12	40,35	31,53	28,12

OHZ6563: $\alpha = 30^\circ$				
Core ID	Depth (m)	Clay (%)	Carbonates (%)	Quartz (%)
EST49019	7,12	36,97	33,66	29,38
EST49056	7,3	27,65	37,97	34,38
EST49101	7,33	28,43	34,96	36,60
EST48982	7,34	39,71	31,89	28,40
EST49082	7,41	33,95	32,53	33,52
EST49020	7,43	36,97	33,66	29,38
EST48983	7,65	38,32	32,67	29,01
EST49057	7,6	30,82	35,93	33,25
EST49103	7,66	30,15	34,13	35,72

OHZ6564: $\alpha = 0^\circ$				
Core ID	Depth (m)	Clay (%)	Carbonates (%)	Quartz (%)
EST49083	7,72	31,73	33,37	34,90
EST49021	7,74	36,97	33,66	29,38
EST48984	7,96	37,59	33,07	29,35
EST49105	8,5	37,75	29,97	32,28
EST49060	8,55	35,14	32,79	32,07
EST49106	8,8	39,40	29,13	31,47

OHZ6565: $\alpha = 0^\circ$				
Core ID	Depth (m)	Clay (%)	Carbonates (%)	Quartz (%)
EST49121	2,84	38,38	30,06	31,56
EST49122	3,14	38,38	30,06	31,56
EST49124	3,52	41,04	27,68	31,28
EST49061	8,85	35,36	32,40	32,25
EST49062	9,15	35,08	32,28	32,64
EST49108	9,22	41,87	28,66	29,47

C Appendix: Characteristics of tested samples

Tab. C.1 Basic properties measured on the samples before testing

Physical properties	Grain density	Dry density	Bulk density	Porosity	Water content	Water saturation
	(g/cm ³)	(g/cm ³)	(g/cm ³)	(%)	(%)	(%)
Mean value	2,695	2,25	2,42	16,5	7,1	96,0
Upper & lower limit	±0,020	±0,030	±0,030	±1,30	±0,40	±4,0

Borehole OHZ6560: α = 90°					Grain density	Dry density	Bulk density	Porosity	Water content	Water saturation
Core ID	confinement	top (m)	end (m)	depth (m)	(g/cm ³)	(g/cm ³)	(g/cm ³)	(%)	(%)	(%)
EST49093	CP13504	5,33	5,53	5,43						
EST49095	T12097	5,64	5,96	5,80	2,68	2,23	2,40	16,7	7,2	96,0
EST49097	CP13504	6,09	6,29	6,19	2,70	2,24	2,41	16,9	7,0	92,1
EST49099	CP13505	6,90	7,10	7,00	2,70	2,29	2,45	15,2	6,9	102,9
EST49101	T12098	7,17	7,49	7,33						
EST49103	CP13505	7,56	7,76	7,66	2,68	2,24	2,41	16,2	6,7	92,5
EST49105	CP13505	8,40	8,60	8,50	2,68	2,23	2,41	16,7	7,5	100,4
EST49106	T12099	8,65	8,95	8,80	2,68	2,23	2,41	16,4	7,3	98,0
EST49108	CP13505	9,12	9,32	9,22						
EST49111	T12101	9,80	10,10	9,95	2,69	2,40	2,23	17,0	7,2	94,0
EST49113	T12102	10,31	10,61	10,46						

Borehole OHZ6561: $\alpha = 60^\circ$					Grain density	Dry density	Bulk density	Porosity	Water content	Water saturation
Core ID	confinement	top (m)	end (m)	depth (m)	(g/cm ³)	(g/cm ³)	(g/cm ³)	(%)	(%)	(%)
EST49073	CP13500	4,91	5,11	5,01						
EST49074	T12094	5,15	5,45	5,30	2,69	2,22	2,40	17,4	7,5	95,9
EST49075	CP13500	5,50	5,71	5,61						
EST49077	CP13500	5,99	6,19	6,09	2,69	2,28	2,45	15,5	7,0	102,5
EST49078	T12095	6,24	6,56	6,40						
EST49079	CP13500	6,61	6,81	6,71	2,69	2,26	2,42	16,2	6,7	93,4
EST49081	CP13501	7,00	7,20	7,10	2,69	2,22	2,40	17,2	7,3	94,1
EST49082	T12096	7,25	7,57	7,41	2,68	2,22	2,40	16,9	7,3	96,5
EST49083	CP13501	7,26	7,82	7,54	2,69	2,22	2,40	17,2	7,3	94,4

Borehole OHZ6562: $\alpha = 45^\circ$					Grain density	Dry density	Bulk density	Porosity	Water content	Water saturation
Core ID	confinement	top (m)	end (m)	depth (m)	(g/cm ³)	(g/cm ³)	(g/cm ³)	(g/cm ³)	(%)	(%)
EST49051	CP13497	5,94	6,14	6,04						
EST49052	T12091	6,20	6,51	6,36						
EST49053	CP13497	6,56	6,76	6,66	2,68	2,24	2,42	16,5	7,3	98,8
EST49055	CP13497	6,89	7,09	6,99	2,70	2,24	2,42	17,1	7,4	96,4
EST49056	T12092	7,15	7,45	7,30	2,70	2,43	2,26	16,4	7,0	96,5
EST49057	CP13497	7,50	7,70	7,60	2,72	2,28	2,45	15,9	6,9	98,2
EST49060	CP13497	8,45	8,65	8,55	2,69	2,28	2,44	15,3	6,5	97,5
EST49061	T12093	8,70	9,00	8,85	2,69	2,25	2,43	16,4	7,3	100,2
EST49062	CP13497	9,05	9,25	9,15	2,69	2,23	2,41	17,2	7,5	97,2

Borehole OHZ6563: $\alpha = 30^\circ$					Grain density	Dry density	Bulk density	Porosity	Water content	Water saturation
Core ID	confinement	top (m)	end (m)	depth (m)	(g/cm ³)	(g/cm ³)	(g/cm ³)	(%)	(%)	(%)
EST48974	CP13481	5,40	5,60	5,50						
EST48975	T12086	5,65	5,97	5,81	2,69	2,26	2,42	15,9	6,6	93,4
EST48976	CP13481	6,15	6,35	6,25	2,69	2,26	2,43	15,9	7,0	99,8
EST48978	CP13481	6,35	6,55	6,45	2,70	2,25	2,43	16,9	7,5	99,5
EST48979	T12087	6,65	6,97	6,81	2,70	2,26	2,44	16,2	7,1	99,3
EST48980	CP13482	7,02	7,22	7,12	2,70	2,27	2,43	16,1	6,7	94,3
EST48982	CP13482	7,24	7,44	7,34	2,69	2,24	2,42	16,6	7,3	98,4
EST48983	T12088	7,49	7,81	7,65	2,70	2,23	2,41	17,7	7,2	93,8
EST48984	CP13482	7,86	8,06	7,96	2,70	2,23	2,42	17,3	7,7	99,8
Borehole OHZ6564: $\alpha = 0^\circ$					Grain density	Dry density	Bulk density	Porosity	Water content	Water saturation
Core ID	confinement	top (m)	end (m)	depth (m)	(g/cm ³)	(g/cm ³)	(g/cm ³)	(%)	(%)	(%)
EST49014	CP13489	5,22	5,42	5,32						
EST49015	T12089	5,47	5,79	5,63	2,68	2,24	2,40	16,3	6,6	90,6
EST49017	CP13489	5,87	6,07	5,97	2,69	2,22	2,41	17,4	7,5	96,2
EST49019	CP13490	7,02	7,22	7,12	2,69	2,25	2,42	16,5	7,2	97,7
EST49020	T12090	7,27	7,59	7,43	2,70	2,26	2,43	16,2	7,0	97,8
EST49021	CP13490	7,64	7,84	7,74	2,72	2,23	2,41	17,9	7,3	91,1
Borehole OHZ6565: $\alpha = 0^\circ$					Grain density	Dry density	Bulk density	Porosity	Water content	Water saturation
EST49121	CP13508	2,74	2,94	2,84						
EST49122	T12104	2,99	3,29	3,14	2,70	2,41	2,23	17,2	7,2	93,0
EST49124	CP13508	3,42	3,62	3,52	2,69	2,23	2,40	17,3	7,2	92,6

D Appendix: Test plan

Tab. D.1 Test plan and realization with COX samples drilled in different directions

TC: triaxial compression test at constant stress

TE: triaxial extension test at constant axial stress

TM: triaxial test at constant mean stress

TCD: triaxial compression test at constant strain rate

TCC: triaxial creep test at constant triaxial stress state

x: test was planned and performed

f: test was failed due to sample damage

OHZ6560: $\alpha = 90^\circ$										
Core ID	confine-ment	top (m)	end (m)	depth (m)	TCD-test $\sigma_r = 5 \text{ MPa}$ $\dot{\varepsilon}_a = 1 \cdot 10^{-5} / \text{s}$	TCS-test $\sigma_r = 5 \text{ MPa}$ $\dot{\sigma}_a = 7 \cdot 10^{-3} \text{ MPa/s}$	TES-test $\sigma_a = 5 \text{ MPa}$ $\dot{\sigma}_r = 7 \cdot 10^{-3} \text{ MPa/s}$	TEM-test $\sigma_m = 13.7 \text{ MPa}$ $\dot{\sigma}_a = 7 \cdot 10^{-3} \text{ MPa/s}$	TCC-test $\sigma_a \geq 15 \text{ MPa}$ $\sigma_r = 5 \text{ MPa}$	
EST49093	CP13504	5,33	5,53	5,43			f			
EST49095	T12097	5,64	5,96	5,80					x	
EST49097	CP13504	6,09	6,29	6,19				x		
EST49099	CP13505	6,90	7,10	7,00			x			
EST49101	T12098	7,17	7,49	7,33	f					
EST49103	CP13505	7,56	7,76	7,66					f	
EST49105	CP13505	8,40	8,60	8,50				x		
EST49106	T12099	8,65	8,95	8,80			x			x
EST49108	CP13505	9,12	9,32	9,22				f		
EST49111	T12101	9,80	10,10	9,95	x, x					
EST49113	T12102	10,31	10,61	10,46					x	

OHZ6561: $\alpha = 60^\circ$									
Core ID	CP	4,91	5,11	5,01		f			
EST49073	CP13500	4,91	5,11	5,01		f			
EST49074	T12094	5,15	5,45	5,30	f			x	
EST49075	CP13500	5,50	5,71	5,61					
EST49077	CP13500	5,99	6,19	6,09	f	x			
EST49078	T12095	6,24	6,56	6,40				f	
EST49079	CP13500	6,61	6,81	6,71			x		
EST49081	CP13501	7,00	7,20	7,10			x		
EST49082	T12096	7,25	7,57	7,41		x			x
EST49083	CP13501	7,26	7,82	7,54			f		

OHZ6562: $\alpha = 45^\circ$

EST49051	CP13497	5,94	6,14	6,04		f			
EST49052	T12091	6,20	6,51	6,36				f	
EST49053	CP13497	6,56	6,76	6,66				x	
EST49055	CP13497	6,89	7,09	6,99		x			
EST49056	T12092	7,15	7,45	7,30	x, x				
EST49057	CP13497	7,50	7,70	7,60			x		
EST49060	CP13497	8,45	8,65	8,55			x		
EST49061	T12093	8,70	9,00	8,85					x
EST49062	CP13497	9,05	9,25	9,15				x	

OHZ6563: $\alpha = 30^\circ$

EST48974	CP13481	5,40	5,60	5,50		f			
EST48975	T12086	5,65	5,97	5,81				x	
EST48976	CP13481	6,15	6,35	6,25				x	
EST48978	CP13481	6,35	6,55	6,45		x			
EST48979	T12087	6,65	6,97	6,81					x
EST48980	CP13482	7,02	7,22	7,12			x		
EST48982	CP13482	7,24	7,44	7,34			x		
EST48983	T12088	7,49	7,81	7,65	x, x				x
EST48984	CP13482	7,86	8,06	7,96				x	

OHZ6564/5: $\alpha = 0^\circ$

EST49014	CP13489	5,22	5,42	5,32		f			
EST49015	T12089	5,47	5,79	5,63				x	
EST49017	CP13489	5,87	6,07	5,97	f				
EST49019	CP13490	7,02	7,22	7,12		x			
EST49020	T12090	7,27	7,59	7,43				x	x
EST49021	CP13490	7,64	7,84	7,74			f		
EST49121	CP13508	2,74	2,94	2,84				f	
EST49122	T12104	2,99	3,29	3,14	x, x		x, x		
EST49124	CP13508	3,42	3,62	3,52		f			

E Appendix: Test data

E.1 TCD – triaxial compression tests with strain control

Tab. E.1 Characteristic parameters determined from the TCD compression tests

Basic properties of the samples before testing								
sample ID	D/L (mm)	angle to bedding α (°)	grain density (g/cm^3)	bulk density (g/cm^3)	dry density (g/cm^3)	initial porosity (%)	water content (%)	water saturation (%)
EST49122A	70/140	0	2,698	2,407	2,234	17,21	7,2	93,5
EST49122B	70/140	0	2,698	2,410	2,236	17,11	7,2	94,1
EST48979A	70/140	30	2,700	2,420	2,248	16,73	7,1	95,4
EST49056A	70/90	45	2,703	2,430	2,260	16,39	7,0	96,5
EST49056B	70/85	45	2,703	2,395	2,227	17,60	7,0	88,6
EST49111A	70/130	90	2,688	2,390	2,218	17,49	7,2	91,3
mean value			2,697	2,408	2,236	17,08	7,13	93,4
standard deviation			0,006	0,013	0,013	0,386	0,088	2,454

Hydrostatic pre-compaction up to 16 MPa							
sample ID	angle to bedding α (°)	max. mean stress σ_m (MPa)	max. axial strain ε_{a-m} (%)	max. radial strain ε_{r-m} (%)	max. volume strain ε_{v-m} (%)	bulk modulus K (GPa)	anisotropy ratio R (-)
EST49122A	0	16	0,18	0,20	0,56	4,75	2,16
EST49122B	0	16	0,16	0,16	0,48	3,49	x
EST48979A	30	16	0,17	0,21	0,58	6,76	2,83
EST49056A	45	16	0,28	0,11	0,51	7,79	x
EST49056B	45	16	0,32	x	x	x	x
EST49111A	90	16	0,30	0,08	0,32	5,22	1,65
EST49111B	90	16	0,30	x	x	x	x
mean value			0,24	0,13	0,45	5,60	2,21
standard deviation			0,065	0,072	0,116	1,514	0,483
sample ID	angle to bedding α (°)	max. mean stress σ_m (MPa)	bulk density (g/cm^3)	dry density (g/cm^3)	porosity (%)	water content (%)	water saturation (%)
EST49122A	0	16	2,421	2,246	16,74	7,2	96,6
EST49122B	0	16	2,422	2,247	16,71	7,2	96,9
EST48979A	30	16	2,434	2,261	16,25	7,1	98,8
EST49056A	45	16	2,438	2,267	15,98	7,0	98,4
EST49056B	45	16	2,398	2,225	17,23	7,0	93,0
EST49111A	90	16			7,2		
EST49111B	90	16			7,20		
mean value			2,422	2,249	16,61	7,13	96,7
standard deviation			0,014	0,015	0,392	0,088	2,051

Deviatoric loading at constant radial stress of 5 MPa								
sample ID	angle to bedding α ($^{\circ}$)	radial stress (MPa)	Young's modulus E (GPa)	anisotropy ratio R (-)	Poisson's ratio ν (-)	peak strength σ_F (MPa)	failure strain ε_{a-f} (%)	fracture angle β ($^{\circ}$)
EST49122A	0	5	6,0-12,0	1,0-2,6	0,13-0,36	30,4	1,03	21,0
EST49122B	0	5	8,0-10,0	x	x	30,4	1,00	20,0
EST48979A	30	5	8,2-9,6	2,4-2,5	0,37-0,47	25,4	0,65	25,0
EST49056A	45	5	2,8-8,4	0,3-2,2	0,08-0,21	27,4	0,85	28,0
EST49056B	45	5	2,1-6,1	x	0,02-0,19	22,3	0,96	35,0
EST49111A	90	5	3,5-6,4	x	0,20-0,29	25,8	1,07	32,0
EST49111B	90	5	3,3-6,4	x	0,20-0,34	27,2	1,20	30,0
mean value						27,0	0,97	27,3
standard deviation						2,66	0,16	5,18

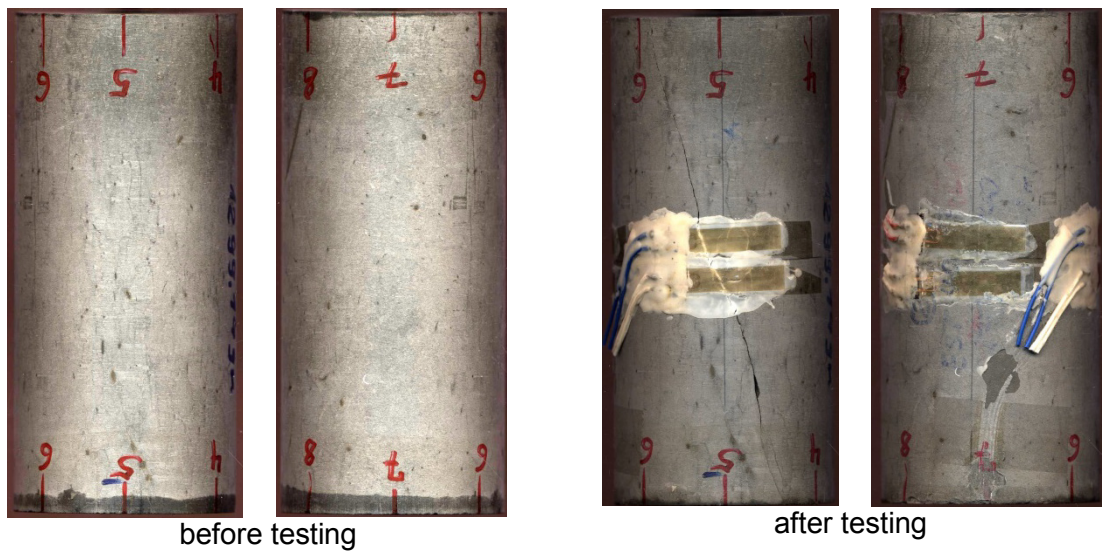


Fig. E.1 Sample EST49122A in axial load orientation $\alpha = 0^\circ$ with respect to bedding

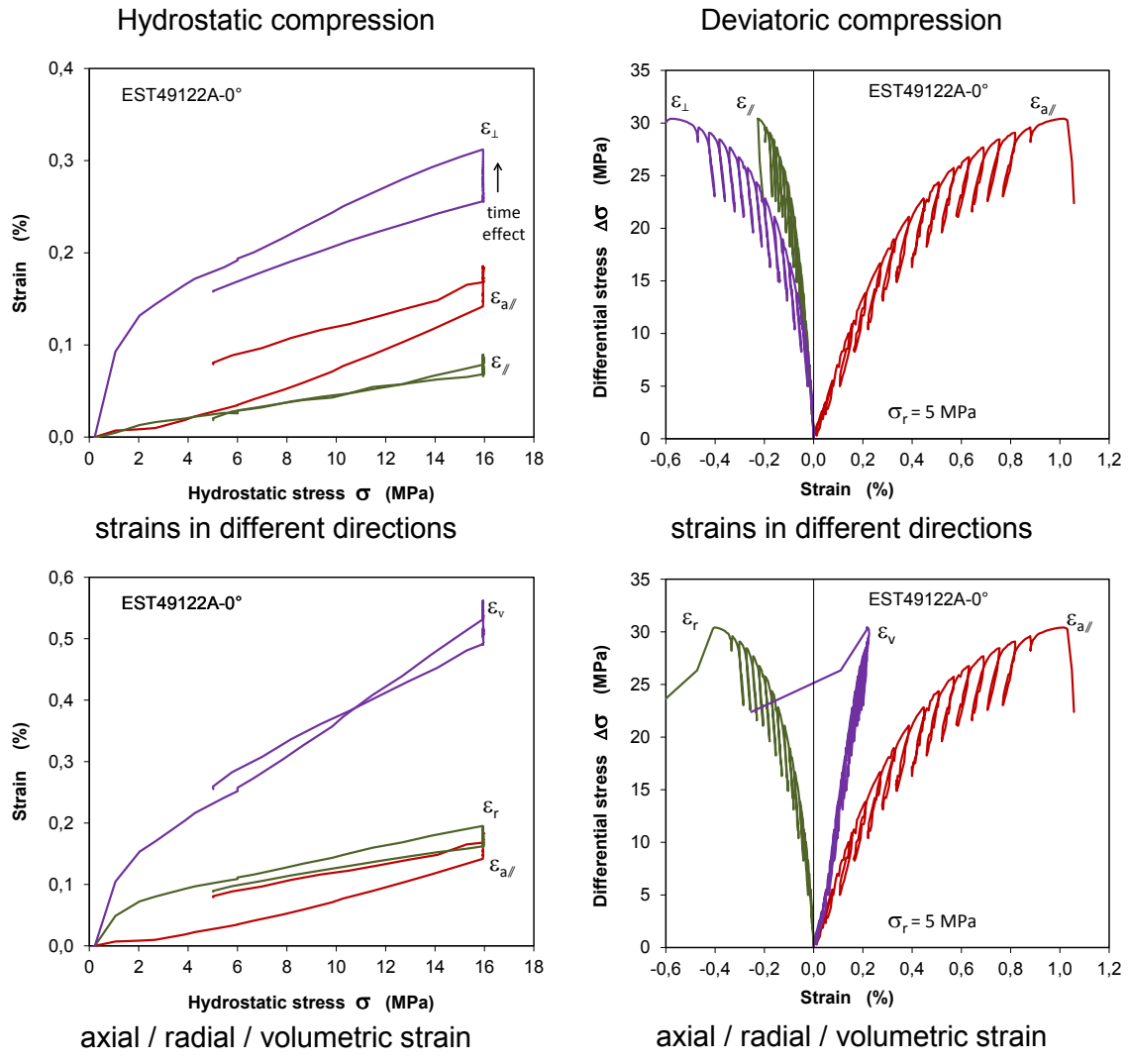


Fig. E.2 Stress-strain curves during hydrostatic pre-compaction and deviatoric loading

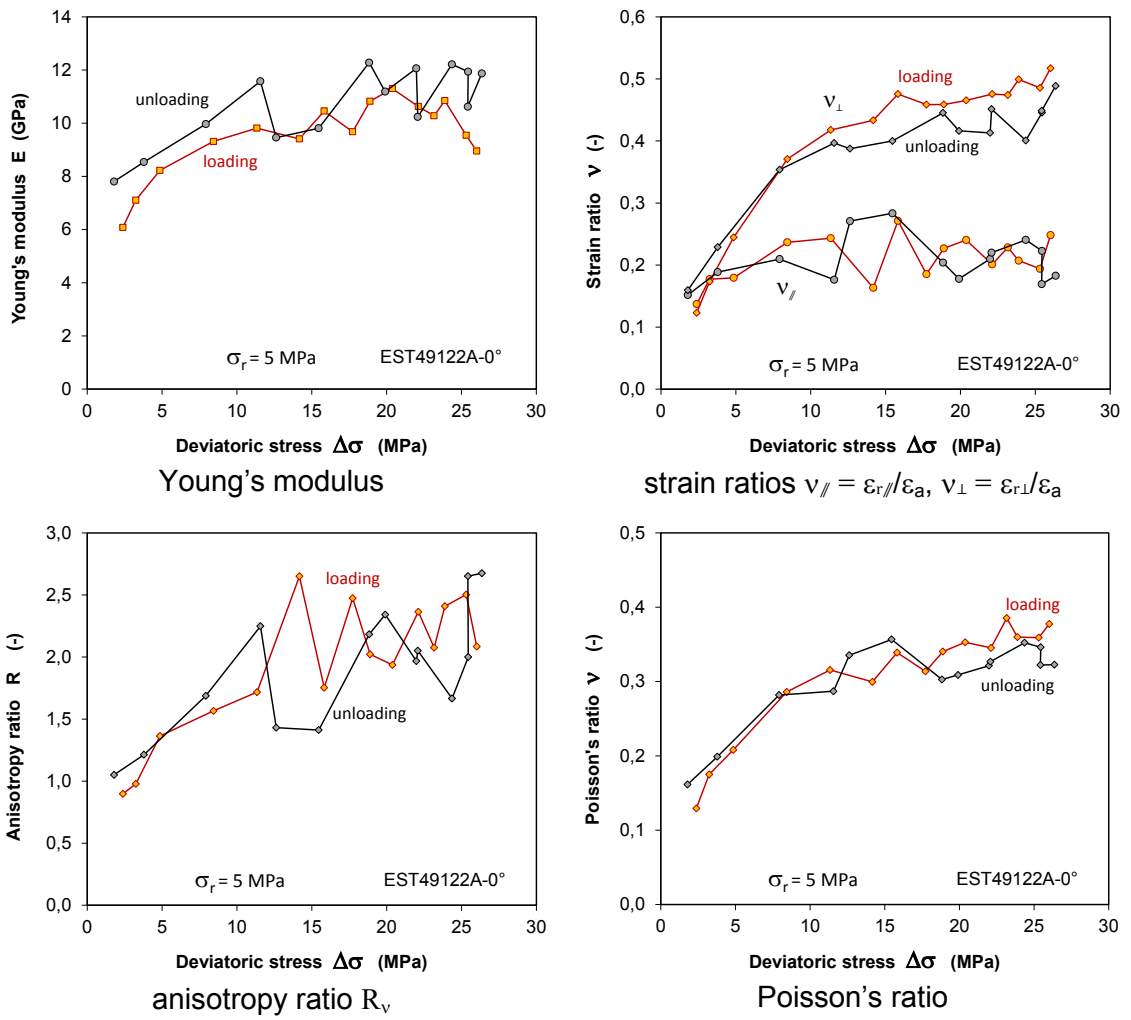


Fig. E.3 Elastic parameters as a function of applied deviatoric stress

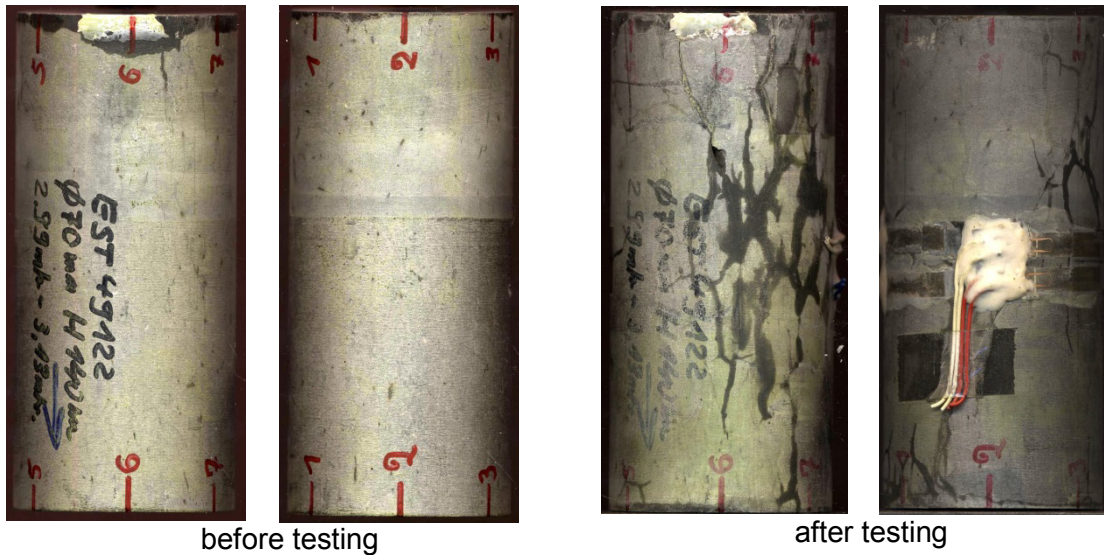


Fig. E.4 Sample EST49122B in axial load orientation $\alpha = 0^\circ$ with respect to bedding

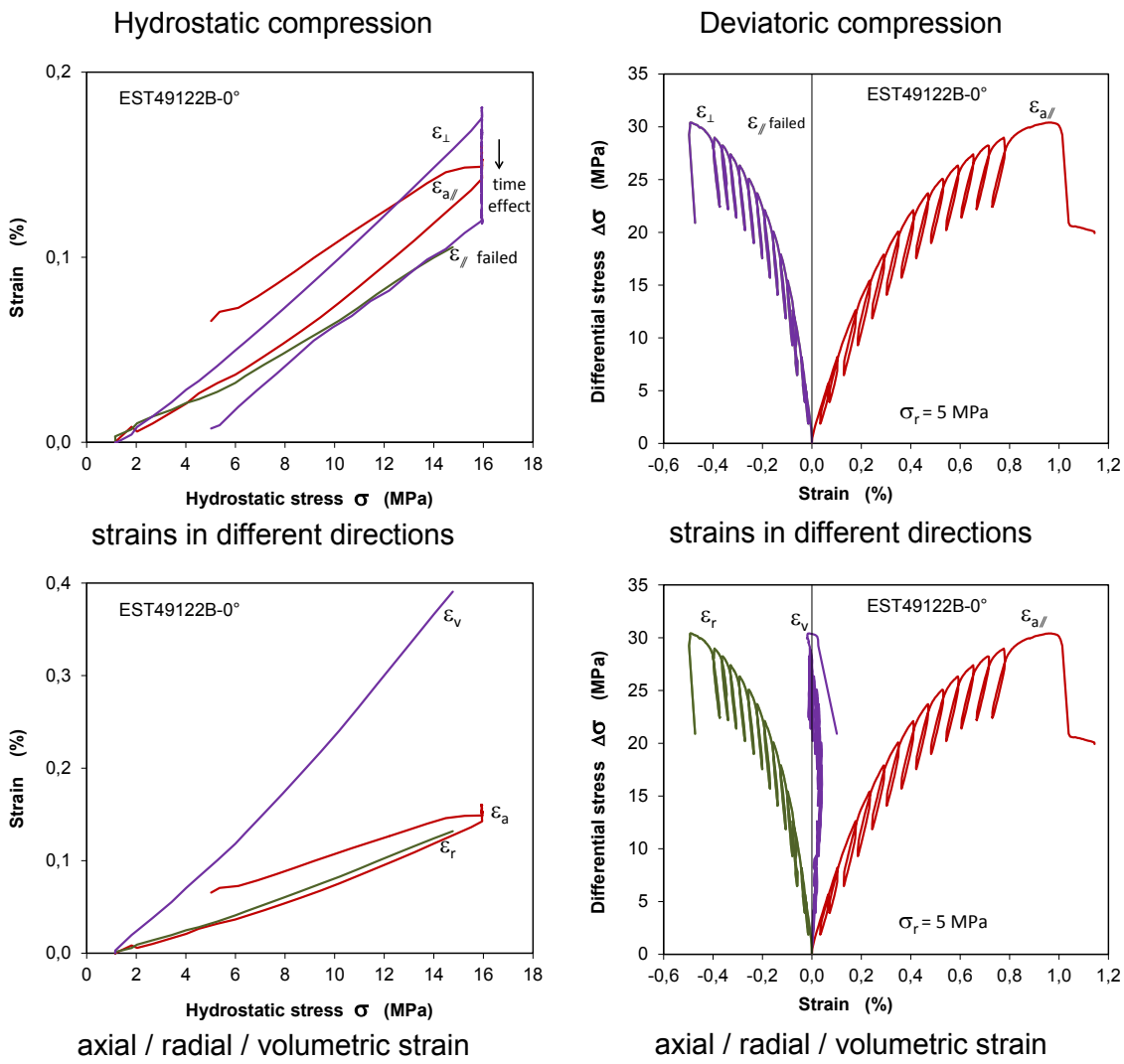


Fig. E.5 Stress-strain curves during hydrostatic pre-compaction and deviatoric loading

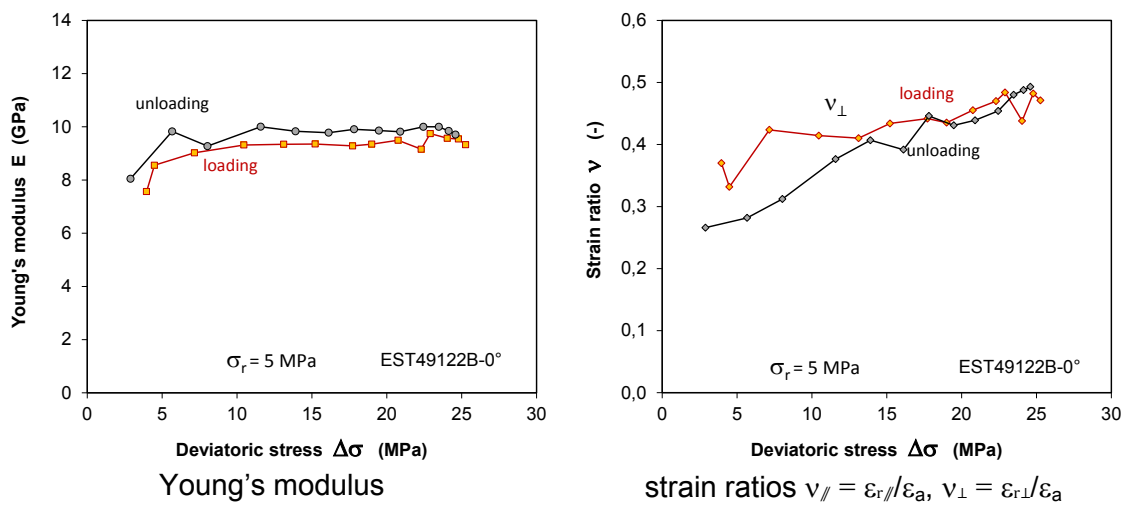


Fig. E.6 Elastic parameters as a function of applied deviatoric stress

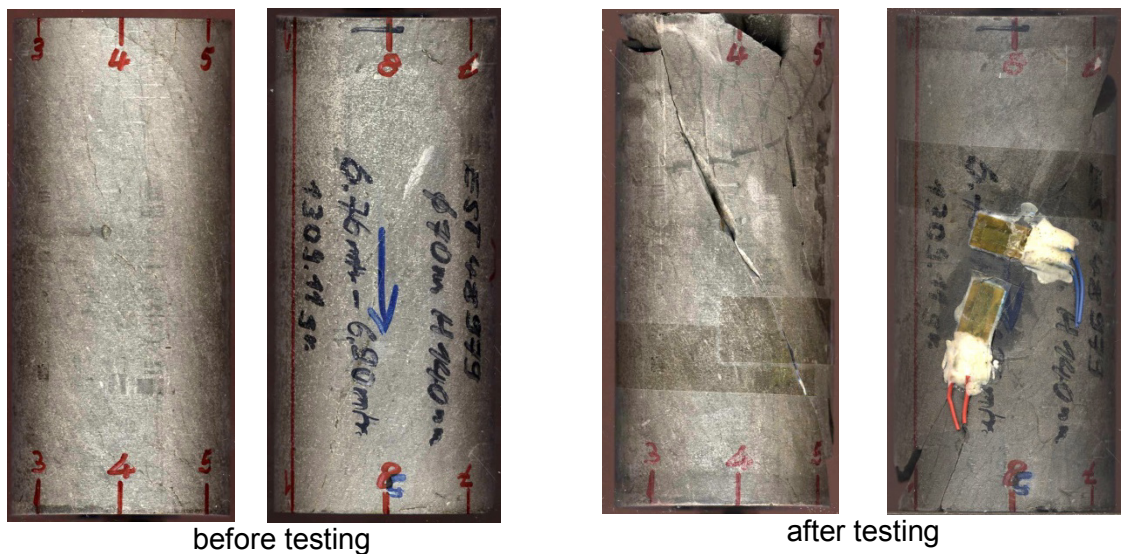


Fig. E.7 Sample EST48979A in axial load orientation $\alpha = 30^\circ$ with respect to bedding

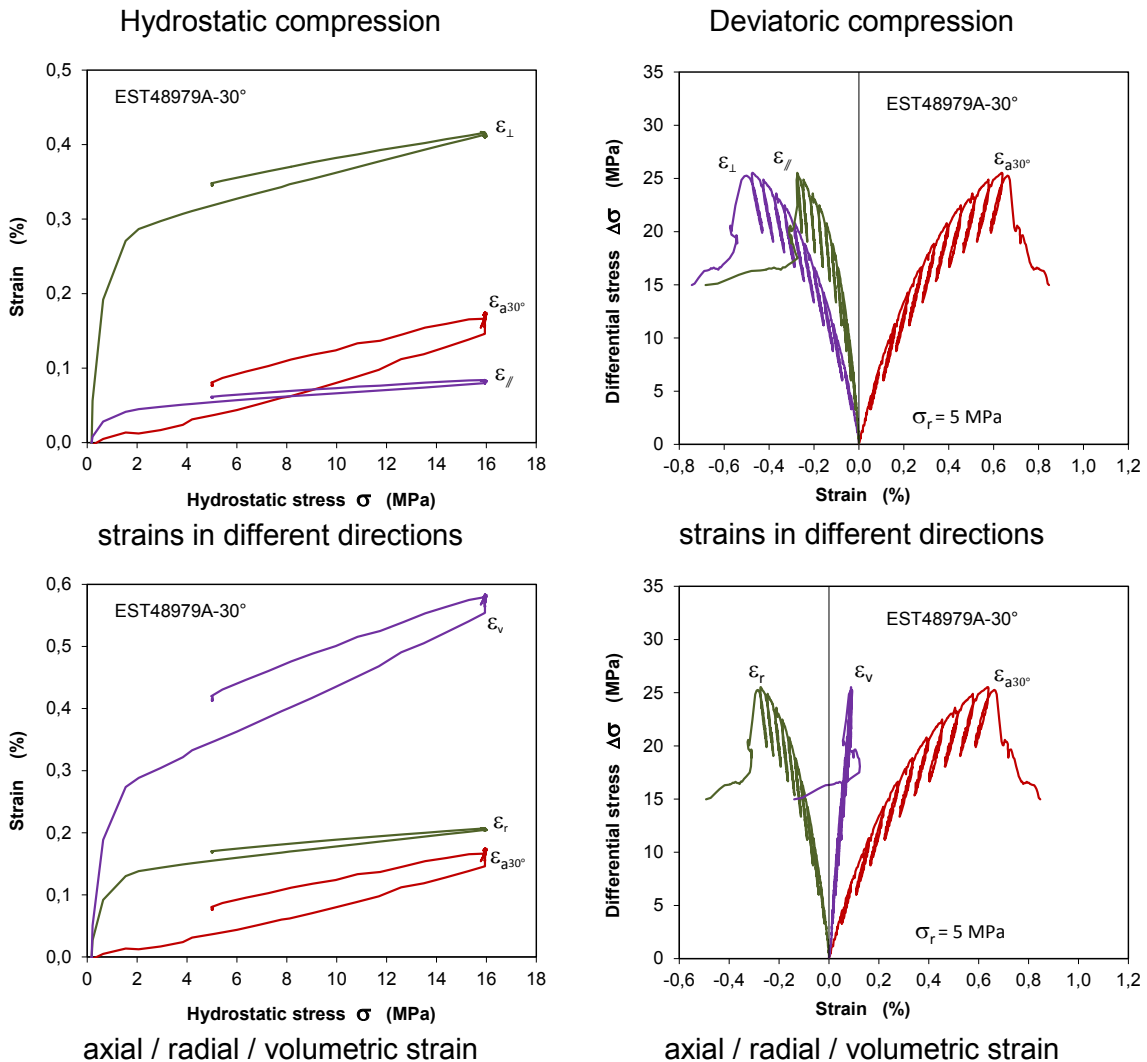


Fig. E.8 Stress-strain curves during hydrostatic pre-compaction and deviatoric loading

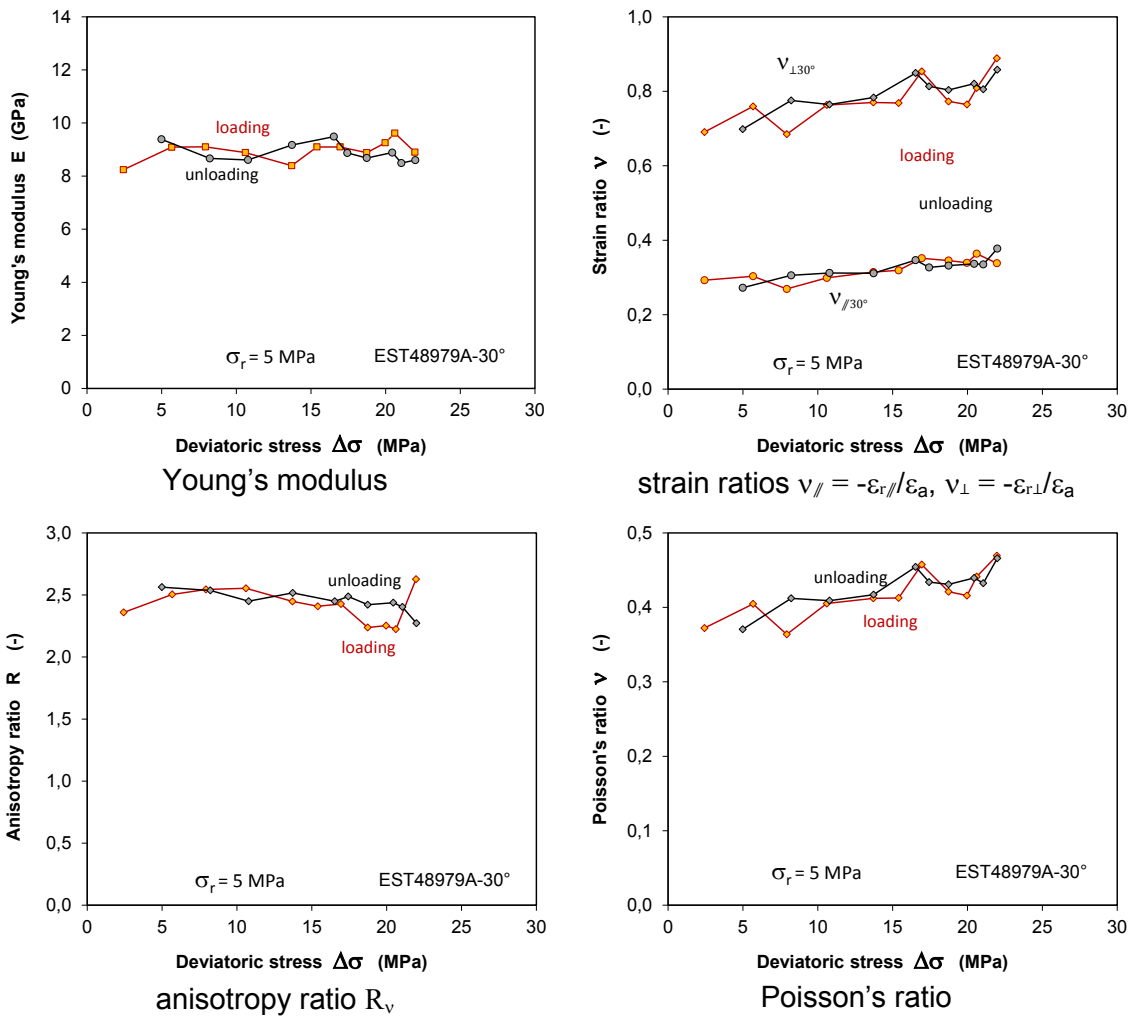


Fig. E.9 Elastic parameters as a function of applied deviatoric stress

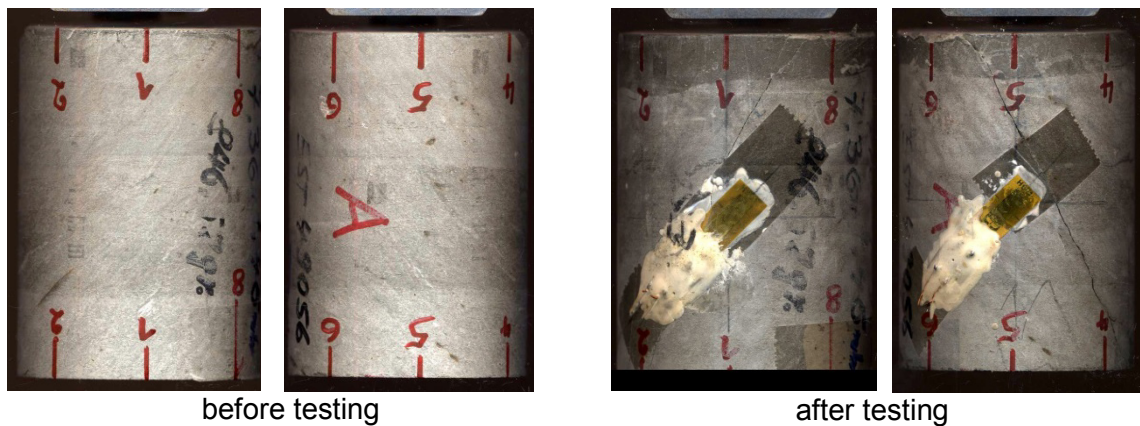


Fig. E.10 Sample EST49056A in axial load orientation $\alpha = 45^\circ$ with respect to bedding

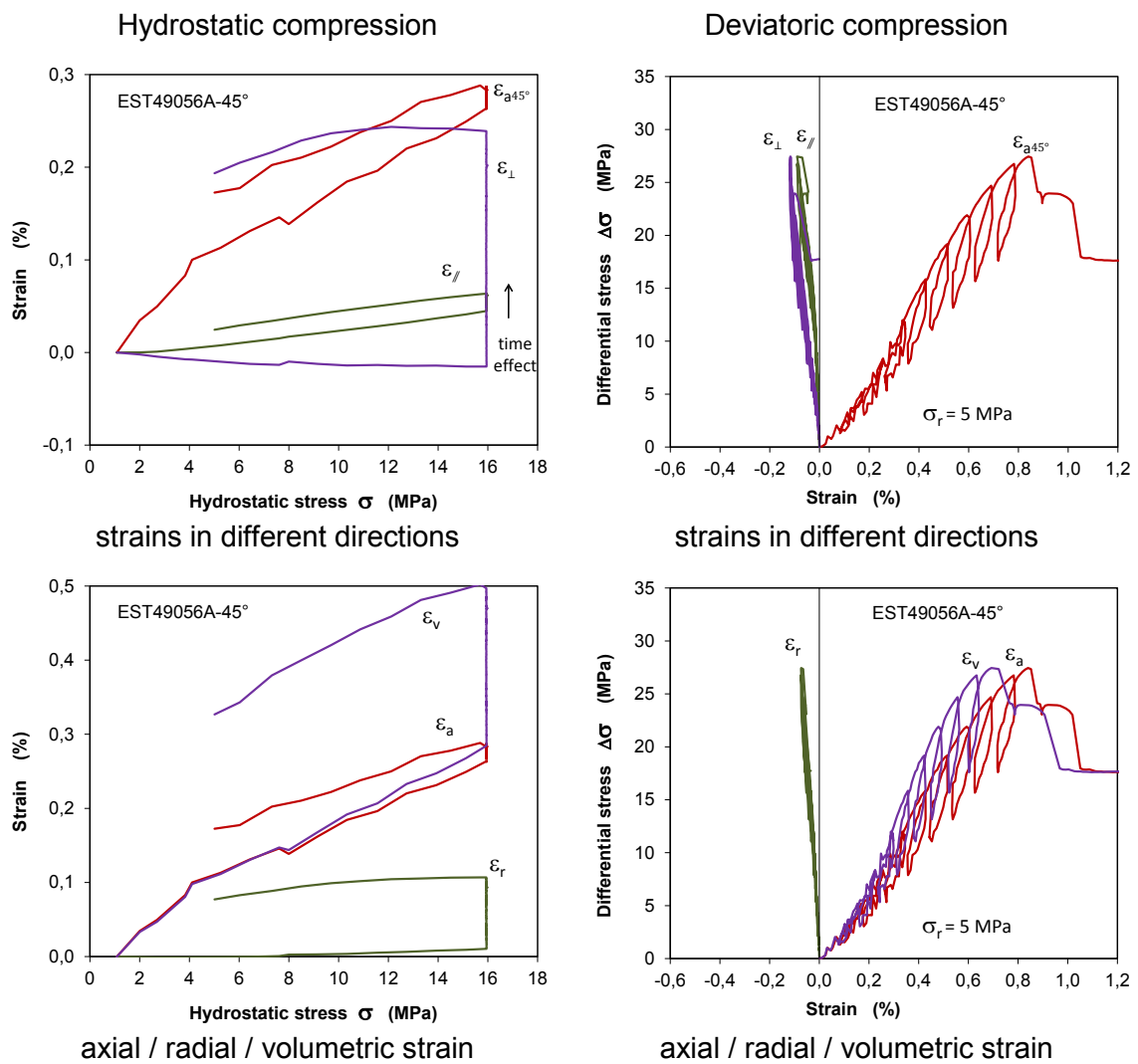


Fig. E.11 Stress-strain curves during hydrostatic pre-compaction and deviatoric loading

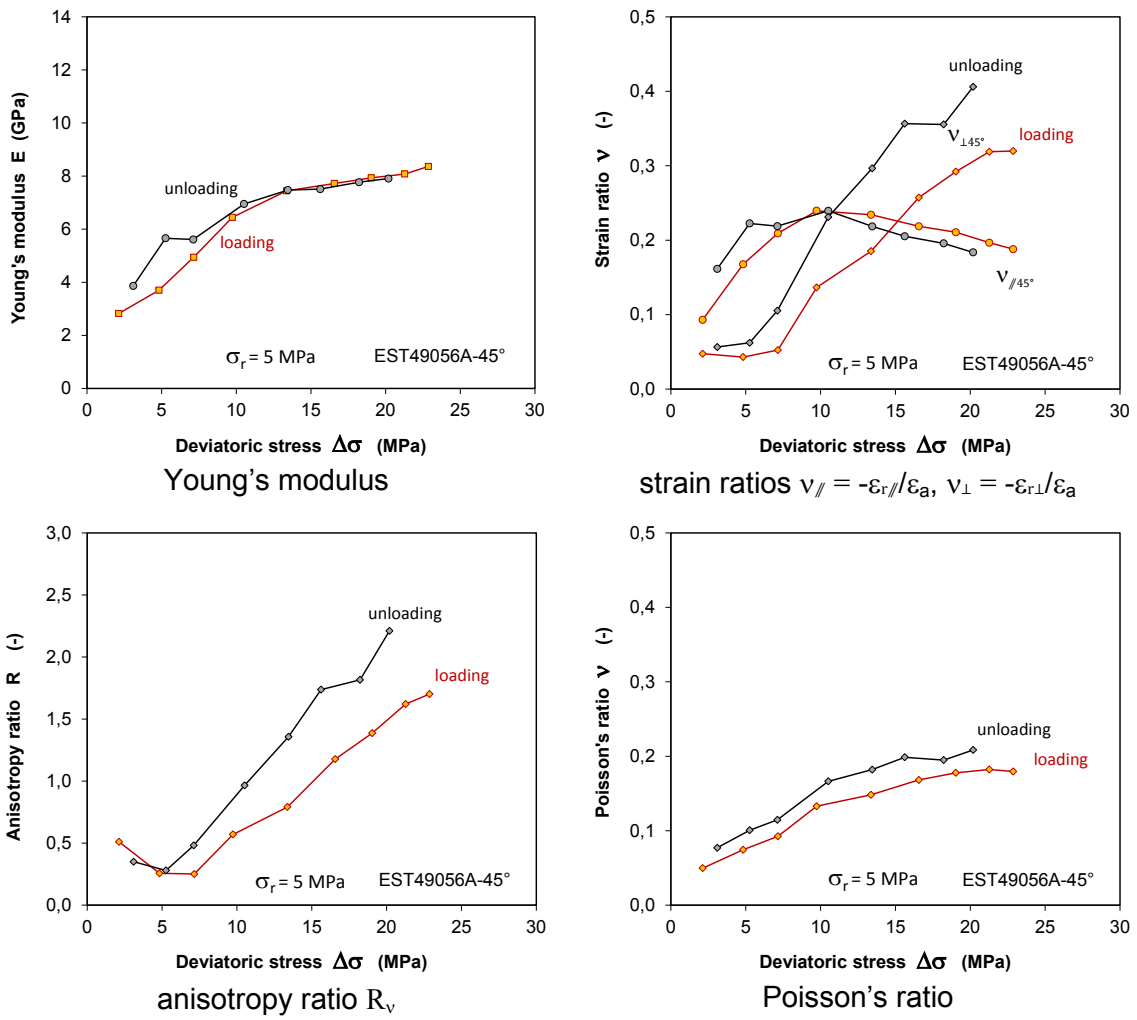


Fig. E.12 Elastic parameters as a function of applied deviatoric stress

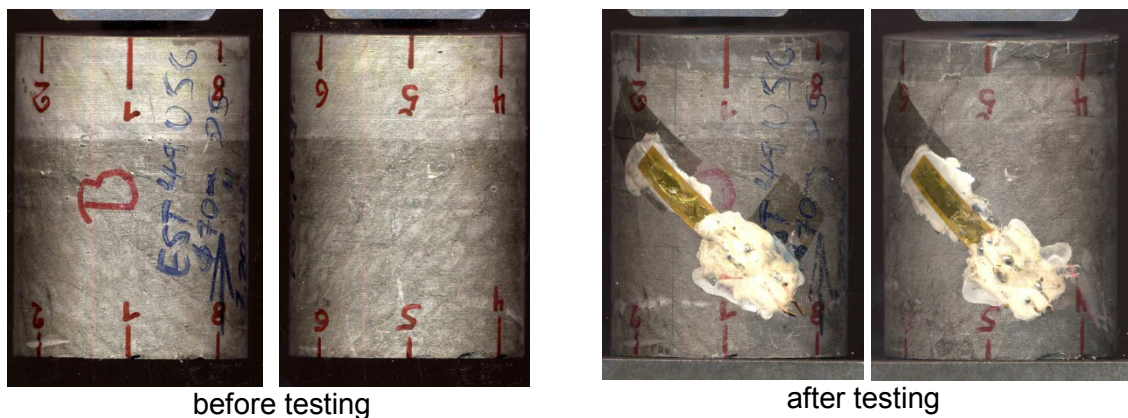


Fig. E.13 Sample EST49056B in axial load orientation $\alpha = 45^\circ$ with respect to bedding

Hydrostatic compression

Deviatoric compression

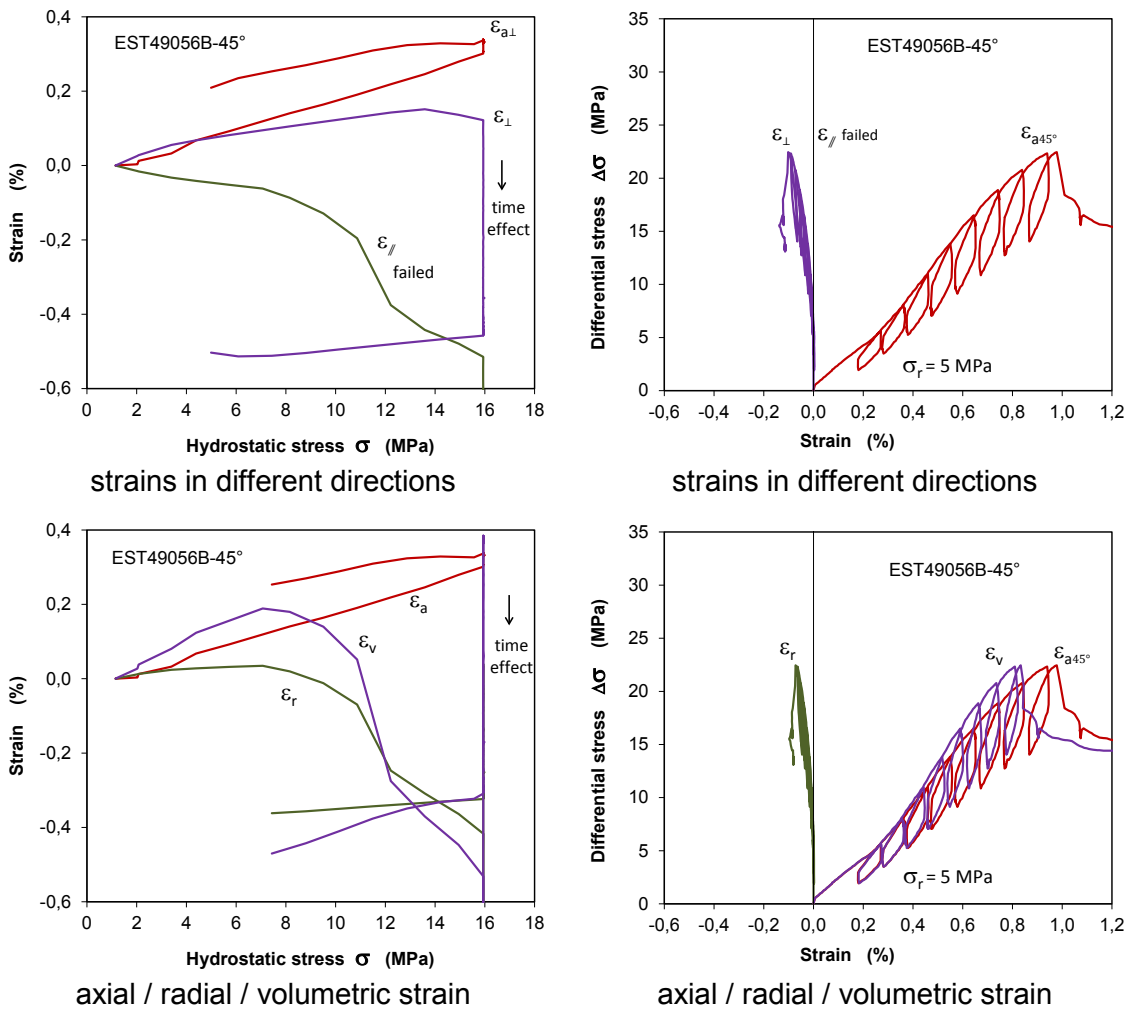


Fig. E.14 Stress-strain curves during hydrostatic pre-compaction and deviatoric loading

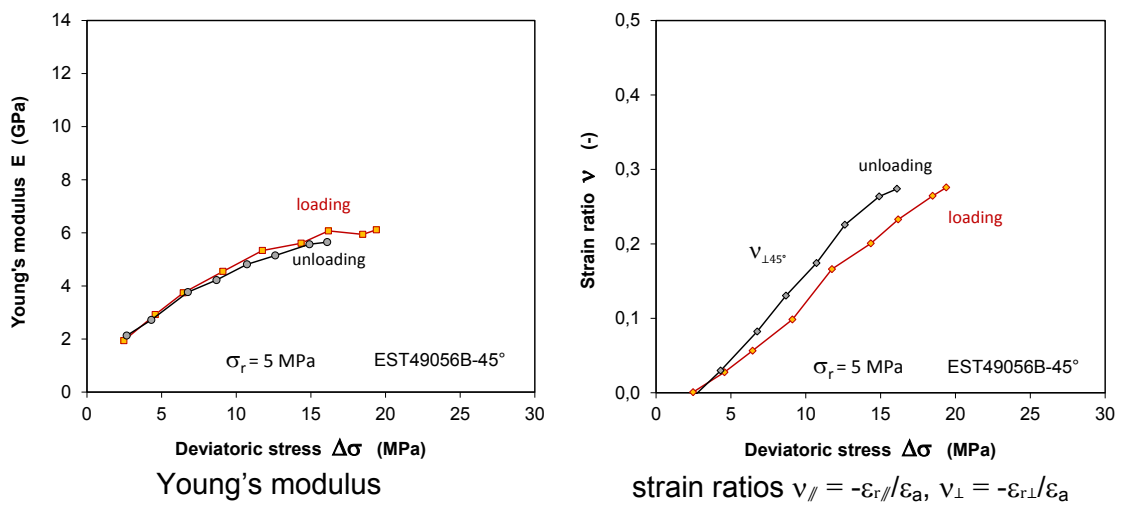


Fig. E.15 Elastic parameters as a function of applied deviatoric stress

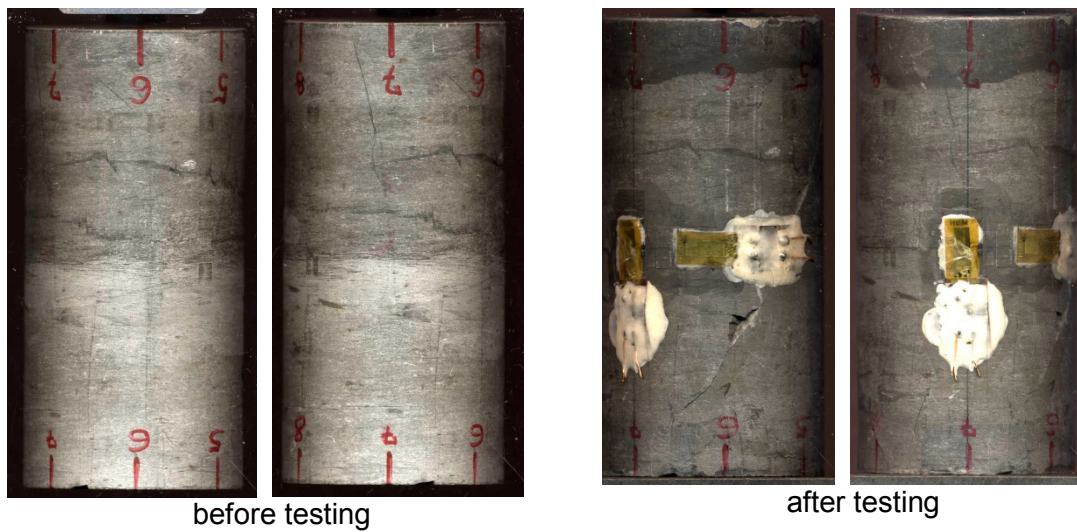


Fig. E.16 Sample EST49111A in axial load orientation $\alpha = 90^\circ$ with respect to bedding

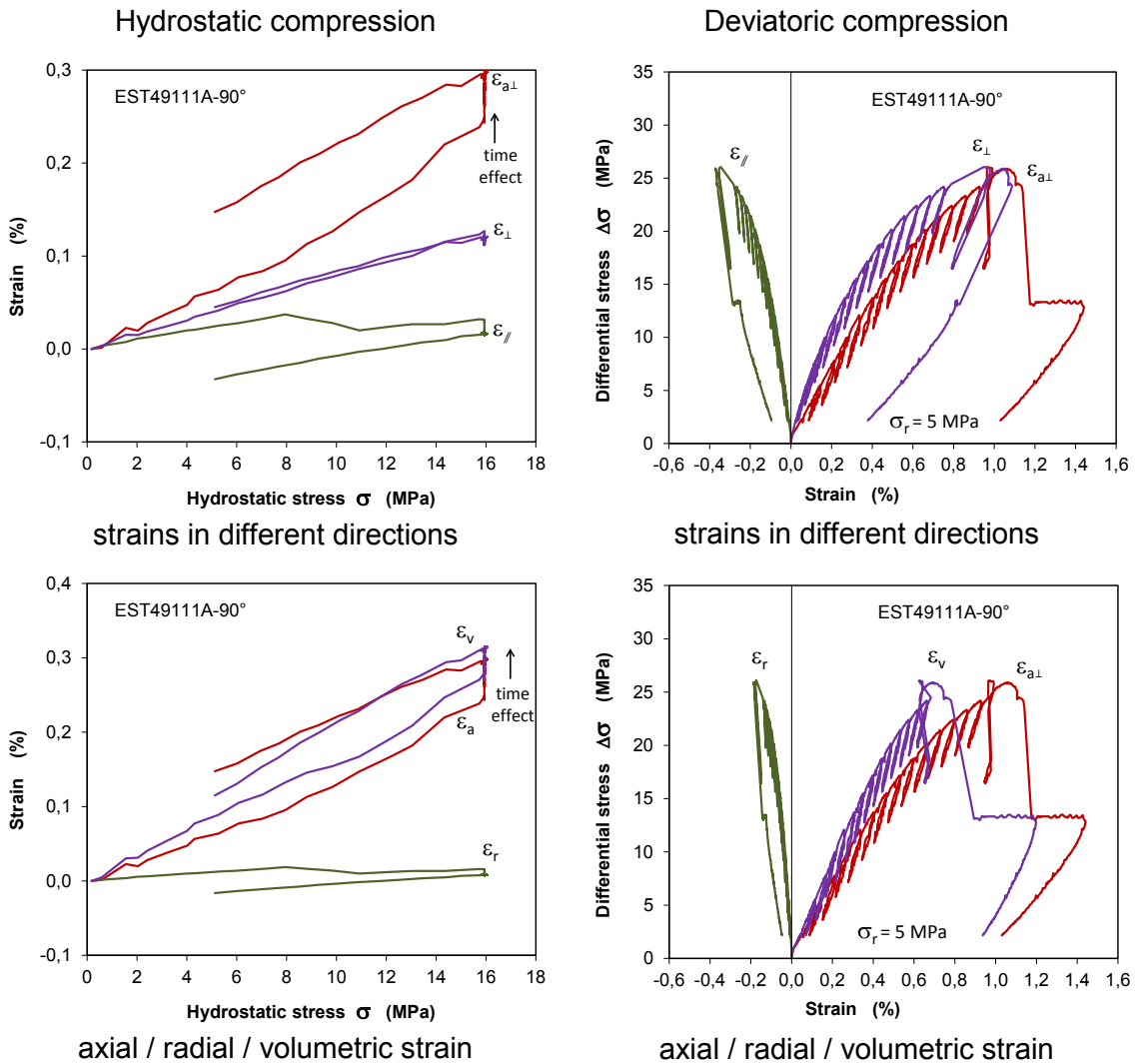


Fig. E.17 Stress-strain curves during hydrostatic pre-compaction and deviatoric loading

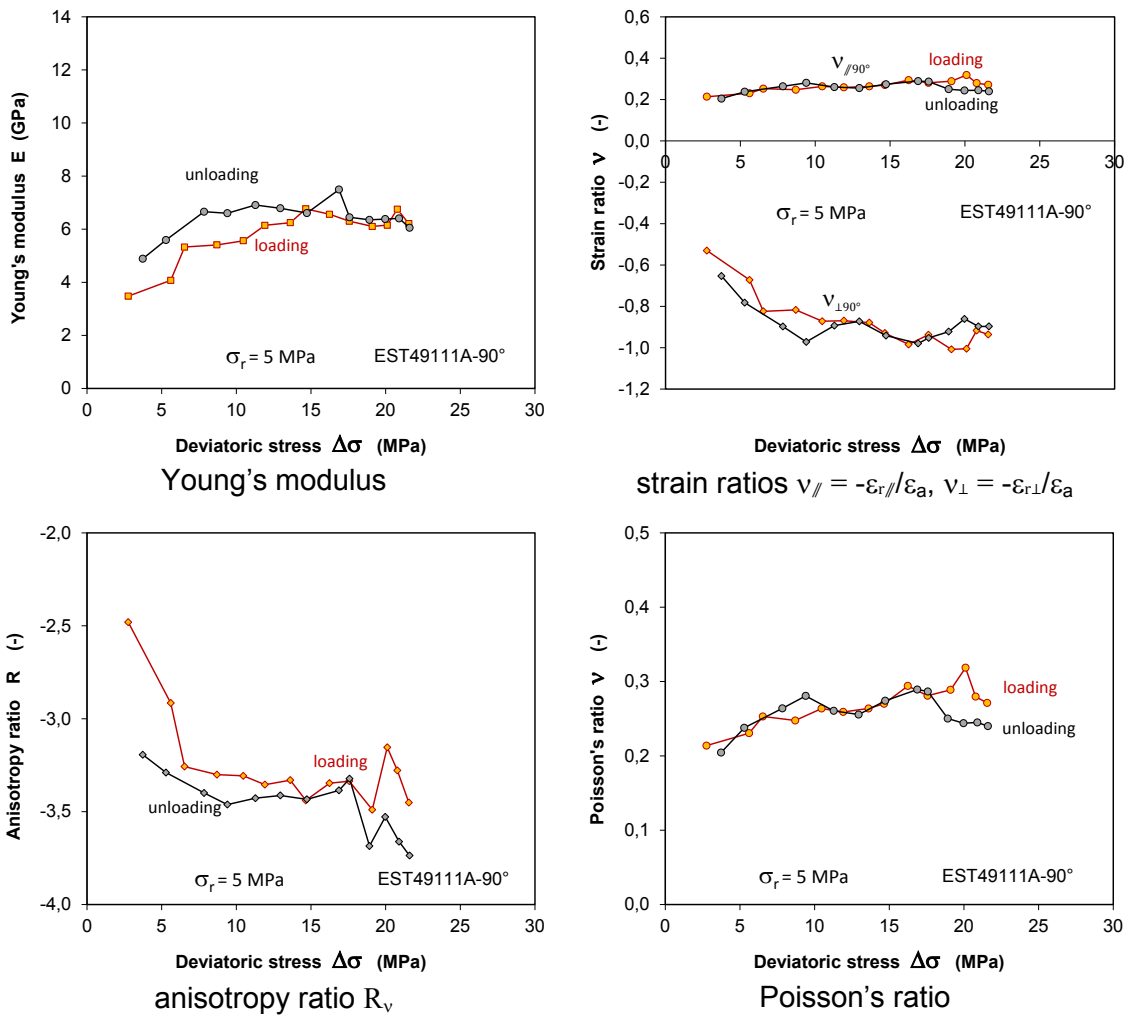


Fig. E.18 Elastic parameters as a function of applied deviatoric stress

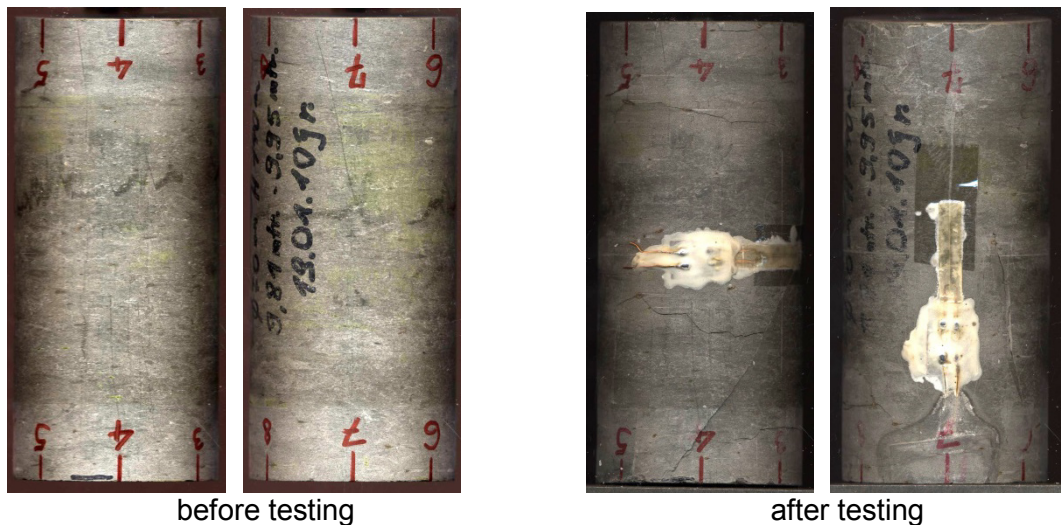


Fig. E.19 Sample EST49111B in axial load orientation $\alpha = 90^\circ$ with respect to bedding

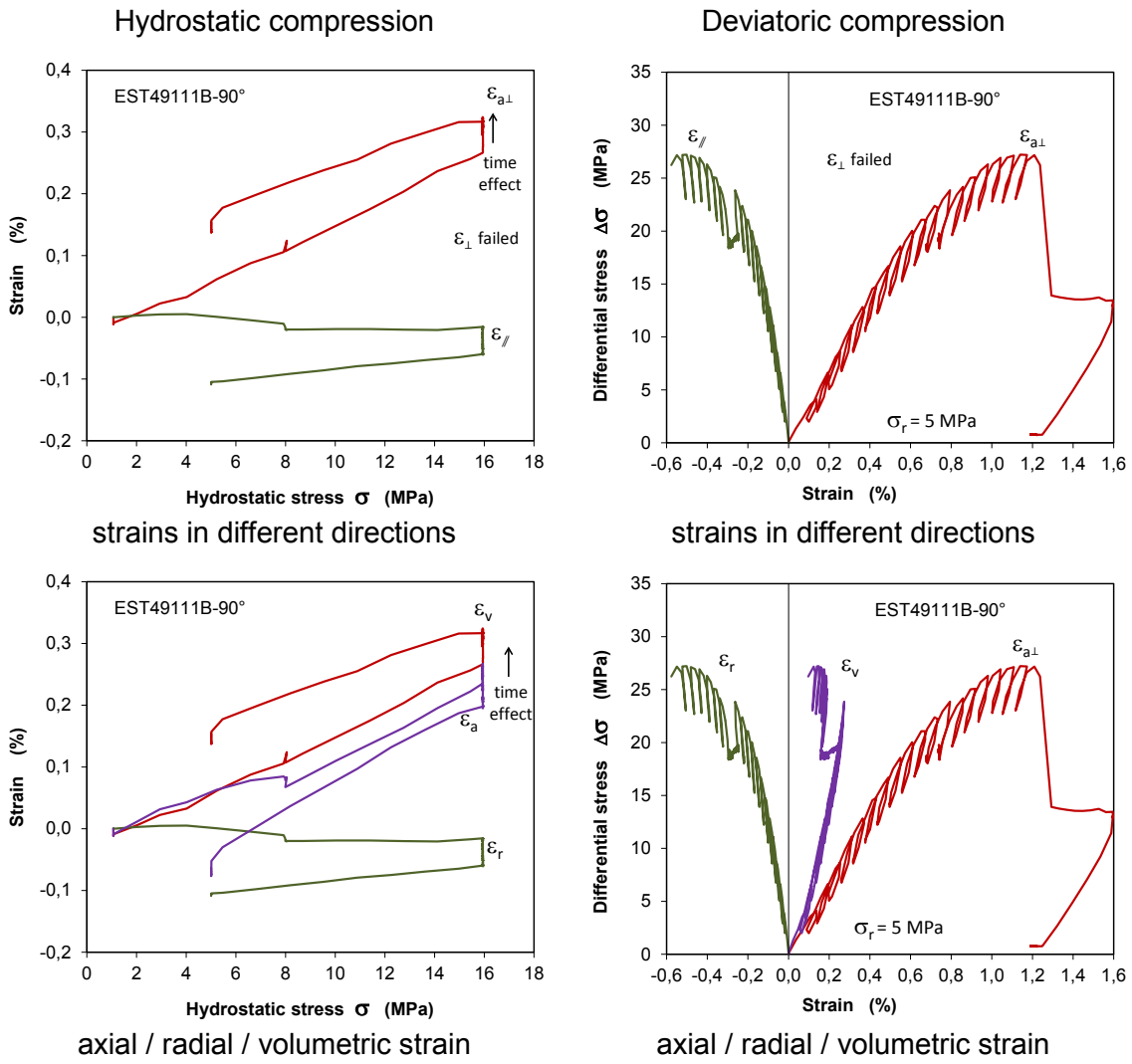


Fig. E.20 Stress-strain curves during hydrostatic pre-compaction and deviatoric loading

Elastic parameters as a function of applied deviatoric stress

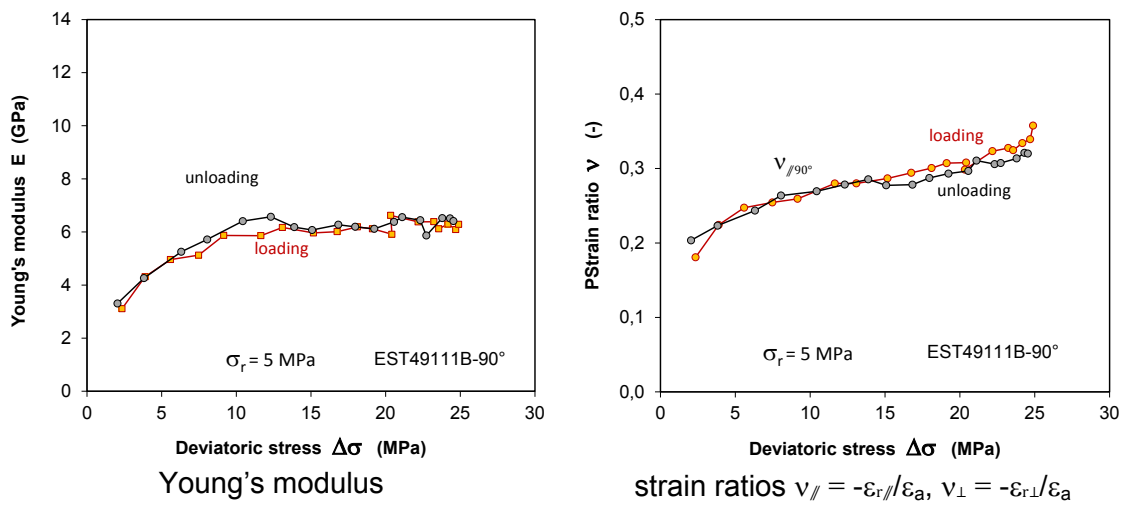


Fig. E.21 Elastic parameters as a function of applied deviatoric stress

E.2 TCS – triaxial compression tests with stress control

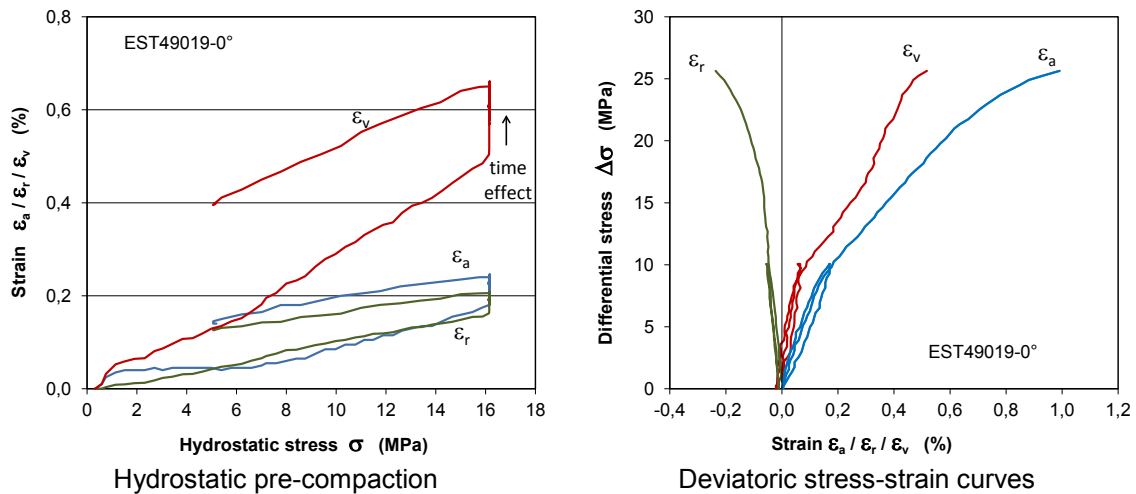
Tab. E.2 Characteristic parameters determined from the TC stress-controlled tests

Basic properties of the samples before testing								
sample ID	D/L (mm)	angle to bedding α (°)	grain density (g/cm³)	bulk density (g/cm³)	dry density (g/cm³)	initial porosity (%)	water content (%)	water saturation (%)
EST49106	50/100	0	2,698	2,422	2,244	16,81	7,3	97,9
EST49082	50/100	30	2,708	2,428	2,266	16,33	6,7	92,7
EST49055	50/100	45	2,703	2,397	2,221	17,85	7,4	91,6
EST49077	50/100	60	2,680	2,400	2,225	16,99	7,3	95,6
EST49082	50/100	60	2,695	2,409	2,232	17,18	7,4	95,5
EST49099	50/100	90	2,700	2,450	2,281	15,52	6,9	101,4
EST49105	50/100	90	2,696	2,443	2,275	15,60	6,9	100,0
mean value			2,697	2,421	2,249	16,61	7,11	96,4
standard deviation			0,008	0,019	0,023	0,786	0,267	3,365

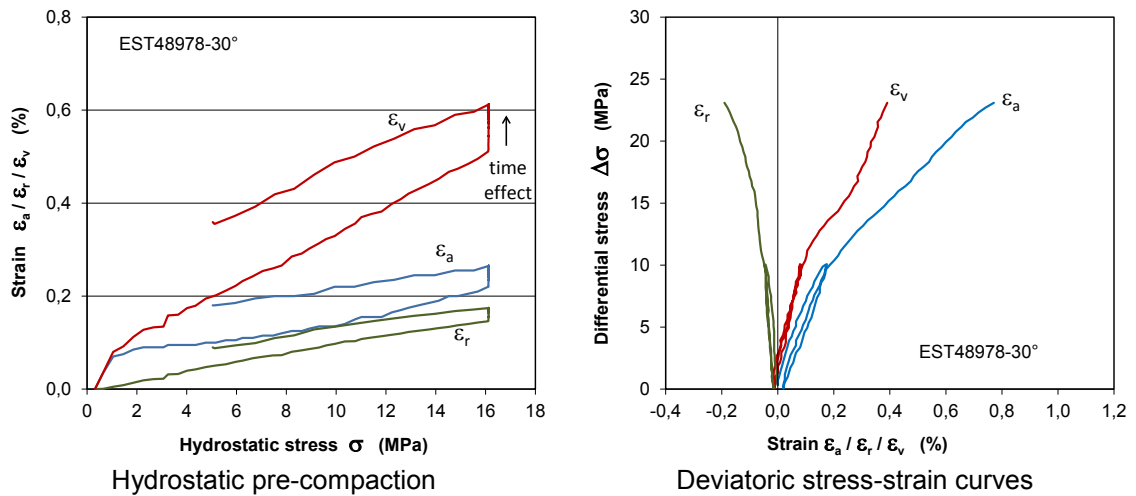
Hydrostatic pre-compaction up to 16 MPa							
sample ID	angle to bedding α (°)	max. mean stress σ_m (MPa)	max. axial strain ε_{a-m} (%)	max. radial strain ε_{r-m} (%)	max. volume strain ε_{v-m} (%)	bulk modulus K (GPa)	
EST49106	0	16	0,47	0,13	0,74	4,71	
EST49082	30	16	0,26	0,17	0,60	4,45	
EST49055	45	16	0,41	0,18	0,77	4,58	
EST49077	60	16	0,30	0,14	0,57	4,29	
EST49082	60	16	0,42	0,18	0,77	5,27	
EST49099	90	16	0,39	0,14	0,67	4,44	
EST49105	90	16	0,47	0,13	0,74	4,71	
mean value			0,39	0,15	0,69	4,64	
standard deviation			0,078	0,020	0,077	0,294	
sample ID	angle to bedding α (°)	max. mean stress σ_m (MPa)	bulk density (g/cm³)	dry density (g/cm³)	porosity (%)	water content (%)	water saturation (%)
EST49106	0	16	2,440	2,261	16,19	7,3	102,4
EST49082	30	16	2,443	2,280	15,82	6,7	96,2
EST49055	45	16	2,416	2,238	17,21	7,4	95,7
EST49077	60	16	2,414	2,237	16,51	7,3	98,9
EST49082	60	16	2,428	2,249	16,54	7,4	100,0
EST49099	90	16	2,467	2,296	14,95	6,9	101,0
EST49105	90	16	2,461	2,292	14,97	6,9	105,0
mean value			2,438	2,265	16,03	7,11	101,0
standard deviation			0,019	0,023	0,778	0,267	3,746

Deviatoric loading at constant radial stress of 5 MPa						
sample ID	angle to bedding α (°)	Young's modulus E (GPa)	Poisson's ratio ν (-)	peak strength σ_F (MPa)	failure strain ε_{a-f} (%)	fracture angle β (°)
EST49106	0	4,31	0,29	23,7	1,06	x
EST49082	30	5,48	0,23	23,1	0,77	25,0
EST49055	45	4,75	0,27	21,0	0,85	45,0
EST49077	60	4,92	0,24	23,9	0,92	30,0
EST49082	60	4,08	0,26	22,0	0,87	25,0
EST49099	90	5,29	0,22	27,4	1,17	25,0
EST49105	90	4,31	0,29	23,7	1,07	x
mean value		4,73	0,26	23,55	0,96	30,0
standard deviation		0,492	0,026	1,857	0,133	7,746

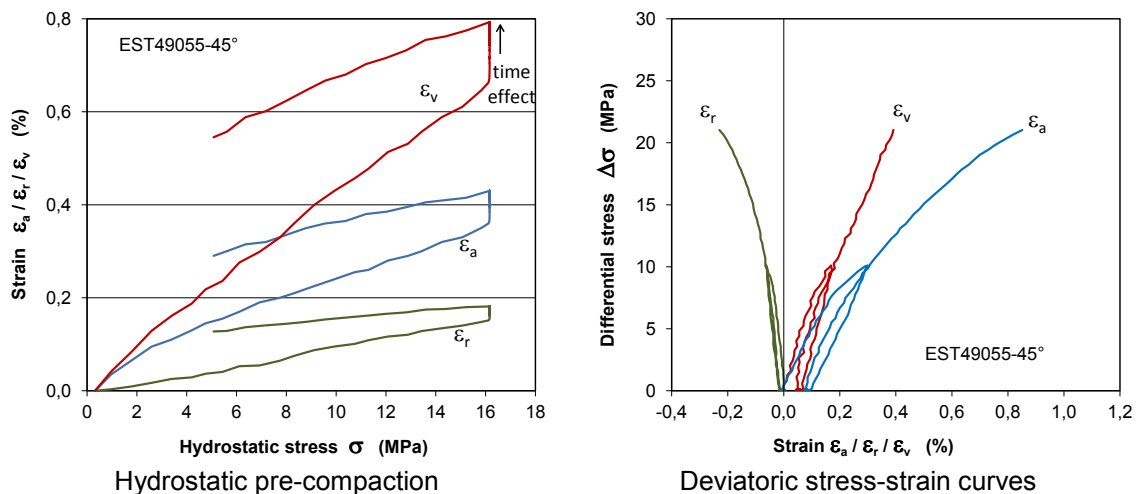
Axial loading orientation $\alpha = 0^\circ$



Axial loading orientation $\alpha = 30^\circ$



Axial loading orientation $\alpha = 45^\circ$



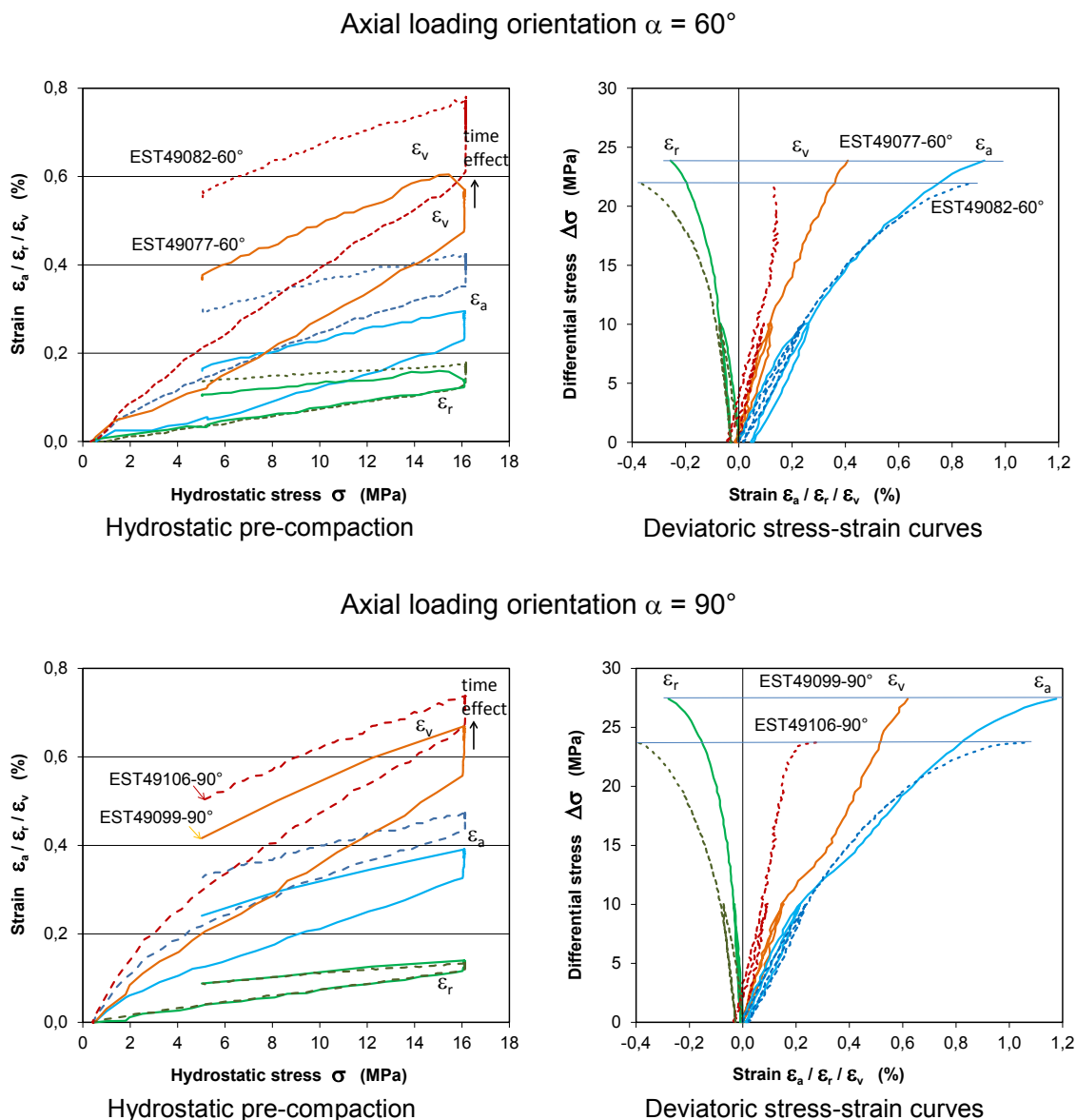


Fig. E.22 Stress-strain curves from TC hydrostatic and deviatoric compression

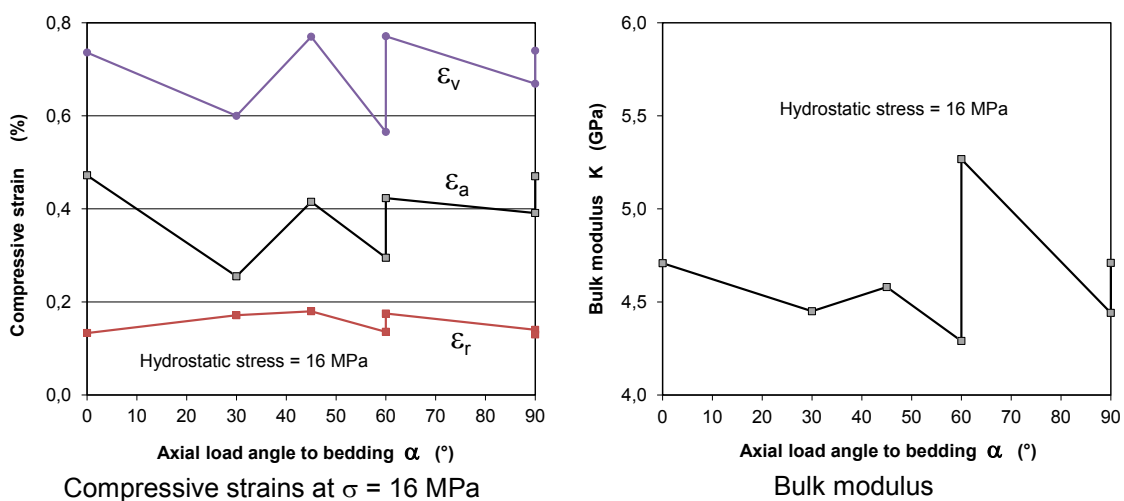


Fig. E.23 Parameters obtained from the TCS hydrostatic pre-compaction

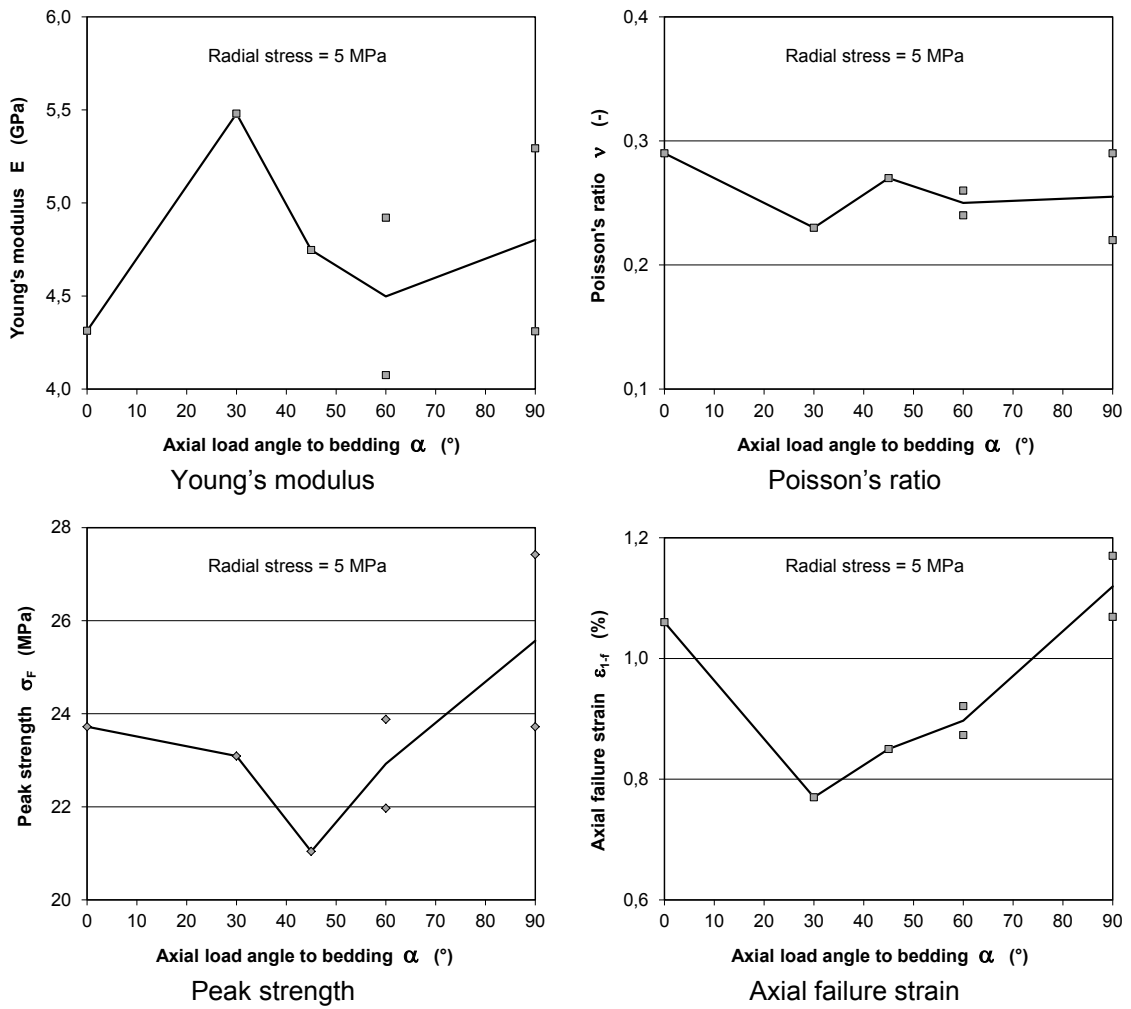


Fig. E.24 Parameters obtained from the TCS triaxial deviatoric compression

E.3 TES – triaxial extension tests at constant axial stress

Tab. E.3 Characteristic parameters determined from the TES extension tests

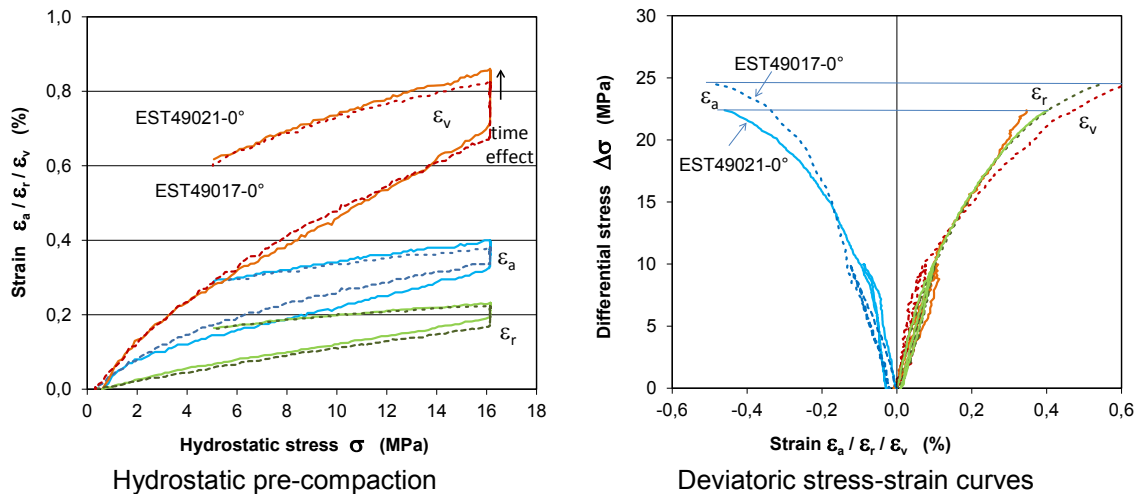
Basic properties of the samples before testing								
sample ID	D/L (mm)	angle to bedding α (°)	grain density (g/cm³)	bulk density (g/cm³)	dry density (g/cm³)	initial porosity (%)	water content (%)	water saturation (%)
EST49021	50/100	0	2,715	2,405	2,229	17,91	7,3	91,2
EST49017	50/100	0	2,690	2,410	2,229	17,13	7,5	97,6
EST48980	50/100	30	2,702	2,430	2,267	16,08	6,7	94,3
EST48982	50/100	30	2,690	2,420	2,243	16,60	7,3	98,6
EST49057	50/100	45	2,715	2,451	2,295	15,46	6,4	94,3
EST49060	50/100	45	2,690	2,440	2,281	15,19	6,5	97,6
EST49079	50/100	60	2,691	2,417	2,262	15,96	6,4	91,1
EST49081	50/100	60	2,690	2,400	2,225	17,29	7,3	93,9
EST49105	50/100	90	2,685	2,410	2,234	16,79	7,3	97,1
EST49097	50/100	90	2,696	2,407	2,239	16,93	7,0	92,0
Mean value			2,696	2,419	2,251	16,54	6,97	94,8
standard deviation			0,010	0,016	0,023	0,810	0,414	2,666

Hydrostatic pre-compaction up to 16 MPa						
sample ID	angle to bedding α (°)	max. mean stress σ_m (MPa)	max. axial strain ε_{a-m} (%)	max. radial strain ε_{r-m} (%)	max. volume strain ε_{v-m} (%)	bulk modulus K (GPa)
EST49021	0	16	0,40	0,23	0,86	4,62
EST49017	0	16	0,38	0,22	0,83	5,09
EST48980	30	16	0,38	0,18	0,74	4,62
EST48982	30	16	1,25	0,14	1,52	3,76
EST49057	45	16	0,26	0,16	0,58	5,58
EST49060	45	16	0,56	0,18	0,92	5,41
EST49079	60	16	0,47	0,14	0,74	4,58
EST49081	60	16	0,75	0,23	1,21	4,20
EST49105	90	16	1,13	0,09	1,32	4,15
EST49097	90	16	0,46	0,13	0,72	4,49
mean value			0,60	0,17	0,94	4,65
standard deviation			0,320	0,046	0,289	0,539

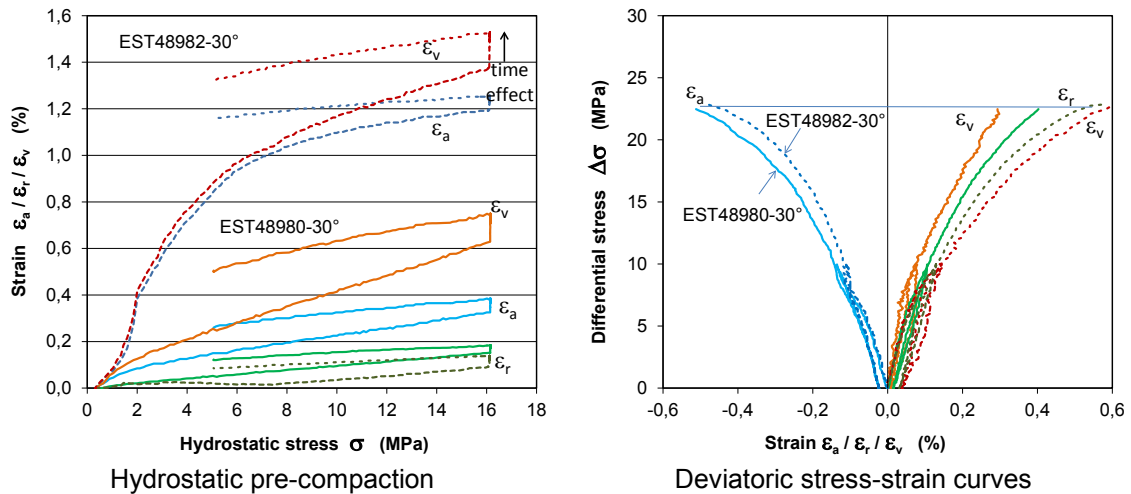
sample ID	angle to bedding α (°)	max. mean stress σ_m (MPa)	bulk density (g/cm³)	dry density (g/cm³)	porosity (%)	water content (%)	water saturation (%)
EST49021	0	16	2,426	2,248	17,20	7,3	95,8
EST49017	0	16	2,430	2,248	16,44	7,5	102,6
EST48980	30	16	2,448	2,284	15,45	6,7	98,9
EST48982	30	16	2,457	2,278	15,31	7,3	108,6
EST49057	45	16	2,465	2,309	14,96	6,4	98,0
EST49060	45	16	2,463	2,303	14,40	6,5	103,9
EST49079	60	16	2,435	2,278	15,33	6,4	95,6
EST49081	60	16	2,430	2,252	16,28	7,3	101,0
EST49105	90	16	2,442	2,264	15,68	7,3	105,4
EST49097	90	16	2,424	2,256	16,33	7,0	96,1
mean value		2,442	2,272	15,74	6,97	100,6	
standard deviation		0,015	0,021	0,779	0,414	4,239	

Radial stress increase at constant axial stress of 5 MPa						
sample ID	angle to bedding α (°)	elastic stiffness C (GPa)	$\varepsilon_a / \varepsilon_r$ ratio μ (-)	peak strength σ_F (MPa)	failure strain ε_{a-f} (%)	fracture angle β (°)
EST49021	0	12,61	1,15	22,4	-0,46	70,0
EST49017	0	13,39	1,36	24,5	-0,49	85,0
EST48980	30	6,25	0,66	22,5	-0,52	80,0
EST48982	30	10,34	1,25	22,8	-0,48	65,0
EST49057	45	8,68	0,83	24,3	-0,45	80,0
EST49060	45	12,38	1,24	27,0	-0,59	65,0
EST49079	60	16,48	1,63	19,8	-0,40	85,0
EST49081	60	18,00	1,82	19,2	-0,48	65,0
EST49105	90	7,97	0,74	22,9	-0,61	90,0
EST49097	90	11,97	1,08	22,9	-0,60	85,0
mean value		11,81	1,18	22,84	-0,51	77,0
standard deviation		3,481	0,354	2,123	0,067	9,274

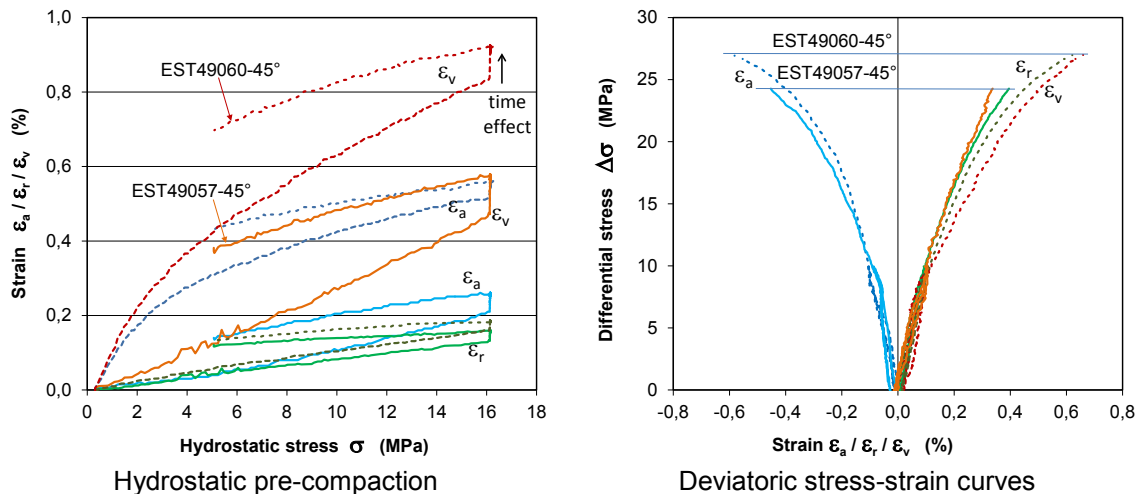
Axial loading orientation $\alpha = 0^\circ$



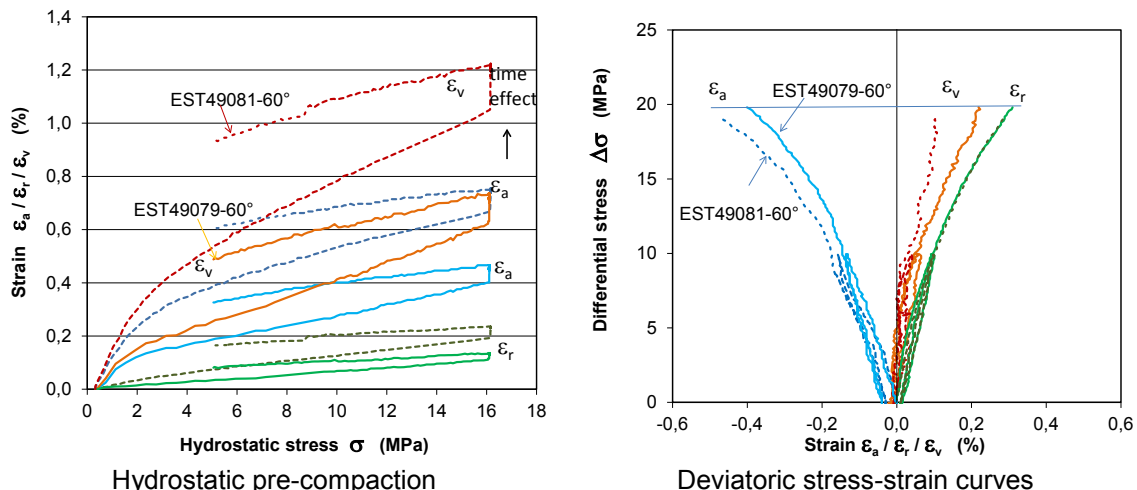
Axial loading orientation $\alpha = 30^\circ$



Axial loading orientation $\alpha = 45^\circ$



Axial loading orientation $\alpha = 60^\circ$



Axial loading orientation $\alpha = 90^\circ$

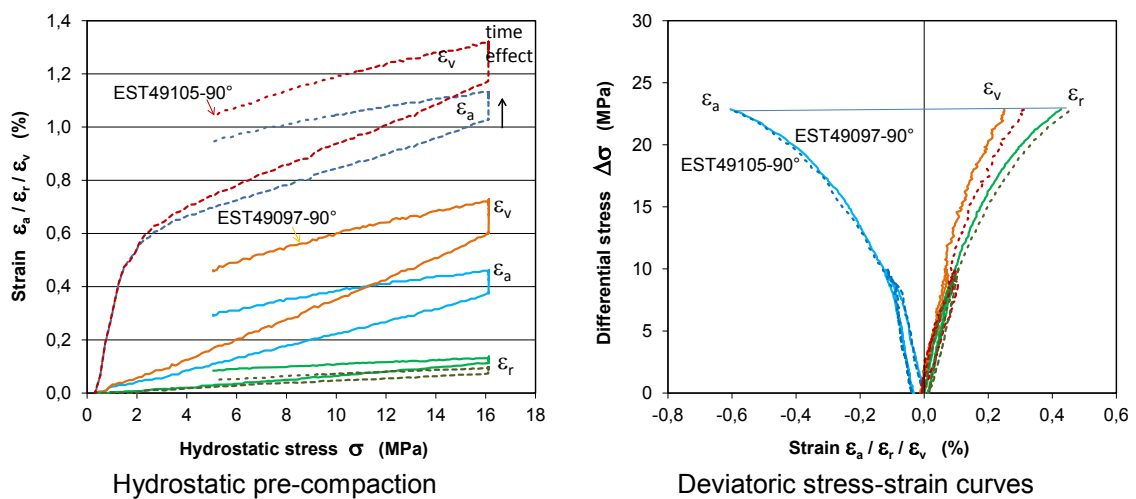


Fig. E.25 Stress-strain curves from TES triaxial extension tests

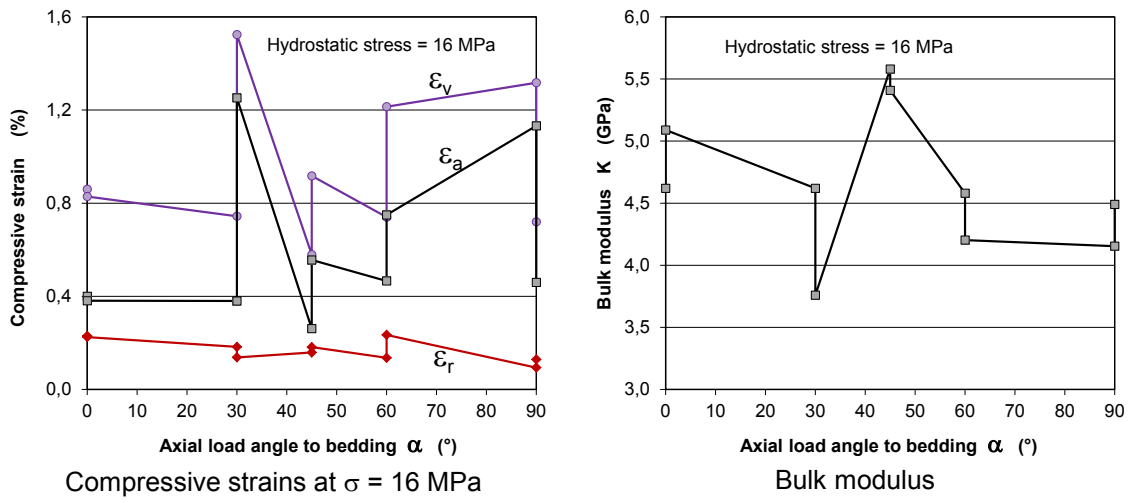


Fig. E.26 Parameters obtained from the TES hydrostatic pre-compaction

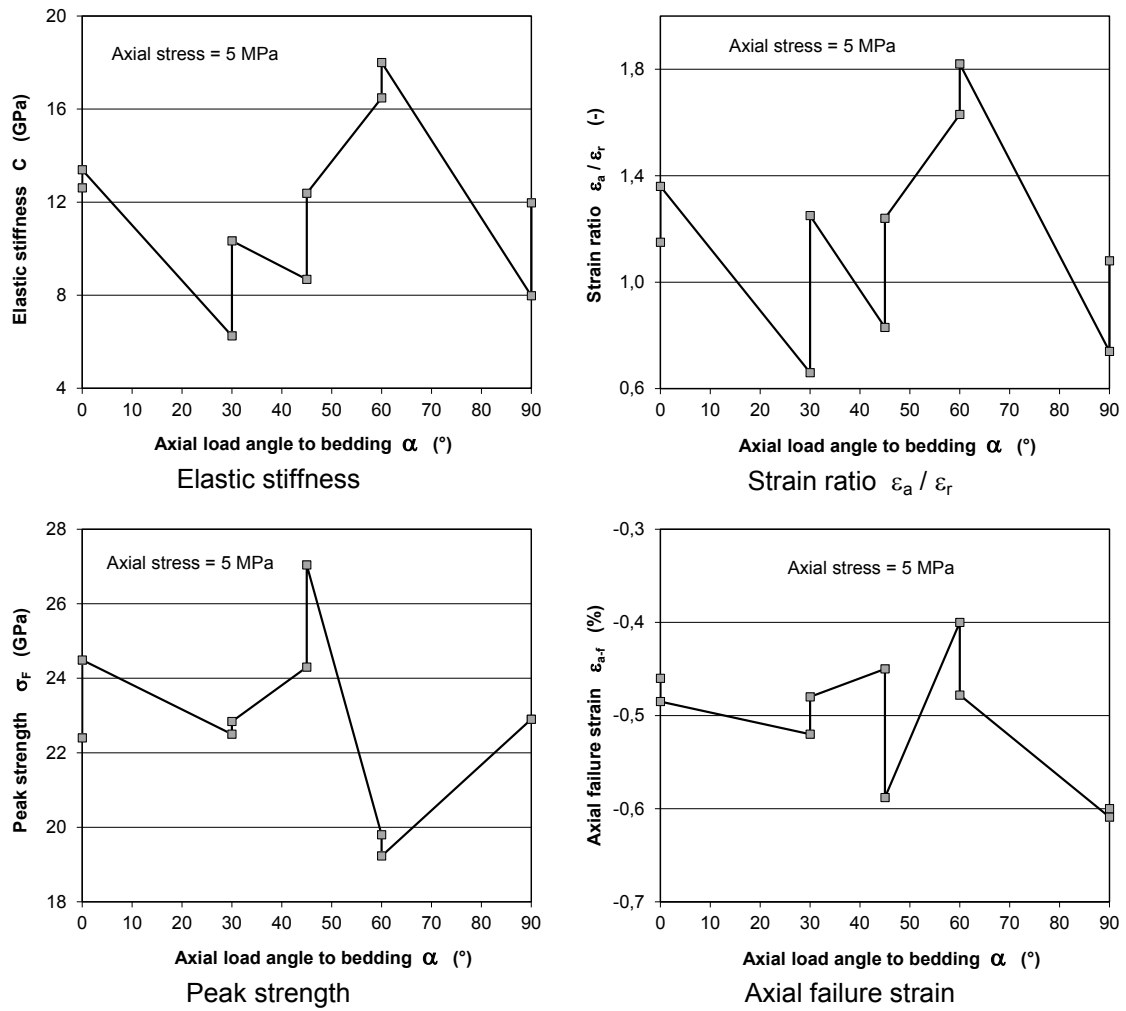


Fig. E.27 Parameters obtained from the TES triaxial extension

E.4 TEM – triaxial extension tests at constant mean stress

Tab. E.4 Characteristic parameters determined from the TM extension tests

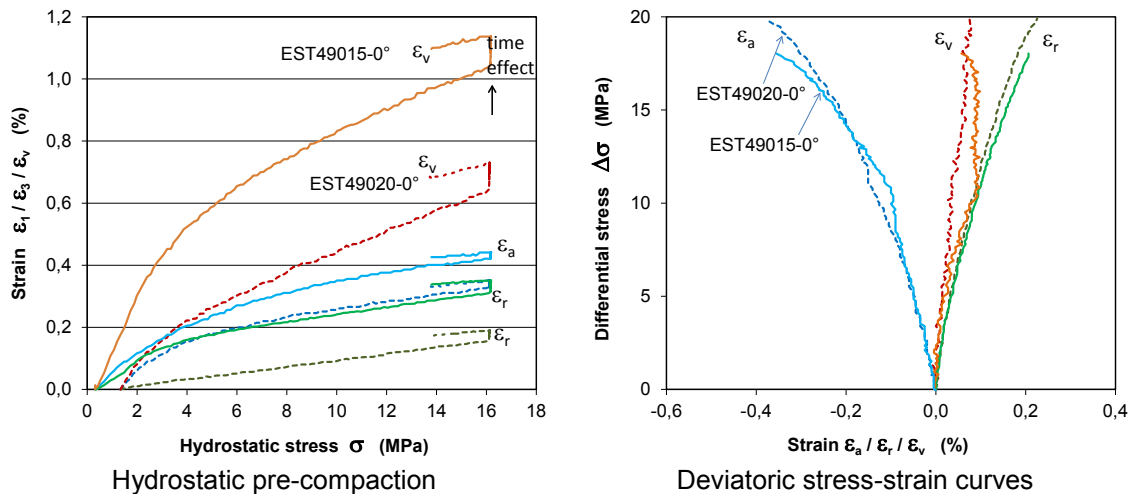
Basic properties of the samples before testing								
sample ID	D/L (mm)	angle to bedding α (°)	grain density (g/cm³)	bulk density (g/cm³)	dry density (g/cm³)	initial porosity (%)	water content (%)	water saturation (%)
EST49015	50/100	0	2,680	2,405	2,246	16,18	6,6	91,6
EST49020	50/100	0	2,700	2,430	2,260	16,30	7,0	97,1
EST48984	50/100	30	2,702	2,420	2,234	17,32	7,7	99,2
EST48975	50/100	30	2,690	2,420	2,260	15,97	6,6	93,4
EST48976	50/100	30	2,690	2,430	2,260	15,99	7,0	98,9
EST49053	50/100	45	2,680	2,420	2,243	16,29	7,3	100,5
EST49074	50/100	60	2,691	2,417	2,236	16,92	7,5	99,1
EST49095	50/100	90	2,680	2,400	2,222	17,10	7,4	96,5
EST49113	50/100	90						
mean value			2,689	2,418	2,245	16,51	7,14	97,0
standard deviation			0,008	0,010	0,013	0,492	0,381	2,907

Hydrostatic pre-compaction up to 16 MPa						
sample ID	angle to bedding α (°)	max. mean stress σ_m (MPa)	max. axial strain ε_{a-m} (%)	max. radial strain ε_{r-m} (%)	max. volume strain ε_{v-m} (%)	bulk modulus K (GPa)
EST49015	0	16	0,44	0,35	1,14	6,87
EST49020	0	16	0,35	0,19	0,73	6,28
EST48984	30	16	0,50	0,16	0,81	6,44
EST48975	30	16	0,47	0,28	1,01	6,86
EST48976	30	16	0,31	0,18	0,65	6,54
EST49053	45	16	0,34	0,16	0,66	6,82
EST49074	60	16	1,13	0,22	1,56	6,26
EST49095	90	16	1,06	0,16	1,37	6,11
EST49113	90	16	0,45	0,16	0,76	5,76
mean value			0,56	0,21	0,97	6,44
standard deviation			0,292	0,063	0,311	0,356

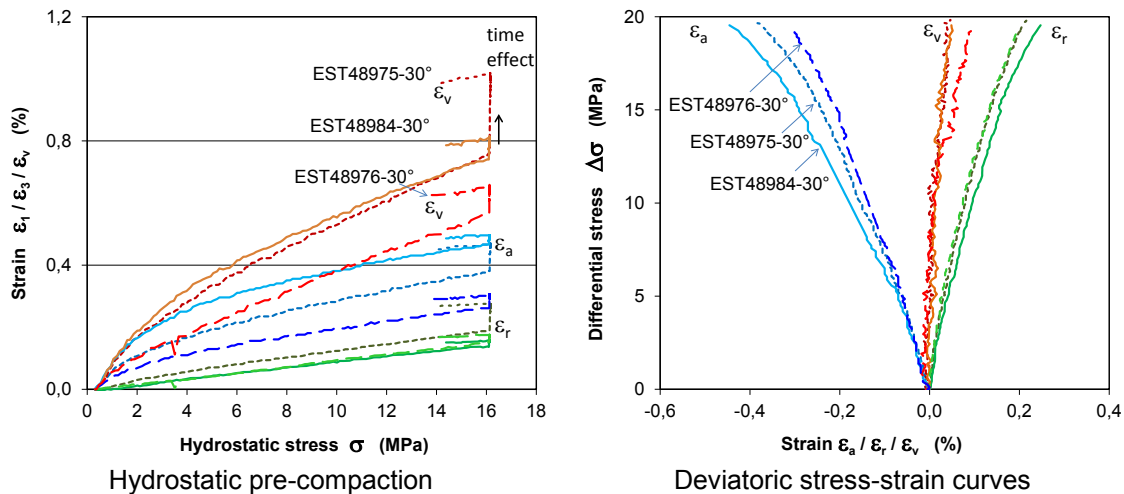
sample ID	angle to bedding α (°)	max. mean stress σ_m (MPa)	bulk density (g/cm³)	dry density (g/cm³)	porosity (%)	water content (%)	water saturation (%)
EST49015	0	16	2,433	2,272	15,22	6,6	98,5
EST49020	0	16	2,448	2,277	15,68	7,0	101,6
EST48984	30	16	2,440	2,252	16,65	7,7	104,0
EST48975	30	16	2,445	2,283	15,11	6,6	99,7
EST48976	30	16	2,446	2,275	15,44	7,0	103,2
EST49053	45	16	2,436	2,258	15,74	7,3	104,7
EST49074	60	16	2,455	2,271	15,60	7,5	104,2
EST49095	90	16	2,433	2,253	15,95	7,4	104,9
EST49113	90	16					
mean value			2,442	2,268	15,67	7,14	100,2
standard deviation			0,007	0,011	0,449	0,381	3,134

Radial stress increase at constant mean stress of 13.7 MPa					
sample ID	angle to bedding α (°)	Mean stress (MPa)	peak strength σ_F (MPa)	failure strain ε_{a-f} (%)	fracture angle β (°)
EST49015	0	13,7	18,00	-0,36	x
EST49020	0	13,7	19,90	-0,38	x
EST48984	30	13,7	19,53	-0,45	75,0
EST48975	30	13,7	19,83	-0,39	90,0
EST48976	30	13,7	19,22	-0,30	75,0
EST49053	45	13,7	17,25	-0,37	90,0
EST49074	60	13,7	15,30	-0,53	70,0
EST49095	90	13,7	18,55	-0,54	88,0
EST49113	90	13,7	19,37	-0,45	90,0
mean value			18,55	-0,42	82,57
standard deviation			1,418	0,076	8,174

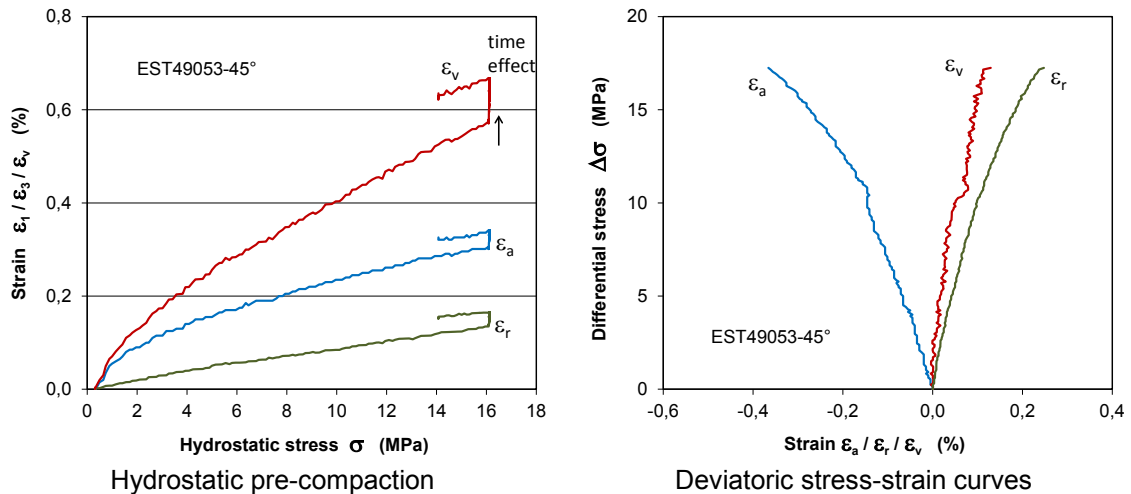
Axial loading orientation $\alpha = 0^\circ$



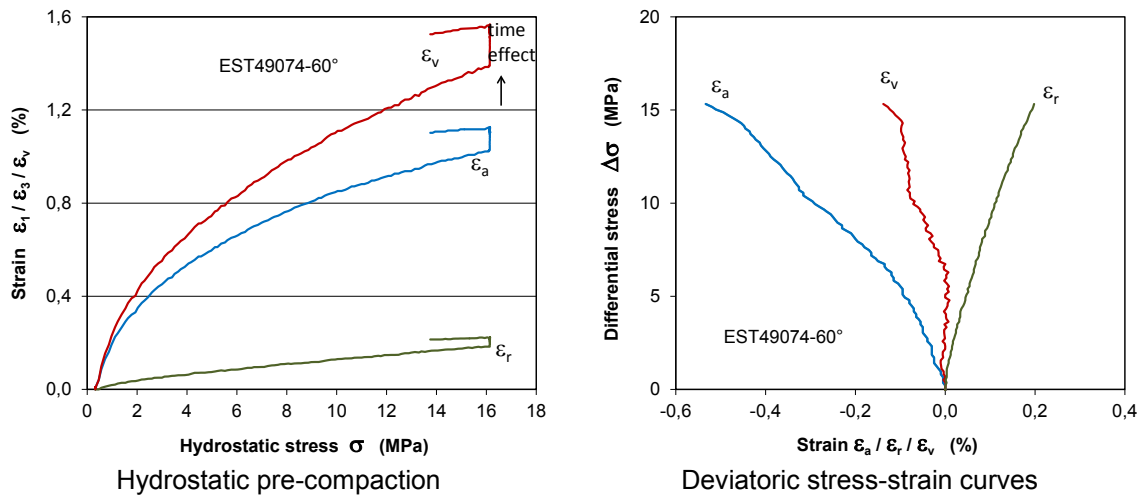
Axial loading orientation $\alpha = 30^\circ$



Axial loading orientation $\alpha = 45^\circ$



Axial loading orientation $\alpha = 60^\circ$



Axial loading orientation $\alpha = 90^\circ$

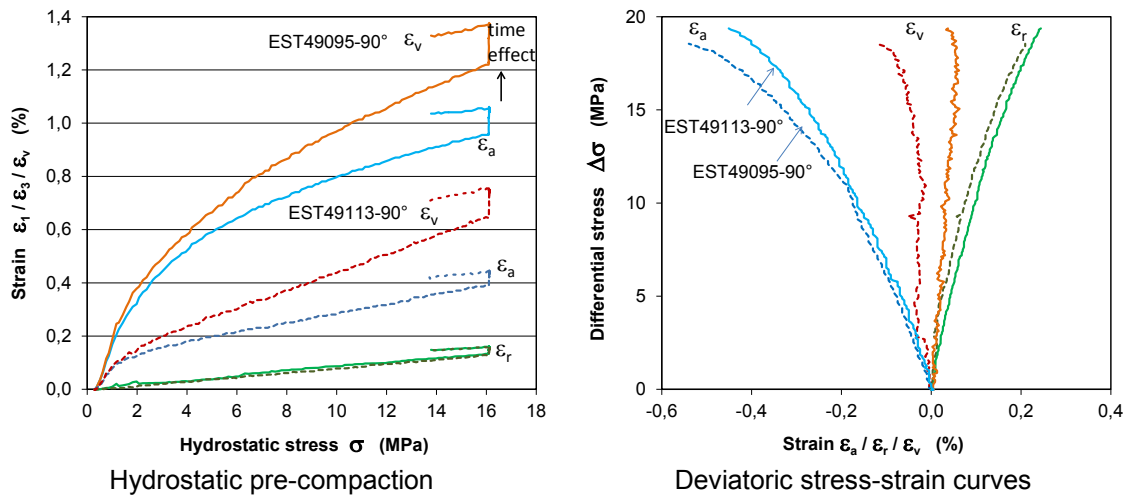


Fig. E.28 Stress-strain curves from TEM triaxial extension tests

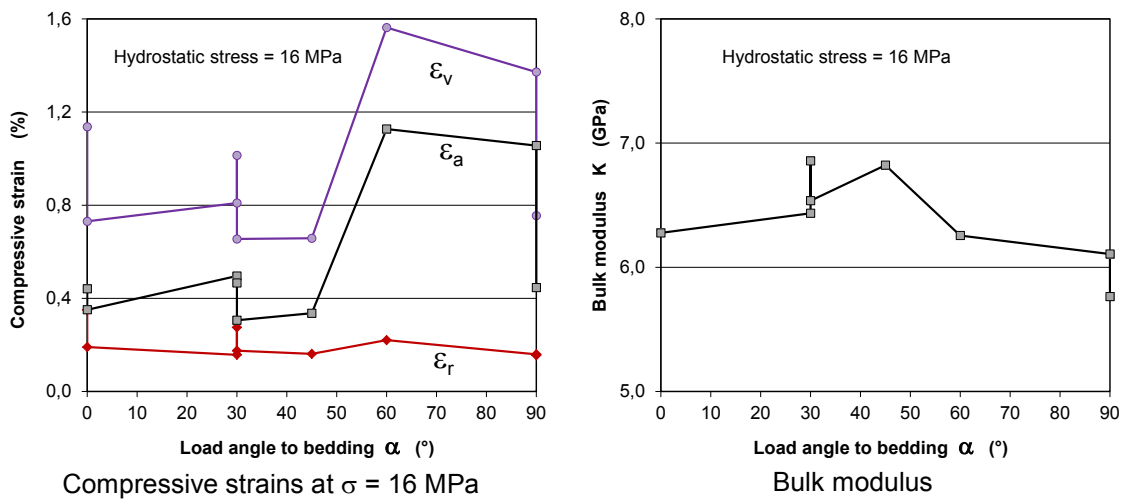


Fig. E.29 Parameters obtained from the TEM hydrostatic pre-compaction

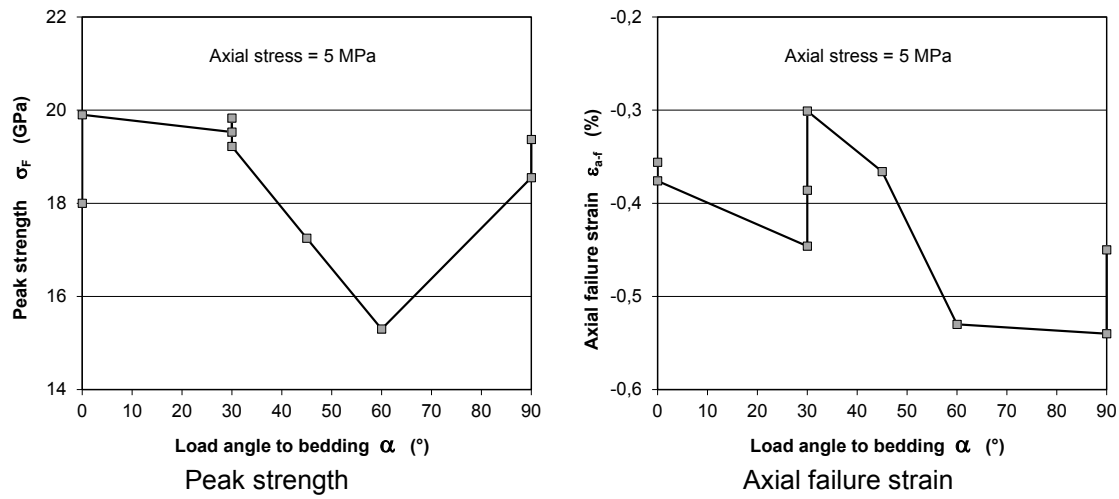


Fig. E.30 Parameters obtained from the TEM triaxial extension

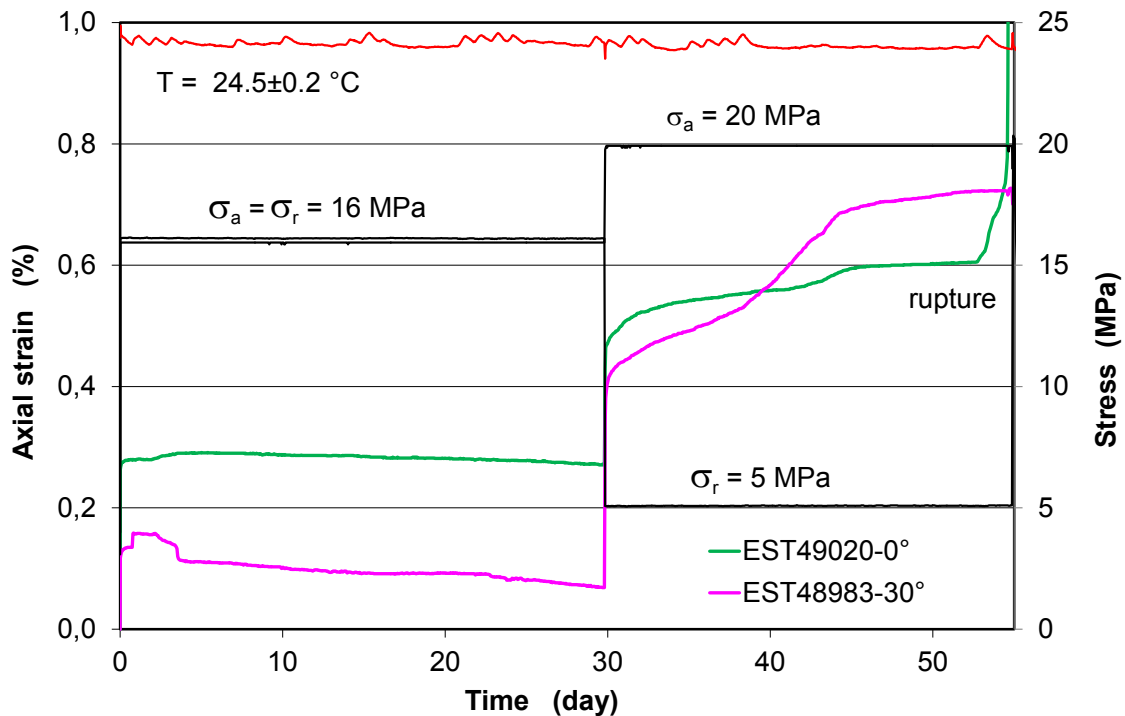
E.5 TCC – triaxial creep tests at multistep stress states

Tab. E.5 Characteristic parameters determined from the TCC creep tests

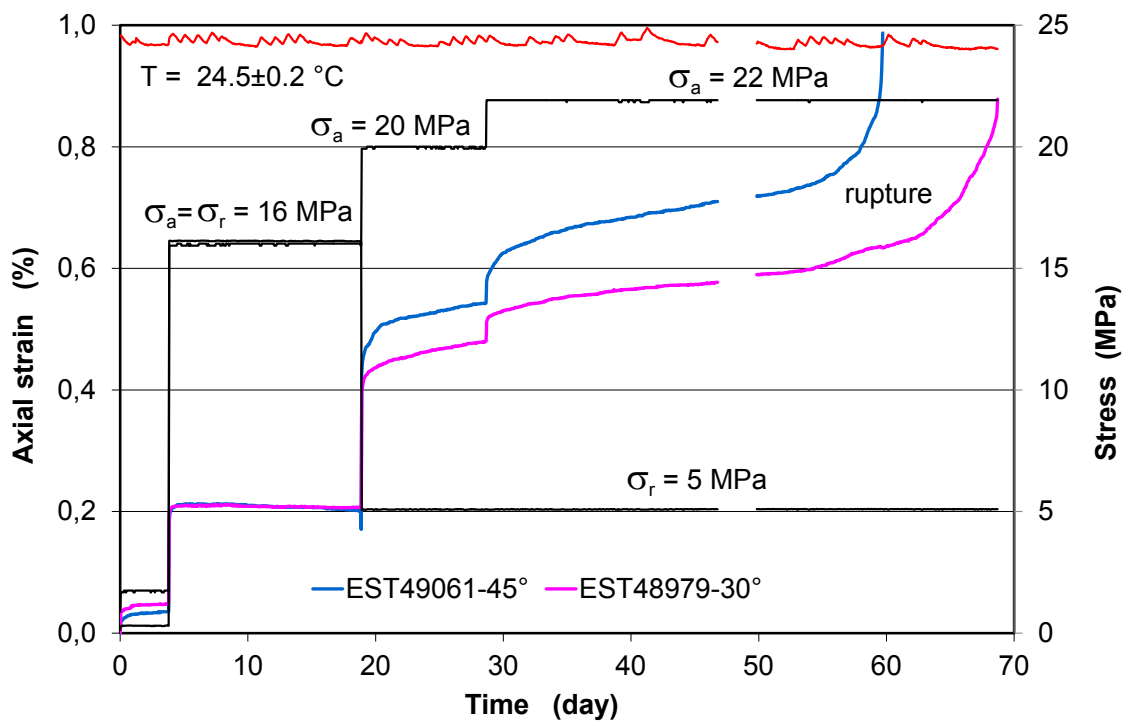
Basic properties of the samples before testing								
sample ID	D/L (mm)	angle to bedding α (°)	grain density (g/cm³)	bulk density (g/cm³)	dry density (g/cm³)	initial porosity (%)	water content (%)	water saturation (%)
EST49020	70/140	0	2,700	2,430	2,260	16,30	7,0	97,1
EST48983	70/140	30	2,700	2,410	2,236	17,17	7,2	93,8
EST48979	70/140	30	2,700	2,440	2,267	16,05	7,1	100,3
EST49061	70/140	45	2,690	2,430	2,253	16,26	7,3	101,1
EST49082	70/140	60	2,680	2,400	2,225	16,99	7,3	95,6
EST49106	70/140	90	2,680	2,410	2,234	16,64	7,3	98,0
mean value			2,692	2,420	2,246	16,57	7,20	97,7
standard deviation			0,009	0,014	0,015	0,404	0,115	2,537

Creep failure stress and strain					
sample ID	angle to bedding α (°)	radial stress (MPa)	axial stress (MPa)	creep failure stress σ _f (MPa)	failure strain ε _{a-f} (%)
EST49020	0	5	20,0	15,0	0,50
EST48983	30	5	x	x	x
EST48979	30	5	22,0	17,0	0,50
EST49061	45	5	22,0	17,0	0,55
EST49082	60	5	22,0	17,0	0,51
EST49106	90	5	22,0	17,0	0,50

Group 1 with two samples with axial loading angle $\alpha = 0^\circ$ and 30°



Group 2 with two samples with axial loading angle $\alpha = 30^\circ$ and 45°



Group 3 with two samples with axial loading angle $\alpha = 60^\circ$ and 90°

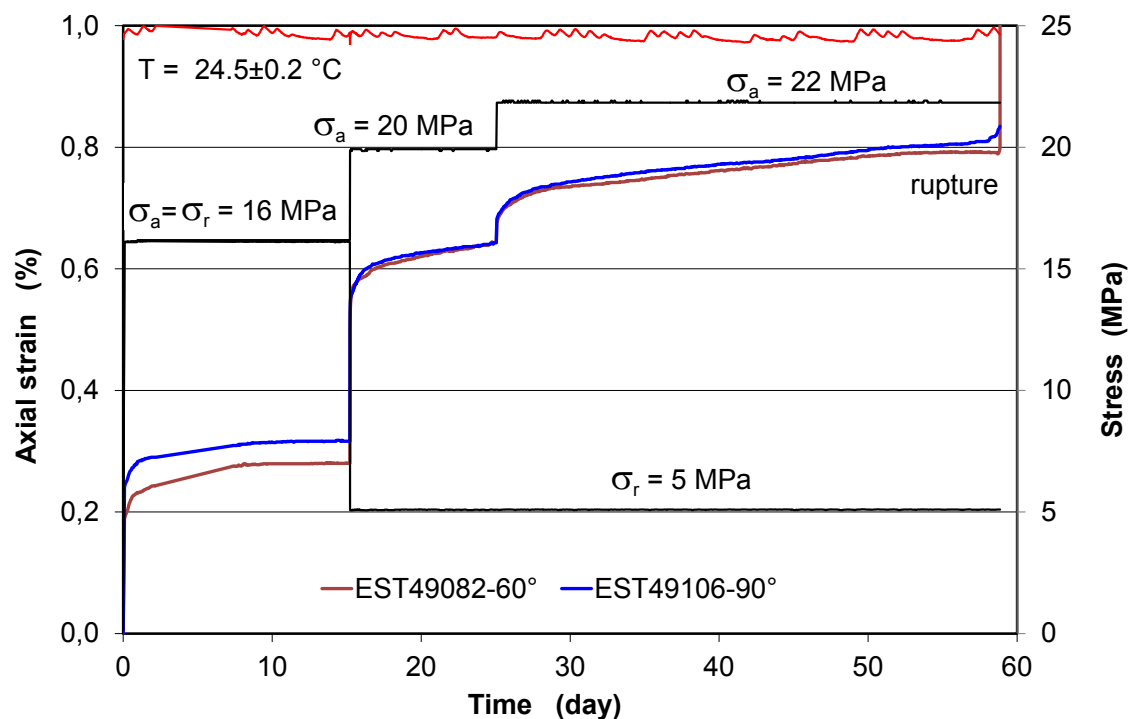


Fig. E.31 Creep curves obtained under constant triaxial stress conditions

Gesellschaft für Anlagen- und Reaktorsicherheit (GRS) gGmbH

Schwertnergasse 1
50667 Köln
Telefon +49 221 2068-0
Telefax +49 221 2068-888

Forschungszentrum
85748 Garching b. München
Telefon +49 89 32004-0
Telefax +49 89 32004-300

Kurfürstendamm 200
10719 Berlin
Telefon +49 30 88589-0
Telefax +49 30 88589-111

Theodor-Heuss-Straße 4
38122 Braunschweig
Telefon +49 531 8012-0
Telefax +49 531 8012-200

www.grs.de

French Agence Nationale Pour la Gestión des Déchets Radioactifs (ANDRA)

1/7, rue Jean Monnet
Parc de la Croix-Blanche
92298 Châtenay-Malabry cedex
FRANCE

www.andra.fr

ISBN 978-3-944161-41-9